In-situ TEM study of carbon nanomaterials and thermoelectric nanomaterials

by

Xiaoting Jia

M.S., State University of New York - Stony Brook (2006)

B.S., Fudan University (2004)

Submitted to the Department of Materials Science and Engineering
in partial fulfillment of the requirements for the degree of
Doctor of Philosophy in Materials Science and Engineering
at the

MASSACHUSETTS INSTITUTE OF **TECHNOLOGY**

June 2011

Signature of Author……
Department of Materials Science and Engineering
May 18, 2011

Certified by……..
Mildred S. Dresselhaus
Institute Professor of Electrical Engineering and Physics
Thesis supervisor

Accepted by……..
Christopher Schuh
Chair, Departmental Committee on Graduate Students

In-situ TEM study of carbon nanomaterials

and thermoelectric nanomaterials

by

Xiaoting Jia

Submitted to the Department of Materials Science and Engineering

on May 18, 2011 in partial fulfillment of the requirements for the degree of

Doctor of Philosophy in Materials Science and Engineering

Abstract

Graphene nanoribbons (GNRs) are quasi one dimensional structures which have unique transport properties, and have a potential to open a bandgap at small ribbon widths. They have been extensively studied in recent years due to their high potential for future electronic and spintronic device applications. The edge structures - including the edge roughness and chirality - dramatically affect the transport, electronic, and magnetic properties of GNRs, and are of the critical importance. We have developed an efficient way of modifying the edges structures, to produce atomically smooth zigzag and armchair edges by using *in-situ* TEM with a controlled bias. This work provides us with many opportunities for both fundamental studies and for future applications. I also report the use of either furnace heating or Joule heating to pacify the exposed graphene edges by loop formation in the graphitic nanoribbons. The edge energy minimization process involves the formation of loops between adjacent graphene layers. An estimation of the temperature during *in-situ* Joule heating is also reported based on the melting and evaporation of Pt nanoparticles. In this thesis work, I have also investigated the morphological and electronic properties of GNRs grown by chemical vapor deposition. Our results suggest that the GNRs have a surprisingly high crystallinity and a clean surface. Both folded and open edges are observed in GNRs. Atomic resolution scanning tunneling microscopy (STM) images were obtained on the folded layer and the bottom layer of the GNR, which enables clear identification of the chirality for both layers. We have also studied the electronic properties of the GNRs using low temperature scanning tunneling spectroscopy (STS). Our findings suggest that edges states exist at GNR edges which are dependent on the chiral angles of the GNRs.

Thesis Supervisor: Mildred S. Dresselhaus
Title: Institute Professor of Electrical Engineering and Physics

Acknowledgments

I am deeply grateful to my advisor Prof. Mildred S. Dresselhaus for her guidance, encouragement, and continuous support. She is a true inspiration to me. Her dedication to science, her scientific vision, her passion on mentoring young professionals and her being always approachable for students have set a great example for me. I am also grateful to Dr. Gene Dresselhaus who is always there to help, to criticize and give advice in a unique entertaining way, and brings us lots of happiness. I would like to thank Laura Doughty for all of her help, and most importantly her deep caring about me in these five years.

I am also very grateful to many other great people who I closely interacted with during my thesis work. I am very thankful to Prof. Jing Kong for her generous support, her advice and guidance throughout the years. I am also very thankful to Prof. Gang Chen who has taught me a lot about how to conduct innovative research and develop a scientific career. I also greatly appreciate his continuous support, encouragement, and the time he spent on me during weekly meetings in my first year and later discussions. I am very thankful to Prof. Silvija Gradecak who I always go for help on TEM questions as well as general advice. I also enjoyed the TA experience with her very much and learnt a lot from her. I am grateful to Prof. Yoel Fink who has given me invaluable advice for my thesis work. I would also like to thank Prof. Francesco Stellacci for the useful discussions and scientific inputs.

I would like to thank Prof. Mauricio Terrones who I closely collaborated with in many of my thesis projects. Without his advice, his scientific insights and the frequent teleconference or email discussions with him, my thesis work would not have been possible. I also want to thank our collaborator Prof. Vincent Meunier for all the theoretical calculations and discussions, and for inviting me to visit ORNL and RPI. I am thankful to Dr. Minghu Pan who I closely worked with during my visit at ORNL (and afterwards) with his home-built UHV STM. I want to thank Dr. Bobby G. Sumpter and Dr. Eduardo Cruz-Silva for theoretical calculations on graphene edges, and Dr. Helen Farrell for the calculations on nanoparticles. I also want to thank Prof. Zhifeng Ren for providing the *in-situ* TEM facilities at Boston College and for the discussions.

I would like to thank Jessica Campos-Delgado and Jose M. Romo-Herrera who visited our group with graphitic nanoribbon samples, and the collaboration with them resulted in interesting and important science. I would like to thank all the people in the MGM group, NME lab, NanoEngineering group, and Prof. Ren's group who have made my research and life at MIT much more colorful and enjoyable. I especially thank Dr. Shuo Chen for teaching me *in-situ* TEM, and for the discussions and ideas, Mario Hofmann for the help on data analysis, scientific discussion and all kinds of problem solving, Alfonso Reina, Ki Kang Kim, Yumeng Shi, Sreekar Bhaviripudi, Hyungbin Son, Ya-Ping Hsieh Vincent Berube for invaluable and enjoyable collaborations.

I am also grateful to all of my other friends at MIT, especially my DMSE classmates and friends from CSSA. They have accompanied and supported me through all these years, and made my MIT life a wonderful experience.

Finally, this thesis is dedicated to my parents who have given me unlimited support and love.

Contents

List of Figures

List of Tables

Chapter 1

Introduction

Nanostructured materials and related research have expanded significantly in the past two decades. The low dimensional effects give rise to dramatic changes in the materials properties, which could for example be utilized to enhance the figure of merit of an existing thermoelectric material, to explore new applications of a material, and to study its fundamental physical properties, among others. Thermoelectric nanomaterials (nano-composites, nanobelts, nanowires, etc.) and carbon based nanostructures (single- or multi-wall carbon nanotubes, graphene films, graphene nanoribbons, etc.) are two materials that have recently attracted a lot of attention due to their potential for both fundamental studies and applications [1-11].

While the synthesis of nanomaterials is developing rapidly, the development of new characterization tools and techniques capable of studying nanostructured materials are also becoming important. Most commonly used characterization techniques include transmission electron microscopy (TEM), scanning electron microscopy (SEM), atomic force microscopy (AFM), scanning tunneling microscopy (STM), Raman spectroscopy, X-ray diffraction, etc. The small scale of nanomaterials requires sophisticated manipulation and probing techniques, and therefore integrated systems which combine two or more different characterization techniques have emerged.

In this thesis work, an integrated TEM-STM system is used to study thermoelectric nanomaterials and carbon based nanostructures. With this TEM-STM system, nanoparticles, nanoribbons, nanowires, and films can be manipulated individually, and contacted with electrodes, allowing a voltage to be applied, while its structure being observed *in-situ* with the TEM. A lot of new

properties of the nanomaterials can thus be probed with this combined characterization technique.

The main contributions of this work include the following: (1) A novel method for forming atomically smooth edges in graphitic nanoribbons was developed using *in-situ* Joule heating. The resultant edges mostly show either zigzag or armchair configurations. (2) Folded edge formation was also studied experimentally using both furnace heating and Joule heating. A theoretical model was introduced for understanding the edge folding mechanism. (3) STM and STS characterization of CVD grown graphene nanoribbons and edges states was studied for the first time. (4) Bismuth nanowire reduction and bismuth nanoparticles formation was studied for the first time using the *in-situ* TEM.

This thesis is presented in 9 chapters. Following this introduction chapter, Chapter 2 reviews the current status of the graphene nanoribbon and edge study. Chapter 3 presents the characterization of CVD grown graphene and BN thin films using HRTEM and elemental analysis tools. Chapter 4 introduces the *in-situ* Joule heating method for graphene edge modification. Chapter 5 discusses folded edge formation using furnace heating and Joule heating. Chapter 6 presents Pt nanoparticle melting experiments for temperature estimation during *in-situ* Joule heating. Chapter 7 presents the results on STM and STS studies of CVD grown graphene nanoribbons. Chapter 8 introduces our *in-situ* TEM study of bismuth nanowires and nanoparticles. And in Chapter 9, a conclusion of the thesis work is presented together with an outlook to the future.

Chapter 2

Graphene nanoribbons and edges

In this chapter, the current status of graphene nanoribbons and graphene edge study is presented, which provides the general background for the following chapters from Chapter 3 through Chapter 7.

2.1 Graphene nanoribbons and edge properties

The study of graphene, and in particular of graphene edges, is a research topic that has expanded rapidly over the past few years. The motivation for the popularity of this field largely stems from the unique electronic, chemical, and magnetic properties of graphene edges. The graphene community has become increasingly aware of the importance of clean, atomically sharp edges, in light of experimental difficulties in designing electronic logic devices due to the presence of disorder in the edges of narrow graphene ribbons [12]. In this chapter I will review the present status of graphene edges, their fabrication, characterization, and properties. Specifically, I will present an overview of the different methods commonly employed in the production of graphene nanoribbons and graphene edges. I will also discuss the characterization of graphene edges using transmission electron microscopy (TEM) and Raman spectroscopy, and discuss about edge defects which are found in graphene. Finally I will conclude with a summary.

Graphene, a single layer of carbon atoms forming a two-dimensional (2D) honeycomb lattice, can, in principle, be considered as an elementary building block for all sp^2-hybridized carbon allotropes. Although graphene was in fact produced experimentally decades ago [13], it wasn't until the recent developments in 2004 by the Manchester group that the field of graphene

research took off rapidly [4,7,10,14], These developments in the "science of graphene" prompted an unprecedented surge of activity and demonstration of new physical phenomena. These developments also triggered a renewed emphasis on the interdisciplinary nature of nanoscience and created new opportunities in materials science, physics, chemistry, and electrical engineering. Graphene is a unique monolayer two dimensional crystal, which exhibits a room temperature quantum Hall effect [15]. It is the strongest material by weight, so far reported [16]. It is a semimetal with its conduction band and valence band being degenerate at the K point in the Brillouin zone (a situation that occurs only for the special unit-cell geometry and orientation relative to graphene's high-symmetry axis). Graphene shows a symmetrical linear dispersion relation for electrons and holes, and it has an extremely high room temperature carrier mobility that is about 2 orders of magnitude greater than that of silicon [10].

One of the most widely discussed applications of graphene in electronics is its potential use in field effect transistors (FETs). The promise held by graphene for electronics applications is due to the fact that it is one atomic layer thick and should therefore yield particularly good performance for high frequency applications. In order to make FET (field effect transistor) devices for digital logic applications, a sizable band-gap is required [17]. In this context, graphene nanoribbons with narrow widths (below 20 nm) can generate such a bandgap that is dependent on the ribbon width and crystallographic orientation of the edges [18]. Unfortunately, the as-produced narrow ribbons usually suffer from disordered edges that make the bandgap poorly defined [19]. which in turn results in a dramatically degraded carrier mobility. This constitutes the main reason why obtaining atomically sharp edges in narrow graphene nanoribbons of controlled width has been one of the most important challenges for the applications of graphene in electronic devices [20].

There are two types of achiral edges in graphene nanoribbons - zigzag and armchair edges, defined by the orientation of the hexagons relative to the ribbon length (see Figure 2.1). These achiral edges have been observed to dominate over chiral edges after joule heating [21]. Theoretical calculations [22] show that

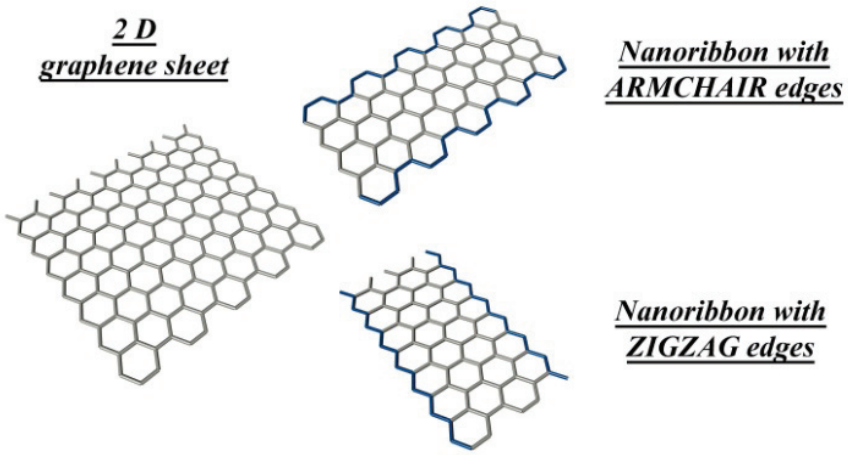

Figure 2.1 Zigzag and armchair edges in monolayer graphene nanoribbons. The edge structure and the number of atomic rows of carbon atoms normal to the ribbon axis determine the electronic structure and ribbon properties. (Image courtesy of M. Hofmann, MIT)

zigzag edges are metastable and a planar reconstruction into pentagon-heptagon configurations spontaneously takes place at room temperature. In practice, hydrogenated or oxygenated edge passivation during heat treatment [23,24] is commonly used to stabilize the edges in air. The detailed chemistry and carrier transport associated with these functionalized edges seem very exciting and further work is necessary along these directions.

2.2 Fabrication of graphene nanoribbons and edges

Edged graphene (nanoribbons) can be fabricated in various ways. Quantum mechanical manifestations are most pronounced in narrow, high-quality edged graphene ribbons which have a unique crystallographic orientation. Such graphene nanoribbons (GNRs) are therefore expected to be the most important in graphene electronic device applications. As a result, there has been significant progress in the large-scale production of GNRs in recent years with approaches such as the mechanical exfoliation of graphite, chemical vapor deposition, and lithographic, chemical and sonochemical methods.

It is noteworthy that different types of defects are generally present in high or low concentrations on the edges of graphene or graphene nanoribbons [25]. From an electronic materials point of view, the presence of hydroxyl groups on the edges could affect the nanoribbon carrier transport, and they should be removed in order to enhance the conductivity of the ribbons. In this context, Tour's group demonstrated that hydrazine is very efficient in removing oxygen from the graphene nanoribbons, thus improving their electrical conductivity [26]. However, a great majority of the published work in the graphene field does not emphasize (or study in detail) the importance of edge defects (or edge functionalities), and most of these papers assume that some of the produced graphene nanoribbons are defect-free or very close to that. Therefore, further research involving the detailed chemistry and physics of sharp- and defective-graphene edges should be carried out, with the goal of understanding and eventually reaching control of edge defects.

2.2.1 Chemical vapor deposition (CVD)

Although lithographically produced graphene nanoribbons have been commonly used in research laboratories, chemically derived graphene nanoribbons have also been demonstrated [27]. Such narrow GNRs however may not be as appealing for bulk industrial level applications due to their multi-step processing and relatively low yields. Therefore, chemical vapor deposition (CVD) offers an alternative approach for preparing large quantities of graphene nanoribbons in a relative short amount of time [28]. The first report of CVD graphite nanoribbon samples is attributed to Murayama and Maeda in 1990 [29]. Through the decomposition of a reactant gas containing $CO/H_2/Fe(CO)_5$ at 400-700 ºC, they were able to produce graphite filaments 10 μm long, with a rectangular cross-section 100-700 nm wide and 10-200 nm thick with catalytic Fe_3C particles attached to one of the ends (Figs. 2.2a-c). Using high-resolution TEM they demonstrated that the graphene sheets had a uniform orientation perpendicular to the filament axis and that the graphene edges formed loops at the edges upon thermal annealing at

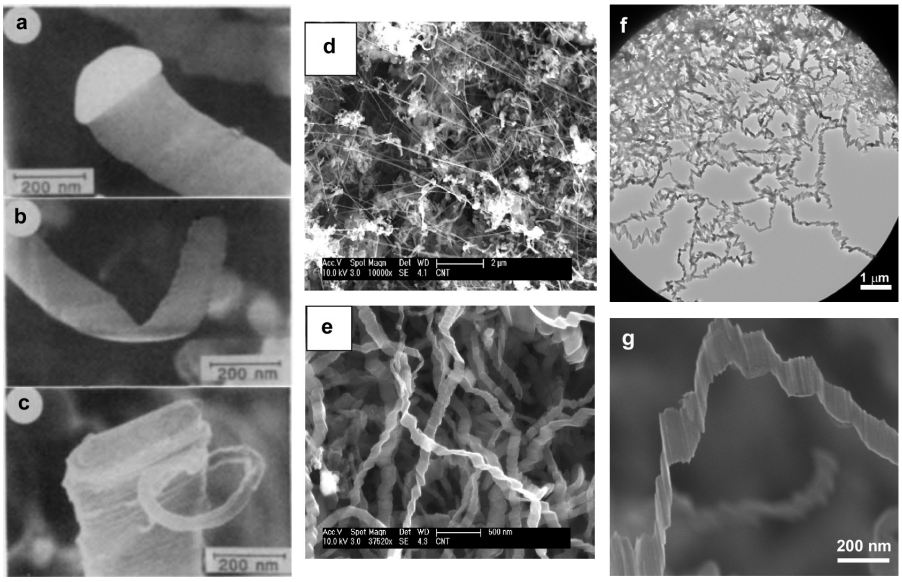

Figure 2.2 CVD grown graphitic nanoribbons. (a) SEM micrographs by Murayama and Maeda of the ribbon-like filaments of graphite prepared at 700 ºC, using a bright catalytic particle which is located on the tip of the filament; (b) the 'tail' of a ribbon-like filament prepared at 700 ºC; (c) the cross-section of a ribbon-like filament prepared at 550 ºC ((a), (b) and (c) are extracted from Ref. [29]); (d) SEM image of a mixture of carbon nanoribbons and Fe filled MWNTs reported by Mahanandia, et al.; [30] (e) Magnified SEM image of carbon nanoribbons ((d) and (e) are extracted from Ref. [30]). (f) A low magnification TEM image of many suspended graphitic nanoribbons reported by Campos-Delgado, et al.; [28] (g) SEM image showing the wavy structure of graphitic nanoribbons ((f) and (g) are extracted from Ref. [28]).

2800 ºC [29]. In 2008, two different routes were reported for obtaining graphitic nanoribbons. One of them involved the decomposition of ferrocene and tetrahydrofuran at a temperature of 950 ºC, and the material thus produced contained a mixture of iron filled multiwall carbon nanotubes (MWNTs) and carbon nanoribbons (Figs. 2.2d and 2.2e). Although the length and width of the nanoribbons are not discussed in the report, by observation of the published SEM images, the material appears to be ~200 nm in width and tens of microns in length. The graphitic structure of the carbon nanoribbons was confirmed through X-ray diffraction and TEM measurements, showing that the (002) lattice planes are perpendicular to the axis of growth [30]. The second report involved the thermal decomposition at 950 ºC of ferrocene/ethanol/thiophene solutions, resulting in the synthesis of a material of ~40 graphene layers in thickness

(stacked parallel to the axis of growth), 20-300 nm in width, and tens of microns in length (Figs. 2.2f and 2.2g) [28]. These ribbons start oxidizing at 700 °C [28], similar to highly oriented pyrolytic graphite (HOPG). This method of CVD synthesis produces large quantities of graphitic nanoribbons, and the as-synthesized nanoribbons have many open edges that are suitable for the study of the structural and electronic properties of graphene edges.

2.2.2 Unzipping of carbon nanotubes

Unzipping carbon nanotubes along their longitudinal direction constitutes an alternative method for graphene nanoribbon synthesis. This concept has been adopted by several groups using different reactants and methods. Kosynkin et al. [26] report that MWCNTs can be unzipped by using a chemical treatment with sulphuric acid (H_2SO_4) and potassium permanganate ($KMnO_4$; an oxidizing agent) as schematized in Figure 2.3a. Multi-layer graphene nanoribbons and graphene sheets can be produced in this way. The resulting ribbons are up to 4 μms long, 100-500 nms wide, and 1-30 graphene layers thick. The as-synthesized ribbon edges have many oxygen-containing chemical groups that quench the electrical conductivity of the ribbons, so that reduction or annealing in hydrogen have to be carried out to remove these groups from the edges. More recently, Higginbotham *et al.* [31] reported that the nanotube unzipping process can be optimized by an efficient chemical oxidation process at a somewhat elevated temperatures (60 °C) in the presence of a second acid ($C_2HF_3O_2$ or H_3PO_4) in addition to the H_2SO_4/$KMnO_4$ mixture. The presence of the second acid (*e.g.*, H_3PO_4) inhibits the creation of vacancies in the GNRs due to the protection of the diol groups [31]. Interestingly, the degree of oxidation can be adjusted by controlling the amount of the oxidizing agent ($KMnO_4$) in the reaction. This process results in much longer (>5 mm) and narrower ribbons (<100 nm), with sharper edges (*i.e.*, more atomically perfect) [31], when compared to previous reports in the literature (see Fig. 2.4). Jiao et al. reported a plasma etching method for unzipping CNTs to form graphene nanoribbons [32] (Fig. 2.3b). In

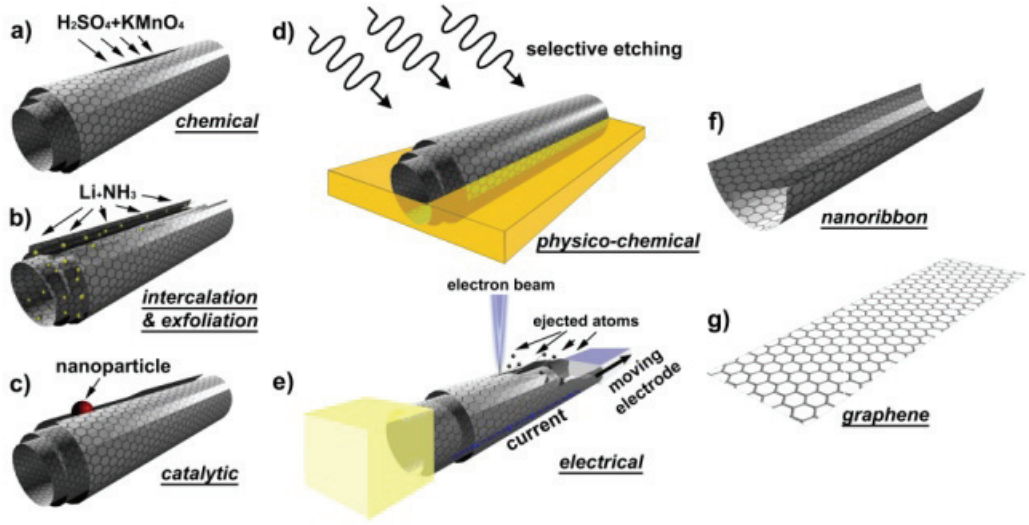

Figure 2.3 Schematic representation of the method used for unzipping carbon nanotubes to form graphene nanoribbons: (a) chemical route, involving acid reactions that start to break carbon-carbon bonds (*e.g.*, H_2SO_4 and $KMnO_4$ as oxidizing agents); (b) intercalation-exfoliation of MWNTs, involving treatments in liquid NH_3 and Li, and subsequent exfoliation using HCl and heat treatments; (c) catalytic approach, in which metal nanoparticles "cut" the nanotube longitudinally like a pair of scissors, (d) physico-chemical method, by embedding the tubes in a polymer matrix followed by Ar plasma treatment; and (e) the electrical method, by passing an electric current through a nanotube. The resulting structures are either (f) GNRs or (g) graphene sheets. (Images are adapted from Ref. [33]).

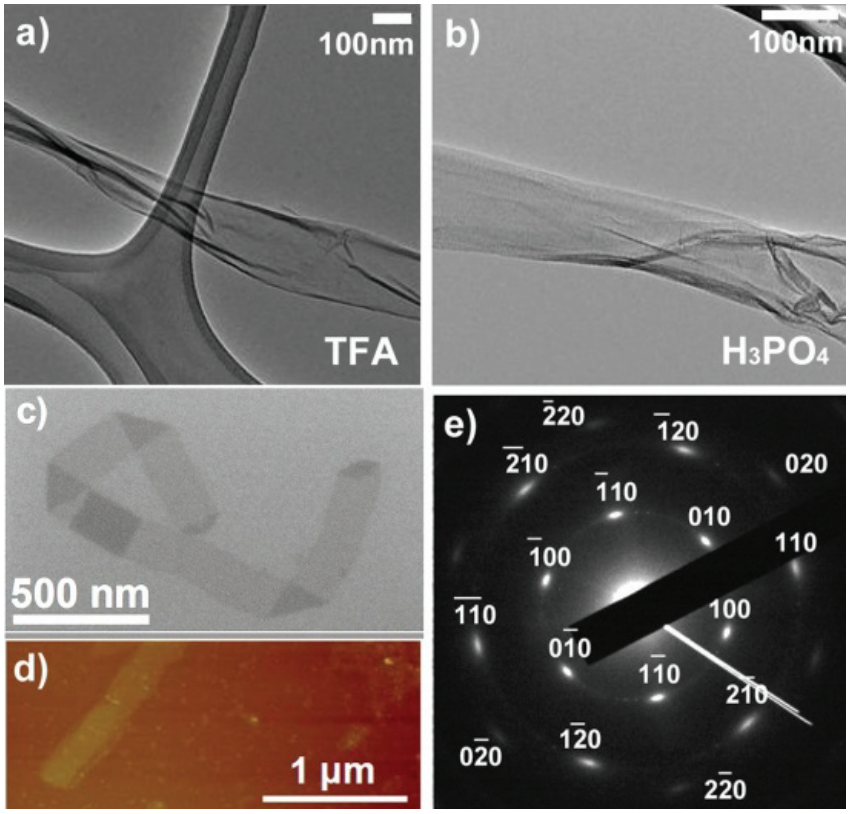

Figure 2.4 Graphene nanoribbons produced by unzipping carbon nanotubes with an efficient chemical oxidation process. (a,b) Transmission electron microscopy (TEM) images of graphene nanoribbons obtained by unzipping CVD-grown multiwalled carbon nanotubes, using an optimized method involving two acids (TFA or H_3PO_4) in the presence of $KMnO_4$ and H_2SO_4 at 65 °C; (c) TEM image of a graphene nanoribbon showing various bends produced using the method by Higginbotham et al.; [31] (d) atomic force microscopy (AFM) image of a graphene nanoribbon segment produced by an optimized oxidation method using a second acid (H_3PO_4) at 65 °C, in addition to $KMnO_4$ and H_2SO_4. (e) An electron diffraction pattern of a few-layer graphitic nanoribbon obtained using the same conditions as those shown in panel (d). Note the bright spots in (e) correspond to the hexagonal lattice. (Images adapted from Ref. [33])

this case, the resulting nanoribbons are 10-20 nms wide, and typically 1-3 graphene layers thick, and show semiconducting properties. Another unzipping method consists of intercalating nanotubes using alkali-metal atoms (e.g. Li, K, Na) and washing out the intercalants. This procedure causes the tube to open along its length. This approach was first reported using Li intercalation in conjunction with ammonia (NH_3) [34] (Fig. 2.3b). A previous study has shown that transition metals can cut through graphene sheets under hydrogen flow

conditions [35,36]. This method can also be used for cutting MWCNTs into GNRs (Fig. 2.3c) through a method of selective etching. A method for the facile synthesis of high-quality graphene nanoribbons has been reported more recently [37]. This method involves two steps in each of the gas phase and liquid phase steps. In the mild gas-phase oxidation step, oxygen reacts with pre-existing defects on the nanotube sidewalls to form etch pits. In the subsequent solution-phase sonication step, sonochemistry and hot gas bubbles enlarge the pits and unzip the tubes. The GNRs thus obtained show smooth edges in the HRTEM image and also show a low (I_D/I_G) ratio in the Raman D and G band spectra indicating a low defect density. These GNRs show the highest electrical conductance and mobility reported thus far for 10-20 nm wide graphene nanoribbons [37]. An alternative method for unzipping carbon nanotubes has been developed by Zettl and co-workers and it consists of passing a high current through a carbon nanotube inside an electron microscope [38].

Unzipping of nanotubes to yield GNRs appears to be a very promising technique in terms of mass production. This is mainly because several companies around the world, are now able to produce massive quantities of carbon nanotubes per year using the CVD process. However, the atomic control of the edge morphologies of the GNRs still needs to be enhanced and scaled up, in order to take advantage of the special properties of graphene nanoribbons.

2.2.3 Other methods

In addition to the approaches summarized above, STM lithography has been used to cut graphene nanoribbons from graphene sheets [39]. Graphene ribbons with a typical width ranging from 2.5 nm to 15 nm, and a length of ~120 nm were produced in this way, with a measured bandgap of about 0.5 eV for a 2.5 nm-wide armchair GNR using room temperature STS measurements [39]. The advantage of using STM lithography is that it is possible to pattern bent junctions with nanometer-precision, as well as to produce a predetermined width and crystallographic orientation of the nanoribbons; such features are hard to

achieve presently using other cutting techniques. This advantage stems from the possibility of achieving excellent atomic resolution using STM on flat graphitic surfaces. However, STM lithography suffers from low throughput and equipment accessibility, two issues that make it unlikely for this technique to be used in large-scale applications. Another chemical method for atomically precise bottom-up fabrication of GNRs has recently been developed by Cai et al. [40], which involves a precursor monomer on a gold substrate that forms GNRs through dehalogenation and cyclodehydrogenation steps. This method produces GNRs with well controlled widths and various shapes. However, challenges remain in fabricating these GNRs on a technology relevant substrate, or in transferring the GNRs onto an arbitrary substrate.

2.3 Characterization of graphene nanoribbons and edges

Graphene edges are investigated using a variety of characterization techniques. Advanced transmission electron microscopes (TEM) are commonly used in evaluating graphene edge structures, and Raman spectroscopy is advantageous for distinguishing zigzag from armchair edges and for studying the chirality-dependent edge disorder and the quantum confinement of the electrons in 1D band structures. The use of scanning tunneling microscopy (STM) and spectroscopy (STS) for studying the electronic states at graphene edges is also a promising research field, and STS/STM can be used to study the magnetic properties of graphene edges, which is reviewed in detail in Ref. [41].

2.3.1 Transmission electron microscopy (TEM)

High resolution transmission electron microscopy (HRTEM) is a highly sensitive tool for studying graphene edges. Graphene edges in each layer typically exhibit a dark line in the TEM image, which enables counting the number of layers in as-synthesized graphene samples [42,43]. The edge roughness can also be directly estimated using HRTEM imaging.

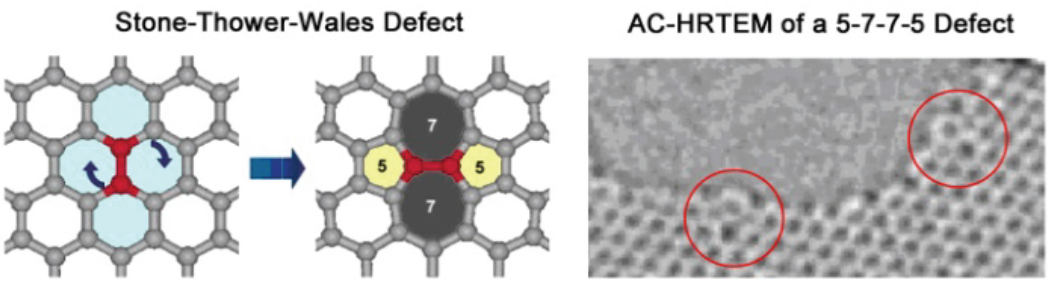

Figure 2.5 (Left) Molecular model showing the transformation of 4 adjacent hexagons into a 5-7-7-5 defect or a Stone-Thrower-Wales defect, and (right) an HRTEM image showing two 5-7-7-5 defects located on the edges (red circles) of a hole in a graphene surface. (Images are taken from movies from supplementary material of Ref. 40).

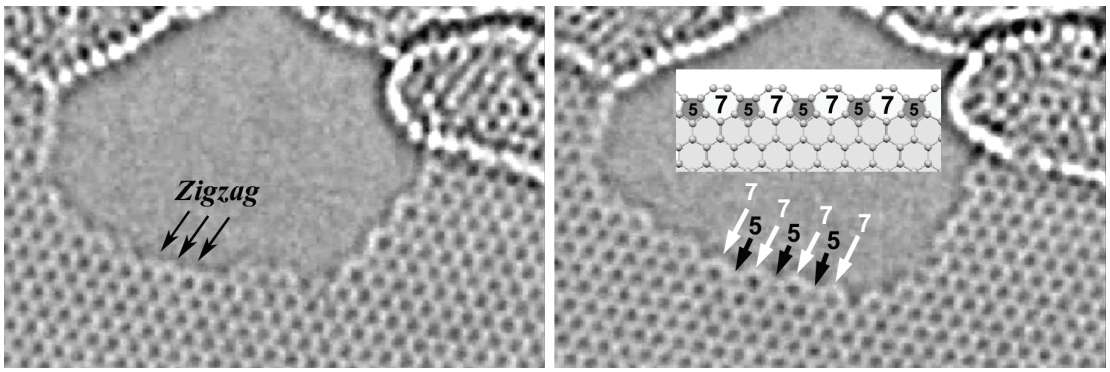

Figure 2.6 HRTEM images showing a zigzag edge near a hole region of a graphene layer *(left)* transformed into a 5-7 defect edge *(right)*. (Images are adapted from movies in the supplementary material of Ref. 40).

Significant progress has been reported in the TEM characterization of graphene edges [21,44-51]. Zettl and co-workers [50] have been able to directly observe 5-7 and Stone-Thrower-Wales (STW) [52,53] bulk defects as well as 5-7 edge defects on isolated graphene surfaces using aberration-corrected transmission electron microscopy (see Fig. 2.5 and Fig. 2.6).

In order to resolve the atomic structures at graphene edges, advanced TEM techniques are required. Using an aberration-corrected TEM instrument combined with a monochromator (TEAM 0.5), which has sub-Angstrom resolution, the stability of mechanically exfoliated graphene edges under electron beam irradiation has been studied in real time. Under these conditions, edge atom reconstruction is observed (see Fig. 2.5). The abundance of zigzag edges lends evidence for a more stable zigzag configuration under these conditions [50]. In

Ref. [48] open and closed (folded) edges in exfoliated HOPG materials have been studied under conditions when such edges are stable. After furnace annealing at ~2000ºC, open edges are found to become less stable so that most of the open edges join with edges in the neighboring layer to form well-stacked loops. Finally, note that Ref. [49] reports on the *in situ* observation of graphene sublimation and multi-layer edge reconstructions at elevated temperatures.

2.3.2 Raman spectroscopy

Compared to the TEM characterization of graphene edges, Raman spectroscopy provides a complementary, yet quite different characterization tool that is also suitable for distinguishing between zigzag and armchair edges in graphene nanoribbons and studying edge disorder. It has been found that the Raman peak of nanographite ribbons (on a HOPG substrate) exhibits an intensity dependence on the light polarization direction relative to the nanographite ribbon axis [54], as shown in Fig. 2.7a. The Raman spectrum here is composed of two peaks centered at 1568 cm^{-1} (G_1 peak) and 1579 cm^{-1} (G_2 peak). The G_2 peak frequency, which remains unchanged when varying the polarization angle (θ) of the incident beam with respect to the ribbon axis direction, comes from the HOPG substrate. In contrast, the G_1 feature in Fig. 8a comes from the nanographite ribbon, and its intensity varies with the polarization of the incident light. The intensity decreases with increasing θ and can be fitted to a $\cos^2 \theta$ curve (Fig. 2.7b). This curve originates from the relationship between the probability of light absorption $W(\vec{k})$ and the wave vector of the electron k written as

$$W(\vec{k}) \propto \frac{\left|\vec{P} \times \vec{k}\right|^2}{k^2} \qquad (2.1)$$

where $\vec{P}$ is the polarization vector of the incident light. Since van Hove singularities occur in the $\vec{T}$ direction (θ = 0) due to the 1D quantum confinement structure in the density of states, a large Raman signal is obtained when the light

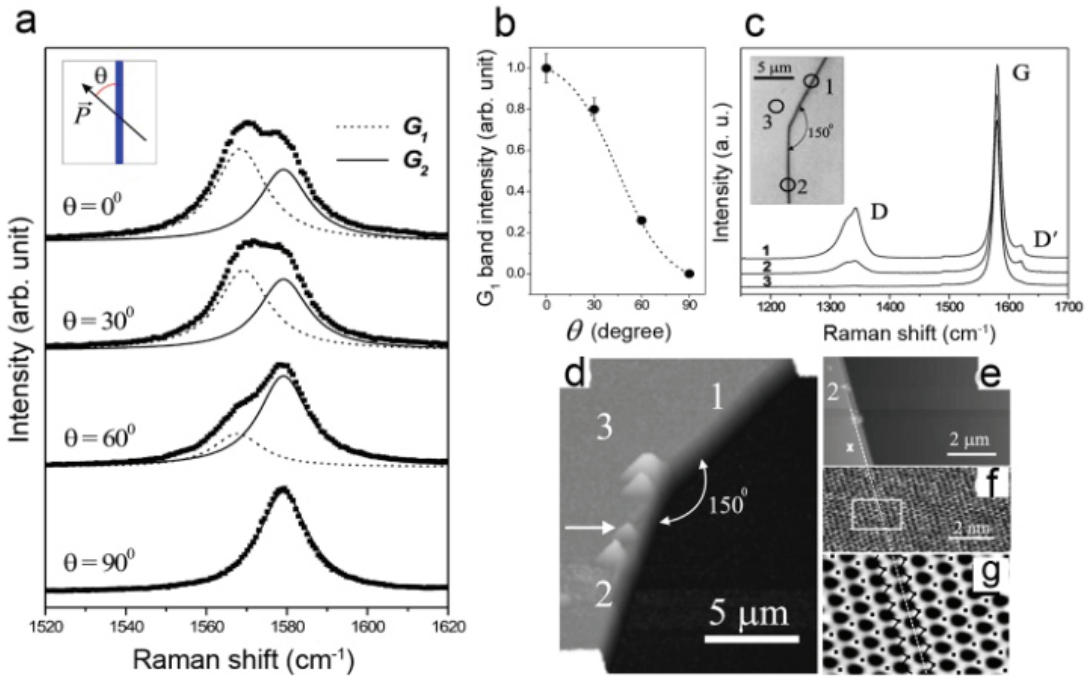

Figure 2.7 Raman spectrum of GNR edges [54,55]. (a) Raman spectra obtained for light incident with different polarization angles (θ) with respect to the ribbon axis direction in nanographite ribbon sheets. The inset shows a schematic figure of the sample (vertical gray line) denoting the direction between the ribbon axis and the light polarization vector. (b) Intensity of the G_1 Raman peak versus θ. The dotted line is a $\cos^2$ θ theoretical fit to the experimental points. (Images (a) and (b) are adapted from Ref. [54]). (c) Raman spectra obtained in three different regions of an HOPG sample (see (d)). The inset in (c) shows an optical image of an edge region of a sample and the regions where spectra 1, 2 and 3 were taken (open circles). (d-e) AFM images of the step on the HOPG substrate where the Raman spectra shown in (c) were taken. (f) The STM measurements and (g) The FFT (fast Fourier transform) filtered image verifying the zigzag edge configuration in the marked region 2 in (c, d). (Images (c)-(g) are adapted from Ref. [55]).

is in resonance with the excitonic optical transition energies E_{ii} between Van Hove singularities. The Raman G-band intensities are, therefore, different for interior regions of a nanographite and at the edges. The G-band intensity of a GNR is also dependent on the GNR width and crystalline direction. Thus it is only the electronic $\vec{k}$ vector along the $\vec{K}_T$ direction that is involved in the optical absorption process. When θ = 0, then we have $\vec{k} // \vec{K}_T$, and G_1 reaches its maximum value; however, when θ reaches 90º, the G_1 peak should vanish and a

$\cos^2\theta$ dependence of the intensity is obtained, as shown in Fig. 2.7b. This polarization dependent behavior allows the Raman technique to distinguish between armchair and zigzag edges.

For example, Figs. 2.7d-g show the influence of the edge structure on the Raman spectra of edges in HOPG [55]. The edge configurations shown here are determined by STM measurements. It is found that the disorder-induced D band in the Raman spectra also provides a powerful way to distinguish armchair from zigzag edges. Here we see that the D band intensity is about 3 times less intense for a zigzag edge (spectrum 2) compared to that for an armchair edge (spectrum 1), when normalized to their G band intensities. The residual intensity of the D band from the zigzag edge is attributed to disorder in this edge structure and also to D band itself which is related to a symmetry breaking. This shows that the observation of the D-band could be useful for characterizing the defect structure in nanographite-based devices. Recent calculations of the Raman spectra of graphene ribbons including the effect of the matrix elements of the Raman tensor [56] represent a first step in a quantitative approach to using the Raman G-band scattering intensities to distinguish between armchair and zigzag edges.

2.3.3 Defective edges

The most common defects one finds in graphene nanoribbons are: vacancies, heptagon-pentagon pairs (STW transformations), loops and interstitials. While heptagon-pentagon pairs and loops preserve the connectivity of the nanoribbon, the interstitials and vacancies do not. Therefore, scientists must now work on defect edge engineering in order to tailor the reactivity and transport properties of graphene edges. For example, defect edge engineering could perhaps be used to achieve specificity for sensing different types of molecules or to anchor specific polymer groups at the edges of GNRs, in order to produce stable and well dispersed composites or suspensions. In addition, electronic and thermal transport measurements are important to study the effect of specific and

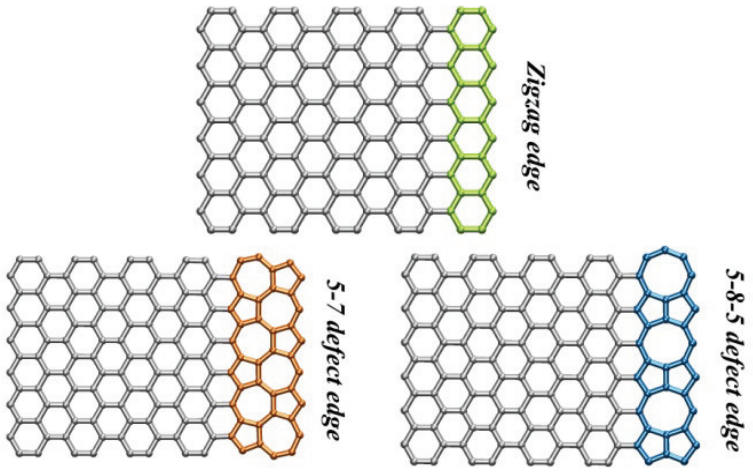

Figure 2.8 Schematics of graphene nanoribbons with a perfect zigzag edge, and edges with 5-7 defects and 5-8-5 defects, respectively. (Image courtesy of L. P. Wang, MIT)

controlled defects on the edges of graphene. It is clear that the edge chemistry and physics of GNRs, a field which is just emerging, could lead to unexpected catalytic reactions, novel field effect transistors, efficient electrodes for Li-ion batteries, anchoring centers for assembling heavy metals, highly conducting and transparent films, drug delivery devices, and other applications.

Further studies considering edges having pentagon-heptagon (5-7) or pentagon-octagon-pentagon (5-8-5) rows (as schematized in Fig. 2.8) need to be carried out in detail from both experimental and theoretical points of view. For example, very recently, Batzill and coworkers identified the presence of a 5-8-5 defect line within a graphene sheet using STM [57]. These defect lines behave as quantum wires. This finding indicates that other defect topologies should also be considered and studied. In addition, Botello-Méndez, et al. also demonstrated that hybrid ribbons interconnecting zigzag and armchair nanoribbons behave as spin polarized conductors [58]. Finally, it is also possible to have non-carbon atoms within either ribbons or graphene using heteroatomic doping atoms, such as B and N [59-64]. These systems need to be studied further along with the presence of defects on the edges caused by the introduction of non-hexagonal rings [22].

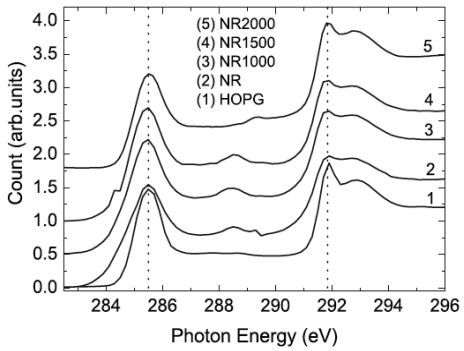

Figure 2.9 Carbon K-edge NEXAFS spectra of the pristine graphene NR, NR1000, NR1500, and NR2000. The pristine sample (NR) and HOPG are also given for comparison. The count value for HOPG given in the figure is reduced to half of the original count to make it comparable with the other traces. The C 1s to π^* (285.5 eV) and σ^* (291.85 eV) transitions are indicated by dotted vertical lines. (Image is adapted from Ref. [65]).

Very recently, Joly, et al. [65] investigated the edge states in graphene nanoribbons prepared by the CVD method, using near-edge x-ray absorption fine structure (NEXAFS) and electron spin resonance (ESR) spectroscopy. It was noted that the C 1*s* to π^* transitions of nanoribbon samples, correspond to the C 1*s* to edge-state transitions of nanographenes. As the CVD ribbons were annealed at high temperatures in an Ar atmosphere, the contribution of the edge states decreased due to the loop formation. These results confirmed the presence of magnetic edge states in the edges of graphene nanoribbons and provided significant insight into these magnetic edge states (see Fig. 2.9).

2.4 Summary

Since 2004, the research on graphene edges has attracted increasing attention and has undergone rapid progress. The fabrication of graphene edges and graphene nanoribbons has made significant advances within the last two years towards the large scale production of smooth edges and narrow ribbons. With the stringent demands of electronic device applications and the desire to continually promote fundamental physics studies, more efforts in improving the synthesis conditions as well as the post-growth treatment procedures of graphene edges are

foreseeable. In the meanwhile, the characterization of graphene edges has also progressed significantly and is now pushing the limit of nanomaterials characterization techniques. Integrated characterization techniques, such as combined STM with TEM, combined Raman spectroscopy with other electron microscopy techniques, are likely to take place, which will facilitate our understanding of advanced nanomaterials and their development towards applications. In addition, study of the magnetoresistance of graphene nanoribbon-based FETs is another emerging research field that is likely to gain more momentum towards various applications [66].

Although extensively investigated in the laboratory, the fabrication of graphene edges in electronic device applications is still facing many challenges, including the creation of both smooth edges and controlled narrow graphene ribbons that can open a sizable and well-defined bandgap and there are still many open issues and opportunities for further research effort. Given the short history of this field, the progress has been impressive and significant developments in graphene edge applications are expected to occur in the near future.

Chapter 3

TEM characterizations of CVD grown graphene and BN films

In chapter 2, I have introduced the recent research progress on graphene nanoribbons and their edges, focusing on their fabrication and characterization. This chapter will present our work on utilizing HRTEM and advanced TEM analysis tools to characterize CVD grown graphene and boron nitride (BN) thin films, and this work may also assist our understanding of the materials growth mechanism. The TEM characterization of graphene and BN nanomaterials introduced in this work will form the baseline for the next two chapters, where a more complex *in-situ* TEM technique is utilized for structural characterizations as well as for the description of the structural modifications.

3.1 CVD grown graphene

The first experimental production of graphene was realized by a micro-cleavage method from HOPG materials [6]. These are high quality materials with truly two dimensional single crystalline structures. However, this micro-cleavage method involves tedious laboratory work, and can only produce small area graphene flakes (on the order of micrometers), and for this reason it is not a suitable method for large scale industrial applications. The chemical vapor deposition (CVD) method for graphene growth, on the other hand, can produce large sheets of graphene, and the graphene size is only limited by the substrate size and the furnace conditions. So CVD grown graphene is in this sense ideal for industrial applications. The materials quality, such as the crystallinity, continuity, and layer number control, then becomes major questions for CVD grown graphene. The best suited technique for measuring these properties is TEM due to its atomic resolution capabilities and easy sample preparation.

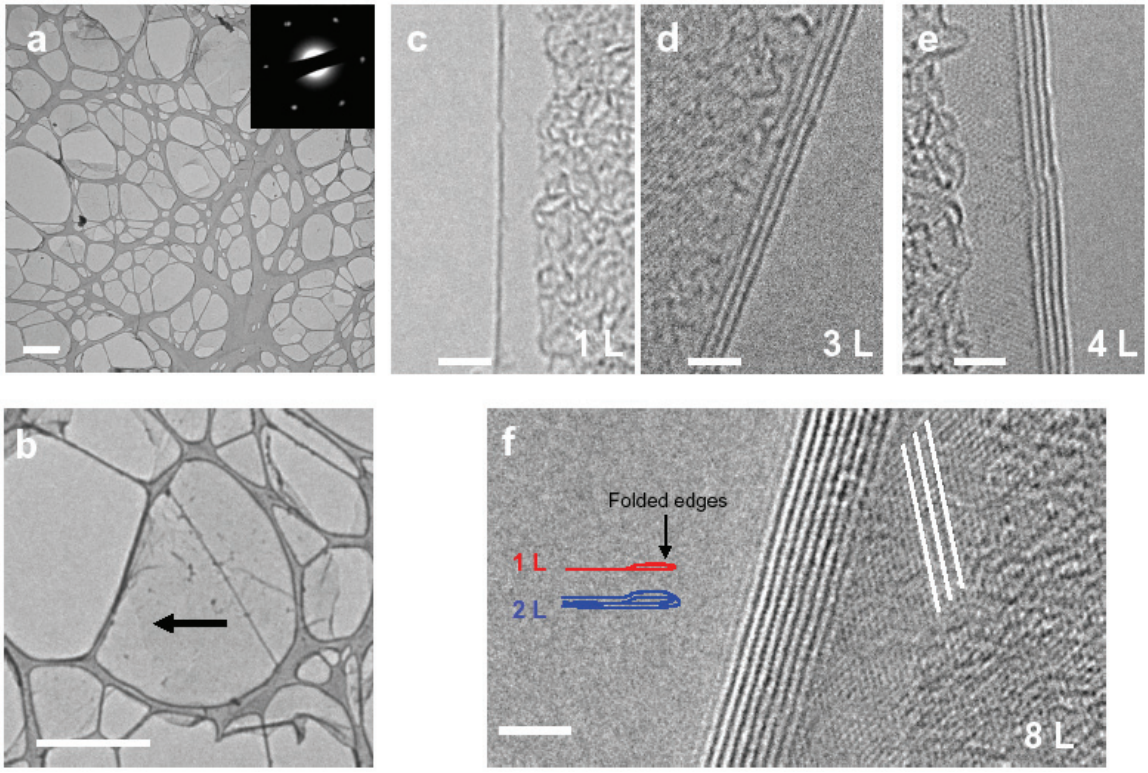

Figure 3.1 TEM images of large area, few layered graphene films grown by the CVD method. (a) A large area graphene film is transferred onto a lacey carbon TEM grid, and the inset shows its selected area diffraction pattern exhibiting a single crystal hexagonal structure. (b) A higher magnification TEM image shows a one-to-two layer boundary on the graphene film (indicated by the black arrow). (c)-(f) The thin films are as thin as 1 to 8 layers, and measurements of the inter-plane (center of (f)) and in-plane (near the right half of (f)) lattice spacings confirmed the highly crystalline structure of the material. Scale bars in (a-b) are 2 μm. Scale bars in (c-f) are 2 nm. [67]

Large area, few layer graphene films grown on Ni foil substrates using the CVD method was first produced by our collaborator Alfonso Reina [67]. These materials were characterized within a JEOL 2010F TEM operated at 200 kV (see Figures 3.1). After CVD growth on Ni, these graphene films can be transferred to arbitrary substrates using a chemical wet etching method [67]. Large area thin films down to 1 to 8 graphene layers are observed in these films (see Figures 3.1c-f). The selected area diffraction pattern (inset of Figure 3.1a), and the interlayer and in-plane lattice spacing measurements confirm that the structures of the CVD grown films are close to those of HOPG-derived films with high crystallinity.

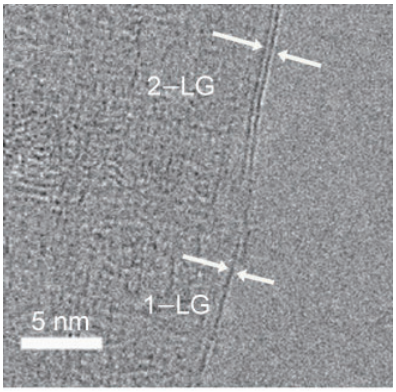

Figure 3.2 A TEM image of large area, single and double layer graphene edges. [68]

Furthermore, it has been shown that it is possible to grow graphene films with up to 87% of their area composed of no more than two graphene layers (2-LG) and these films can also be transferred to insulating substrates [68]. This was accomplished by controlling both the carbon concentration and the substrate cooling rate during the CVD process. Under a suitable carbon concentration (0.5% CH_4 in our case), the cooling rate can be utilized to decrease the number of nucleation sites for multilayer graphene on the film (by a factor of two) and to increase significantly the area covered by sections with 1-2-LG. In order to confirm this 1-2 layered structure, I conducted TEM measurements of the samples grown by Alfonso Reina. A TEM image of a single layer and bilayer graphene edge is shown in Figure 3.2. This result suggests the possibility of dramatically improving the thickness uniformity of graphene films by further controlling the process parameters in our method. Therefore, ambient pressure CVD may be a viable route to control the growth of single graphene layers over large areas.

3.2 CVD grown BN thin films

BN films have similar structures as graphene films, forming two dimensional hexagonal lattices. They have an atomic surface relatively free of dangling bonds and charge traps, unlike conventional silicon oxide substrates; they also possess

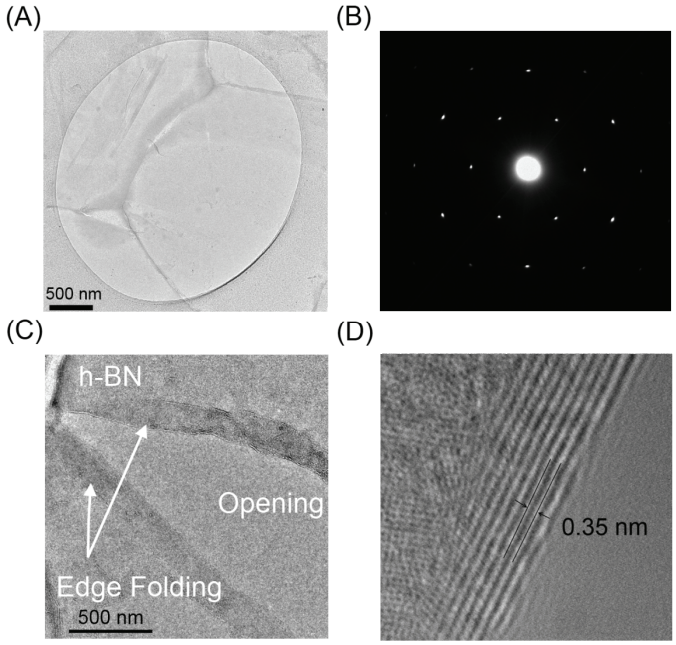

Figure 3.3 TEM images of h-BN thin films grown on Ni films. (A) Low-magnification TEM image shows a CVD-grown *h*-BN film on Quantifoil holey carbon grids. (B) Electron diffraction pattern of the *h*-BN thin film taken from the suspended region shows a hexagonal dotted pattern indicating a single crystal structure in the h-BN. (C-D) TEM images of the *h*-BN thin film are taken under different magnifications. (C) The TEM image shows a broken part of *h*-BN thin film and the edge folding. (D) High resolution TEM image shows the edges of a 8-9 layer BN film with an interlayer spacing of about 0.35 nm. [70]

high frequency optical phonon modes and a large electrical bandgap (~ 6.4eV), making them an ideal substrate for graphene devices [69]. However, the synthesis of ultra-thin large area BN films is still at an early stage. BN thin films can be obtained from micro-cleaving of bulk single crystal BN. In order to produce large area BN thin films, a CVD method similar to graphene growth has also been used in our work [70], and the materials grown under different conditions are characterized and compared using TEM.

The first CVD grown few-layer hexagonal BN (h-BN) films were produced by our collaborator Yumeng Shi. These h-BN films are synthesized by ambient pressure CVD on polycrystalline Ni films, by exposing polycrystalline Ni to borazine ($B_3N_3H_6$) vapor with N_2 gas flow. The as-grown BN films are then transferred onto a TEM grid by wet-etching the underlying Ni, and structural characterizations are performed in a JEOL 2010F TEM operated at 200 kV.

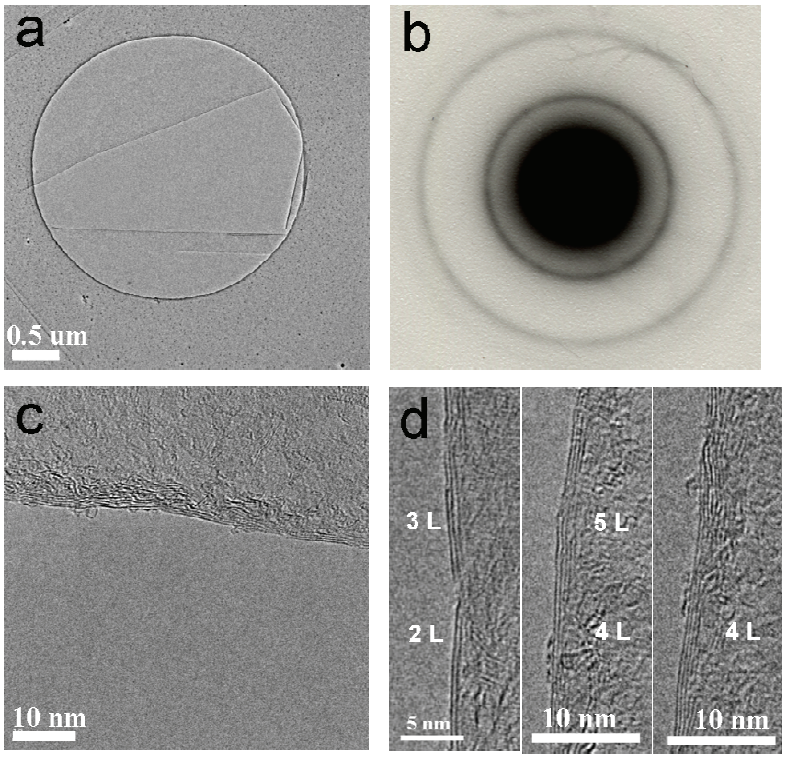

Figure 3.4 TEM images of h-BN thin films grown on Cu foils. (a) TEM image shows a broken region of a CVD grown BN thin film on a Quantifoil holey carbon grid. (b) Electron diffraction of the BN thin film shows a polycrystalline structure. (c) A higher magnification TEM image shows a typical BN thin film edge. (d) High resolution TEM images of the BN film edges show that the thin films contain 2-5 layers.

Figure 3.3 shows typical TEM images and the diffraction pattern of the CVD grown h-BN thin films. The thickness of the BN films is between 5 and 50 nm, and the regions with a uniform thickness can be up to 20 μm in lateral size. The material also has high crystallinity as indicated by the diffraction pattern in Figure 3.3B. A high resolution TEM image measured at the edges of an 8-9 layer BN film (Figure 3.3D) confirms the highly crystalline structure. The interlayer spacing between adjacent layers is measured to be about 0.35 nm, consistent with the theoretical value in crystalline hexagonal BN films.

In order to obtain fewer layer BN films, an alternative CVD growth method is used by our collaborator Ki Kang Kim. This growth method uses copper foil substrates instead of Ni films. Borazine ($B_3N_3H_6$) vapor and H_2 gas are introduced at a high temperature, followed by annealing at temperatures

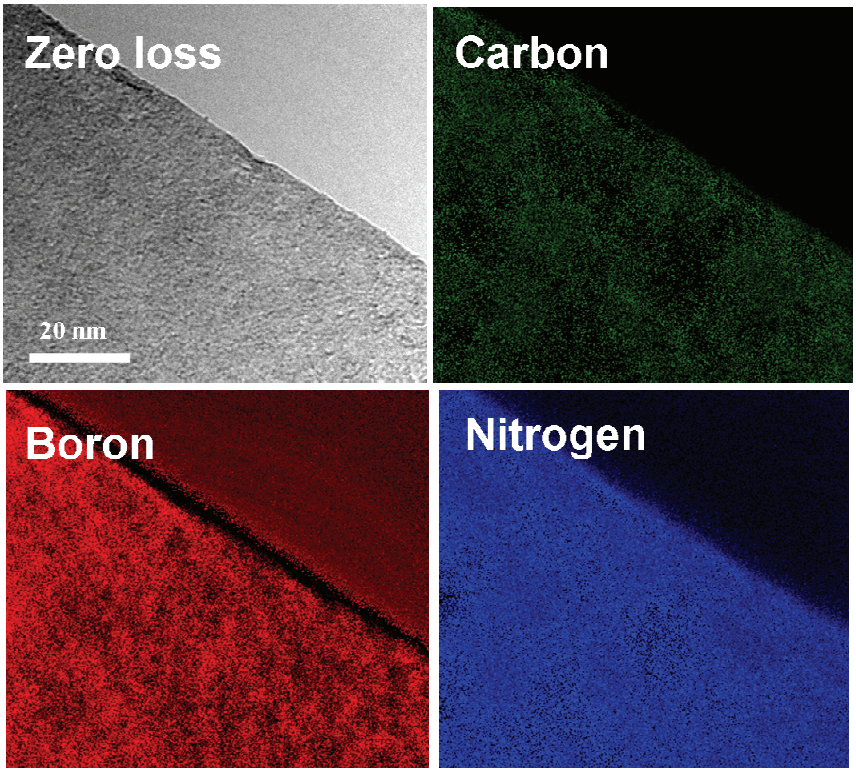

Figure 3.5 Energy filtered mapping of the composition of a suspended CVD grown BN thin film.

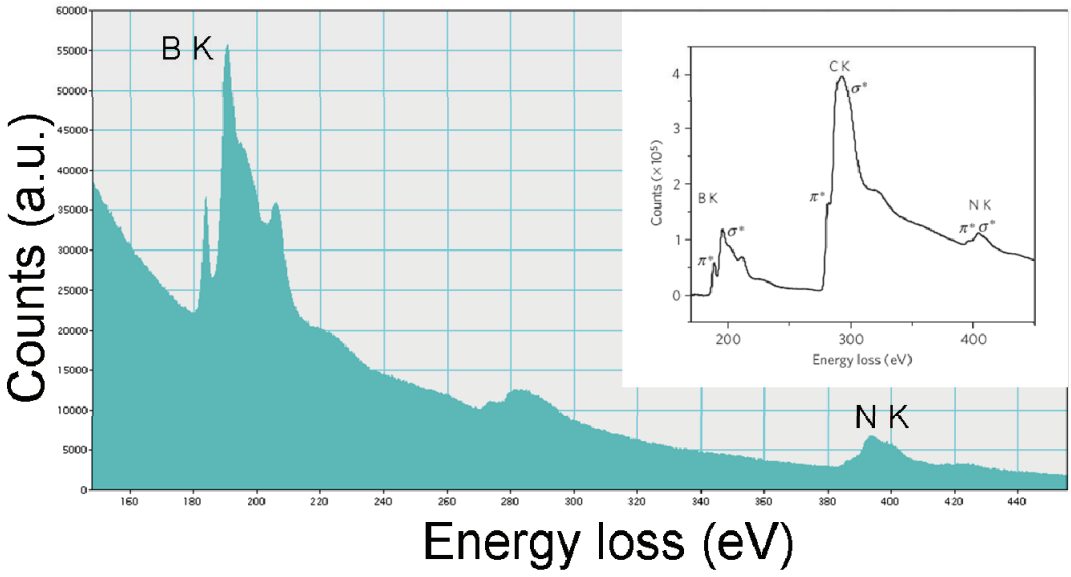

Figure 3.6 Electron energy loss spectrum of the CVD grown BN thin film. The inset is a spectrum adapted from Ref. [59] for comparison.

above 1000^0C with H_2 and N_2 gas flow. The as-grown BN films are also transferred to TEM grids for detailed characterizations. The high resolution TEM images (Figures 3.4c-d) indicate that the BN films grown on a copper foil substrate are ultra-thin containing only 2-5 layers, much thinner than the previous h-BN samples grown on Ni films. The diffraction pattern (Figure 3.4b) indicates that these BN thin films are polycrystalline, different from the previous sample grown on Ni substrates. Different CVD growth mechanisms between the Ni growth and Cu growth can be expected.

Electron energy loss spectrum (EELS) in scanning transmission electron microcopy (STEM) and energy filtered mapping are used to conduct elemental analysis on these BN thin films. The elemental mapping of carbon, boron and nitrogen (see Figure 3.5) atoms shows that boron and nitrogen atoms are uniformly distributed over the BN film surface. The weak signal for carbon atoms may come from the polymer residue left after the wet-etching process. The EELS measurement on the BN thin film (see Figure 3.6) shows π^* and σ^* peaks at the B K edge and the N K edge, indicating that B and N atoms are forming sp^2 bonding.

3.3 Summary

In summary, in this chapter we have shown that HRTEM and advanced TEM analysis tools (such as EELS and energy filtered mapping) are well suited techniques for characterizing CVD grown graphene and BN thin film materials. The materials quality including the crystallinity, the thickness, the layer uniformity, atomic distribution and bonding types (sp^2 or sp^3) can be measured using TEM and STEM. The results show that large area, few layer graphene materials with high crystallinity are grown using ambient pressure CVD and Ni film substrates, highly crystalline h-BN thin films with 5-50 nm thickness are grown on Ni substrates, and ultra-thin polycrystalline BN films with 2-5 layer thickness are grown on Cu substrates. The TEM characterization may assist our understanding of the materials CVD growth mechanisms.

Chapter 4

Formation of sharp zigzag and armchair edges in graphitic nanoribbons by *in-situ* Joule heating

In this chapter, a novel method is developed for modifying the rough edges in graphitic nanoribbons to produce atomically smooth edges by *in-situ* Joule heating.

4.1 Background

Graphene, a single sheet of graphite, has attracted a lot of research interest since it first became experimentally accessible in 2004 [4,6,10,18,42,43]. Its two-dimensional structure and the near massless behavior of its charge carriers provide unique transport properties. Graphene nanoribbons, which are quasi 1D graphene nanostructures, exhibit a bandgap between the valence and conduction band states. The bandgap depends on both the edge type and ribbon width [18], which is typically a few nanometers, making graphene nanoribbons a very interesting material for potential electronics applications [27]. Theoretical and experimental studies show that the edges of graphene nanoribbons strongly influence their electronic and magnetic properties [41,71]. Therefore, much effort has been devoted to studying the edges in graphitic nanomaterials [39,54,55,72-77]. Although atomically smooth edges are essential for many applications, it is difficult to produce such edges by conventional physico-chemical methods. For example, lithographic etching and chemical methods usually provide rough edges [19] which contribute to carrier scattering. Furthermore, characterizing the edges and identifying the edge structures has been a challenge. In this chapter I will introduce a novel method for modifying

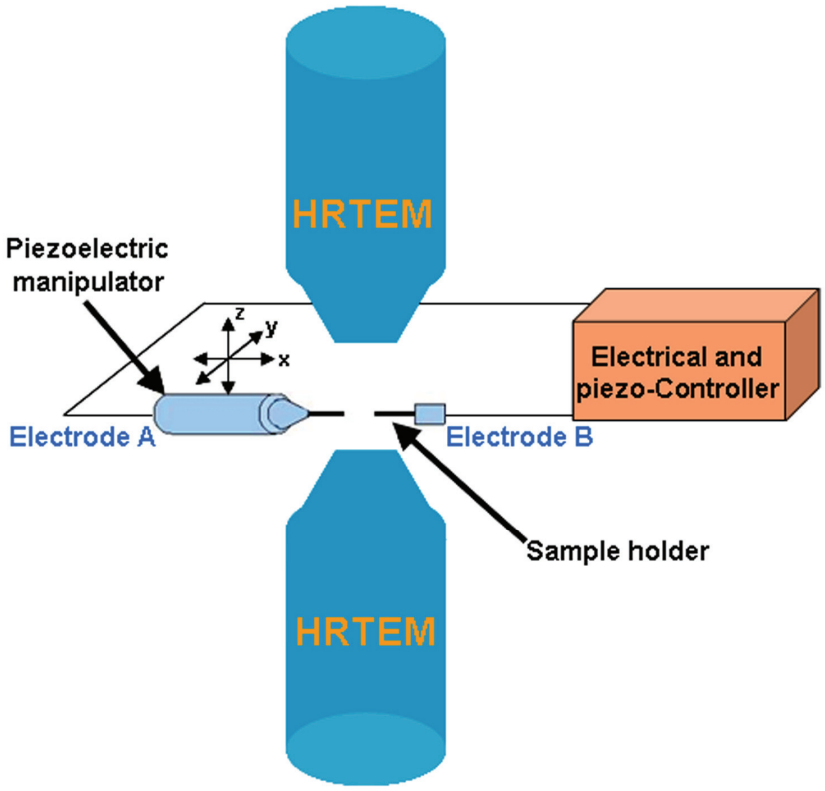

Figure 4.1 A schematic diagram of the integrated TEM-STM system for simultaneous structural and electrical measurements.

the rough edges in graphitic nanoribbons to produce atomically smooth zigzag and armchair edges, using an in-situ Joule heating method. The edge modification mechanism and graphene interlayer stacking will also be discussed here.

4.1.1 *In-situ* TEM

The experiments were conducted inside a JEOL 2010F TEM equipped with a Nanofactory STM holder (see Figure 4.1). The STM tip is further connected to a piezoelectric stage, which enables us to move the STM tip in different directions and to manipulate nanostructures inside the TEM. The STM tip and sample holder also serve as two electrodes where a bias voltage can be applied between these two electrodes, and the electrical current can be measured. This TEM-STM system enables us to make two point electrical measurements across a graphitic

nanoribbon length, while we simultaneously observe the structural behavior under the HRTEM [78].

4.1.2 A novel graphitic nanoribbon material

The graphite nanoribbon samples were produced by a single-step chemical vapor deposition (CVD) process [28]. In short, an aerosol was produced from a solution containing ethanol, ferrocene, and a very small concentration of thiophene. This aerosol was pyrolyzed at 950 ºC for 30 minutes, and after that time, the system was allowed to cool down to room temperature.

As stated in Ref. [28], the presence of S is crucial for synthesizing the graphitic nanoribbons. We could not detect S on the flat areas of the ribbons using EDX or XPS because the detection limits of these instruments were higher than 1 at%. However, it is quite possible that lower concentrations of S are present in highly curved areas (e.g. along the ribbon ripples or in regions containing heptagons or pentagons, such as 5-7 Stone-Thrower-Wales defects), a result which is consistent with previous experimental findings as well as theoretical calculations. Regarding the Fe atoms coming from ferrocene, we never found them on the ribbon sites. Nevertheless we believe that individual atoms of S, Fe and O are somehow bonded to the graphitic sheets (e.g., as adatoms or atoms within the hexagonal lattice) so that under Joule heating and electron irradiation, these atoms are likely the first to move towards the ribbon edges and to detach from the carbon network at low voltages. However at high voltages (1.6V), these atoms no longer play such an important role in the reconstruction process because of the high temperature that is reached in the Joule heating process, in contrast to the catalytically driven edge cutting process reported by Ci, et al. [35].

4.2 Sharp edge formation by in-situ Joule heating

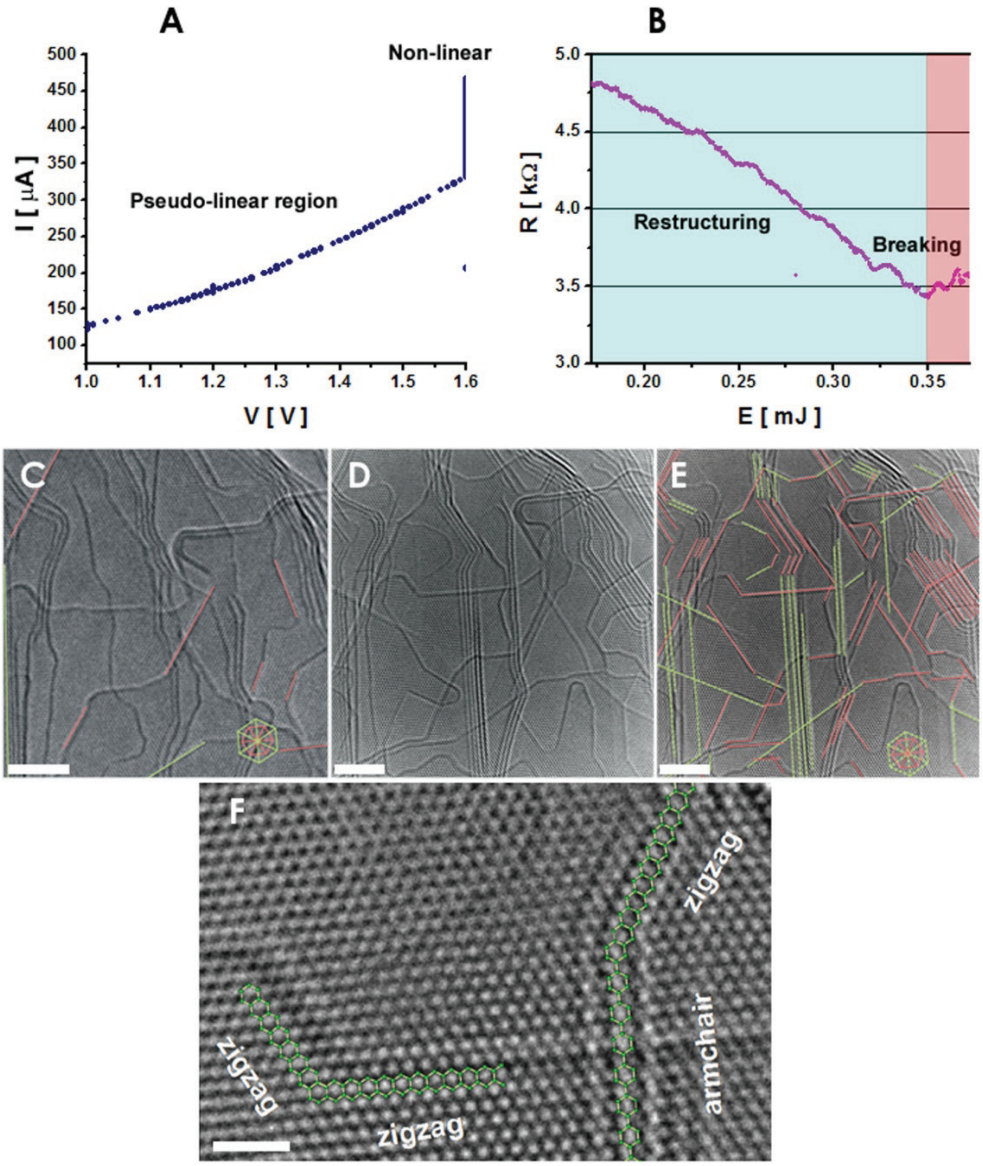

Figure 4.2 The crystallization and edge formation in graphitic nanoribbons. (A) The I vs. V curve during Joule heating, indicating three regimes: a quasi-linear regime from 1 V to 1.25 V, a slowly increasing slope regime from 1.25 V to 1.6 V, and a rapidly increasing slope regime at 1.6 V. (B) The resistance vs. input energy at 1.6 V applied bias. (C) The ribbon sample before Joule heating, showing very few zigzag edges (marked with pink lines) and armchair edges (marked with green lines). (D) The same ribbon sample after Joule heating (for 10 minutes at 1.6 V), in which most of the edges seen are either zigzag or armchair edges, as indicated in (E). The inset hexagons indicate the zigzag or armchair edge orientations associated with the lattice patterns in (C) and (E). (F) A high magnification image of the annealed sample showing that well-defined zigzag-armchair and zigzag-zigzag edges are formed. The green hexagons in (E) help with the identification of the atomic structure at the armchair and zigzag edges. (The scale bars in C, D and E are 4 nm, and the scale bar in F is 1 nm).

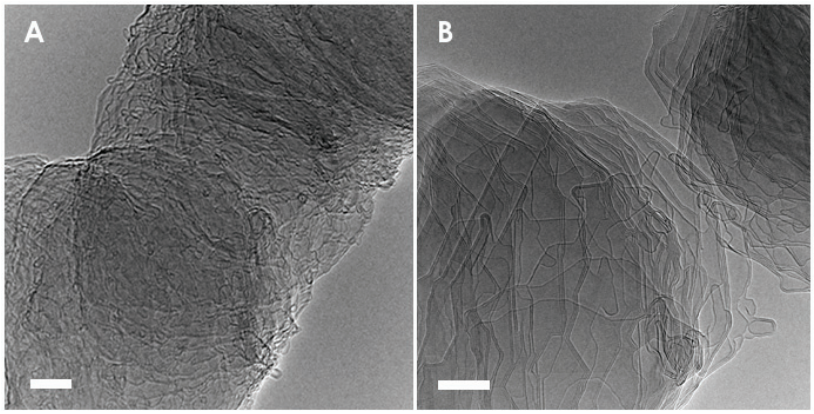

Figure 4.3 HRTEM images of the nanoribbon sample (A) before and (B) after Joule annealing for 20 min at 1.6 V. (scale bar = 10 nm)

With the integrated TEM-STM system, we are able to produce atomically smooth zigzag or armchair edges from defective rough edges that are observed in as-prepared graphitic nanoribbons [28].

An individual nanoribbon sample is attached to the sample holder at one end, and to the STM tip at the other end, and these two ends also serve as the two electrodes. As we apply a voltage (up to 1.6 V) over the length (315 nm) of a 66 nm wide ribbon, the I *vs.* V curve shows (Fig. 4.2A) the onset of a non-linear regime (1.6 V) where the resistance decreases with increasing input energy (Fig. 4.2B). As current flows, the degree of crystallinity of the ribbon improves rapidly (Fig. 4.2C-D), and the sample thickness decreases, until all the graphene layers evaporate and the sample breaks from the middle (see Fig. 4.3B). From the edge terminations observed in Fig. 4.2E, we conclude that the majority of edges are either zigzag or armchair after Joule heating. It is noteworthy that in the lower voltage (quasilinear) regime below 1.6 V (see Fig. 4.2A), carbon atoms mainly vaporize due to knock-on effects caused by the electron irradiation [79], and edges start reconstructing via Joule annealing. However, at higher applied voltages (1.6 V), the preferred reconstruction-crystallization effects induced by the high temperature caused by Joule heating are seen in going from Fig. 4.2C to Fig. 4.2D, indicating that the activation energy of atoms forming zigzag or armchair edges is lower than for other edge configurations. Other types of edges are seen infrequently since a mixture of zigzag and armchair edges are

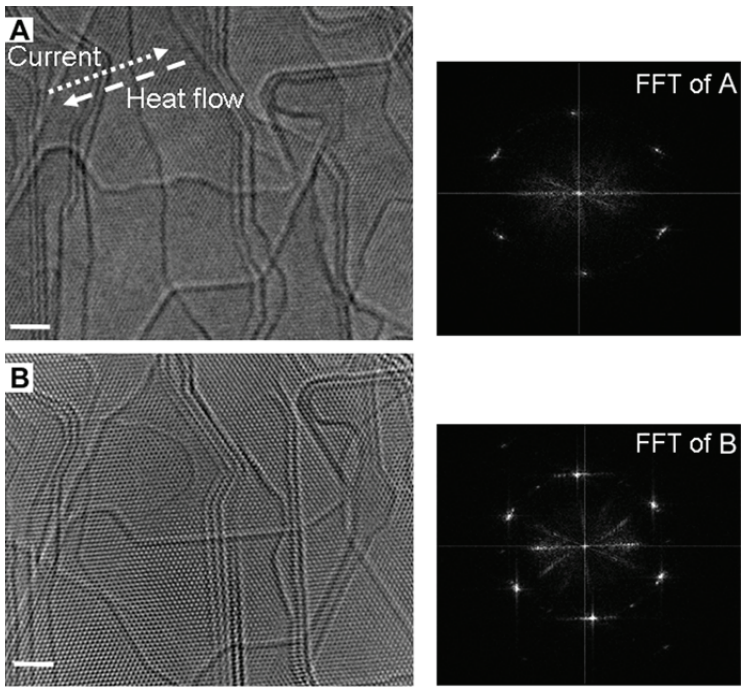

Figure 4.4 TEM images of the same region of the ribbon sample (A) before and (B) after annealing, and their Fast Fourier Transform (FFT) images (on the right of each image) show clear development of the crystallinity and edge quality after annealing. (Scale bars are 2 nm.)

metastable because of the energy penalty at the edge junctions. Figure 4.2F depicts the reconstructed graphitic material shown in Figure 4.2D. The measured in-plane lattice spacing for our ribbons is 0.24 ± 0.02 nm, consistent within the accuracy of our TEM measurements with literature values in graphite (which is $\sqrt{3}\, a_{c\text{-}c}$ where $a_{c\text{-}c}$ is the nearest-neighbor carbon-carbon distance [80]). As a result of carbon atom vaporization and Joule heating, the defective graphitic edges in the as grown nanoribbon sample crystallize (Fig. 4.4), and finally become atomically sharp and highly crystalline. The maximum length of the smooth edges observed after the process in Fig. 4.2E is about 29 nm. The mechanism of reconstruction or crystallization for the nanoribbons and edges is attributed primarily to the carbon atom vaporization, the current flow along the ribbon and edges, and the high temperature associated with the resistive Joule heating.

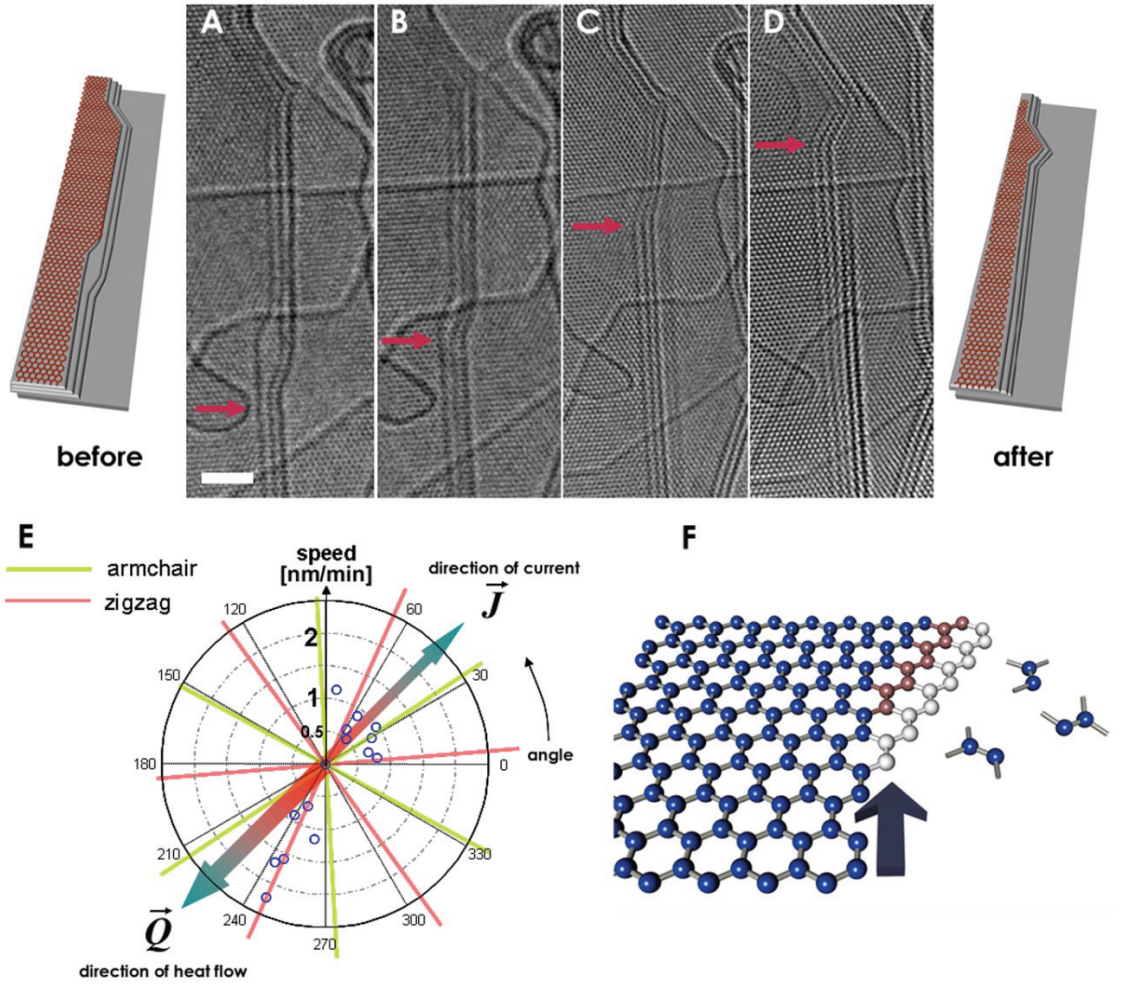

Figure 4.5 Edge motion under Joule heating inside the TEM. (A) A three-layer zigzag-armchair-zigzag-armchair edge array. The red arrow indicates the position of the zigzag-armchair edge junction at the beginning of the annealing process. After some time of Joule heating, the junction moves up (B)-(C), keeping the short zigzag edge length almost unchanged. Eventually, the zigzag edge joins with the upper zigzag edge, forming a stable zigzag-zigzag-armchair edge array (D). The sketches on the left of (A) and on the right of (D) are the simulated structures of (A) and (D), respectively. (E) Plot of the speed (in the radial direction) and angle (in the counter clockwise direction) of the edge motion relative to the current and heat flow directions. (F) A scenario for the motion of carbon atoms near edges and edge junctions, as C_2 dimers are evaporated from edges. As a row of the carbon atoms near the zigzag edge move away from the edge (first white colored balls and then red colored balls) upon heating, the zigzag-armchair edge junction (indicated by a dark black arrow) moves upward by $3a_{c\text{-}c}$. (The scale bar is 2 nm).

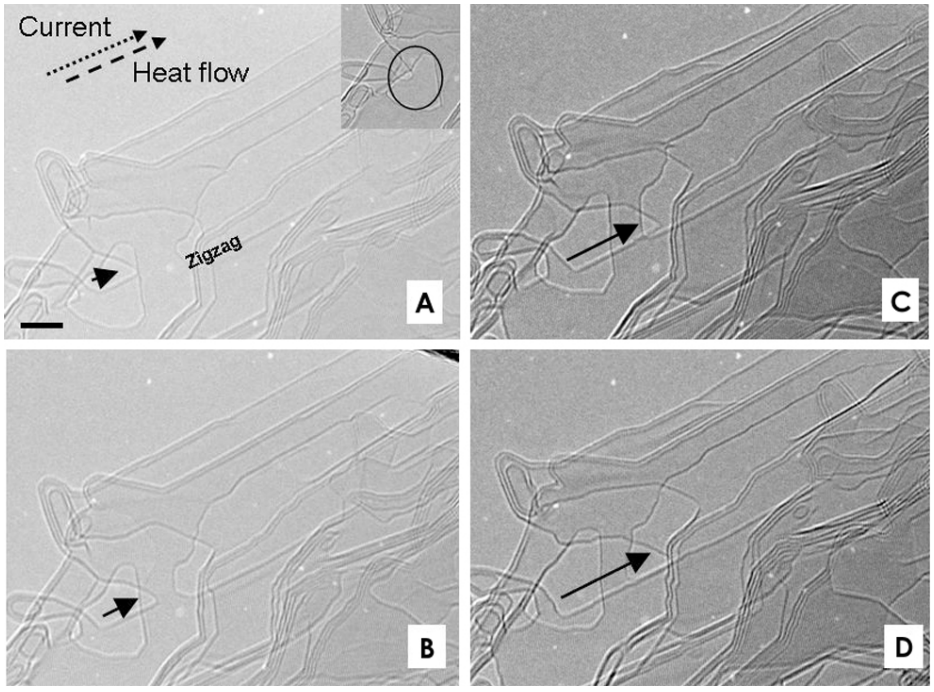

Figure 4.6 (A)-(D) Successive TEM images show a zigzag edge of a single graphene layer (indicated by the solid arrow) moving into the interior region of the graphene along both the current and heat flow direction, while keeping the zigzag edge configuration unchanged. (The scale bar in A is 4 nm.)

The dynamics of the edge reconstruction is shown in Figs. 4.5A-D and Fig. 4.6. In Figs. 4.5A-D we see a time resolved sequence of a three-layered graphene edge structure placed on top of another few-layered graphene sheet with a zigzag- armchair-zigzag-armchair edge configuration forming 150° angles (note that the angles between the zigzag and armchair edges can be 30°, 90° or 150°). As we apply a bias voltage of 1.6 V (high annealing temperatures), the armchair edge above the zigzag edge starts to evaporate, resulting in the upward movement of the zigzag edge (red arrow) with a speed of 2.3 nm/min. This low speed at the investigated high temperatures indicates that the necessary activation energy is much larger than the activation energy of defect migration observed by Iijima et al. [81] in carbon nanotubes. Eventually, as shown in Fig. 4.5D, the armchair edge is eliminated, and the lower zigzag edge joins with the upper zigzag edge and forms a stable zigzag-zigzag junction.

In Fig. 4.5E the edge motion direction and speed are plotted for 14 experiments over the ribbon sample, similar to that shown in Figs. 4.5A-D. From

Fig. 4.5E we see that the edge motion mostly follows either zigzag or armchair crystallographic orientations, and that the speed of edges moving along the heat flow direction $\vec{Q}$ (from the middle of the ribbon to the two electrodes which act as heat sinks) is higher (e.g., 2 nm/min) than that along the current flow direction $\vec{J}$ (from the STM probe to the sample holder) when the two are anti-parallel (e.g., 1 nm/min). Edge motion along other directions is not favored. A scenario for the dissociation of carbon atoms from edges and the resulting motion of the edge junctions is given in Fig. 4.5F.

4.3 Mechanism for edge modification

The graphitization steps of carbon at high temperatures have been described by Goma and Oberlin [82,83]. Here the graphitization process ultimately results in the thermal crystallization of wavy and wrinkled layers into long in-plane crystalline domains by ~2100 ºC with c-axis stacking order starting to develop above 2300 ºC and identified with crystalline graphite. For our ribbon samples, we observed the transformation of AA stacking into ABAB stacking, and we attribute these transformations mainly to the high temperatures reached (e.g. 2000 – 2500 °C) in the non-linear voltage regime. In order to verify that a high temperature is achieved by resistive Joule heating in the suspended graphitic nanoribbons, Pt nanoparticles were deposited on an as-prepared ribbon. Upon Joule heating (with an applied bias below 2V), the Pt nanoparticles evaporate from the center region of the nanoribbon surface, thus indicating that a high temperature is achieved by Joule heating along the freely suspended ribbon (see detailed discussion in Chapter 6).

The reason why thermal energy is dissipated at an edge hetero-junction is because it is the location of the largest electrical resistance. Therefore, quasi-metallic (zigzag edged or one third of armchair edged graphene nanoribbons [84]) systems should be preferred. Joule heating involves both current flow and atomic vibrations. Carbon nanoribbons do not show any specific phonon associated with

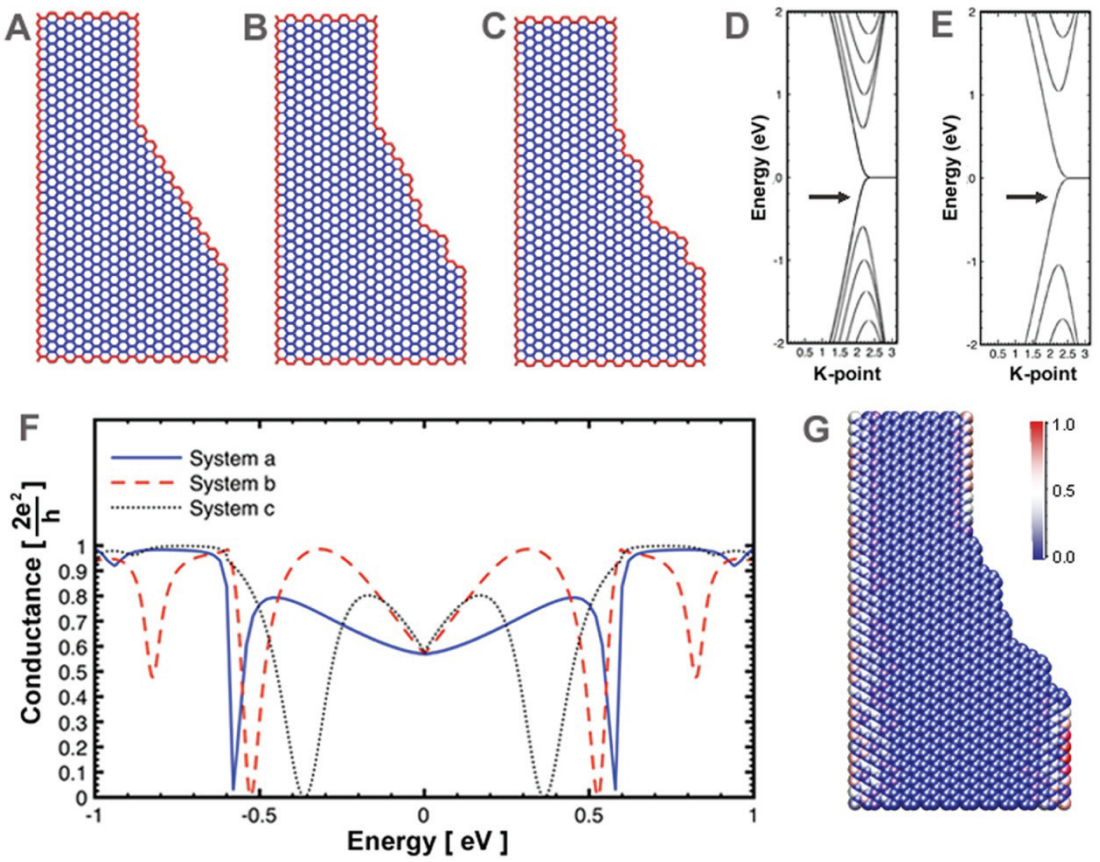

Figure 4.7 Electronic and transport properties of graphene nanoribbon heterojunctions based on a single -orbital tight-binding model (the Fermi energy is located at E = 0 eV). (A)-(C) three models considered here where the details of the edges are highlighted in red. In each case, the two electrodes consist of two zigzag edge nanoribbons (N_{zig} = 44 and N_{zig} = 24, using the notation from Ref. [85]). The electronic properties of the individual electrodes are represented in (D) and (E) for the large and small ribbons, respectively. The conductance versus energy corresponding to systems (A)-(C) is presented in (F). For system (C), the amplitude of the scattered wave-function (current-carrying state) is shown in (G); it is normalized such that the maximum amplitude is 1. The figure in (G) confirms that close to the Fermi level, the current-carrying state, in the zigzag taper is localized along the zigzag edges (zero amplitude at the inner part of the figure) and that the tapered part of the junction presents a high electrical resistance. [21]

a given edge type (there is no special phonon localized on the edges themselves) [86]. Point (localized) defects are associated with large amplitude vibrations and these are likely to be annealed first. In addition, zigzag edged graphene ribbons are the only graphene structures which have electronic states that are localized

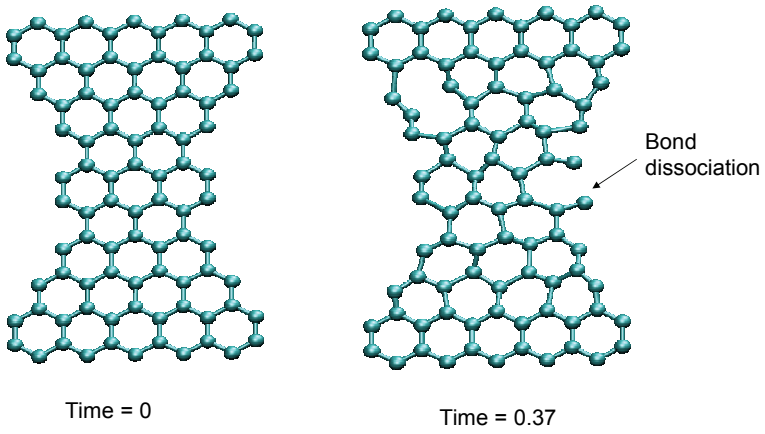

Figure 4.8 Snapshots taken from a quantum molecular dynamics calculation of a zigzag-armchair-zigzag junction by Bobby Sumpter showing the dissociation of the bond at the zigzag-armchair junction. (The unit of time is picoseconds).[21]

along their edges [71]. Since the electronic dispersion is quite large (Figs. 4.7D-E), the electronic flow in zigzag-edged nanoribbons occurs mainly along these zigzag edges. When a zigzag edge meets a non-zigzag edge, the electronic flow is reduced and the system acts as if a large resistance were introduced at the junction. Therefore, additional heating will result and this heating will cause electron flow away from the edge junction, or if enough energy is dissipated at the junction, will result in a modification of the structure. In that case, provided that sufficient energy is dissipated in this manner, the atomic structure will rearrange locally (Fig. 4.8) until electronic flow is reestablished. Starting from a zigzag edge, this can take place if the structure is annealed into a zigzag edge. For this reason, zigzag-zigzag junctions are the favored junction formation (see Figure 4.2). This zigzag edge formation mechanism is therefore local, since it is due to a high local resistance at the edge intersection.

To verify this hypothesis, we considered the three junctions shown in Figs. 4.5A, B, and C, which differ in the structure of the tapered edge; in Fig. 4.5A the junction is made by an armchair edge, while the junctions in Figs. 4.5B and 4.5C

are a mixture of edge geometries. The conductance of the heterojunctions between zigzag and armchair edges is considerably reduced, due to the fact that transmission is hindered on those non-zigzag edges where no electronic state is present. The scattering amplitude of a current-carrying state close to E = 0 eV is shown in Fig. 4.5G, highlighting the appearance of a large, localized resistance where the zigzag edge is interrupted. This resistance in turn results in local heating and subsequent annealing into an all-zigzag edge system.

A non-local transformation mechanism can be invoked to account for the formation of semi-metallic conducting armchair edges. For larger current flow, the structure can also anneal into a conducting armchair edge system, as the current is allowed to flow, albeit not along the edges themselves. The effect is non-local in nature because, even though the edge structure governs the semi-metallicity of the whole structure, the current flow in the non-local case mostly appears away from the edges.

4.4 Graphene interlayer stacking

Experimentally, it is found that more zigzag edges are initially formed at high temperature, which is an indication that local processes are dominant. Conversely, armchair edged ribbons, although found in less abundance, are considerably longer (Figs. 4.2 and 4.5), lending support to an operative non-local mechanism. We should also mention that armchair edges evaporate easily when compared to the zigzag edges (see Fig. 4.5). MD calculations (Fig. 4.8) show that a C-C unit located at the armchair edge dissociates preferentially; the energy required to vaporize a C-C unit from an armchair edge is 6.7 eV while that of a zigzag edge is considerably higher (ca. 11 eV).

The Joule annealing process and its associated current flow, create stable “edge arrays” (see Fig. 4.2D, and Figs. 4.5A-D). These “edge arrays” indicate that an offset is present between the edges of two adjacent layers. The results of a careful measurement of the edge-to-edge distances in these “edge arrays” is plotted in Fig. 4.9A, which shows clear peaks at 0.34 nm, 0.38 nm and 0.43 nm

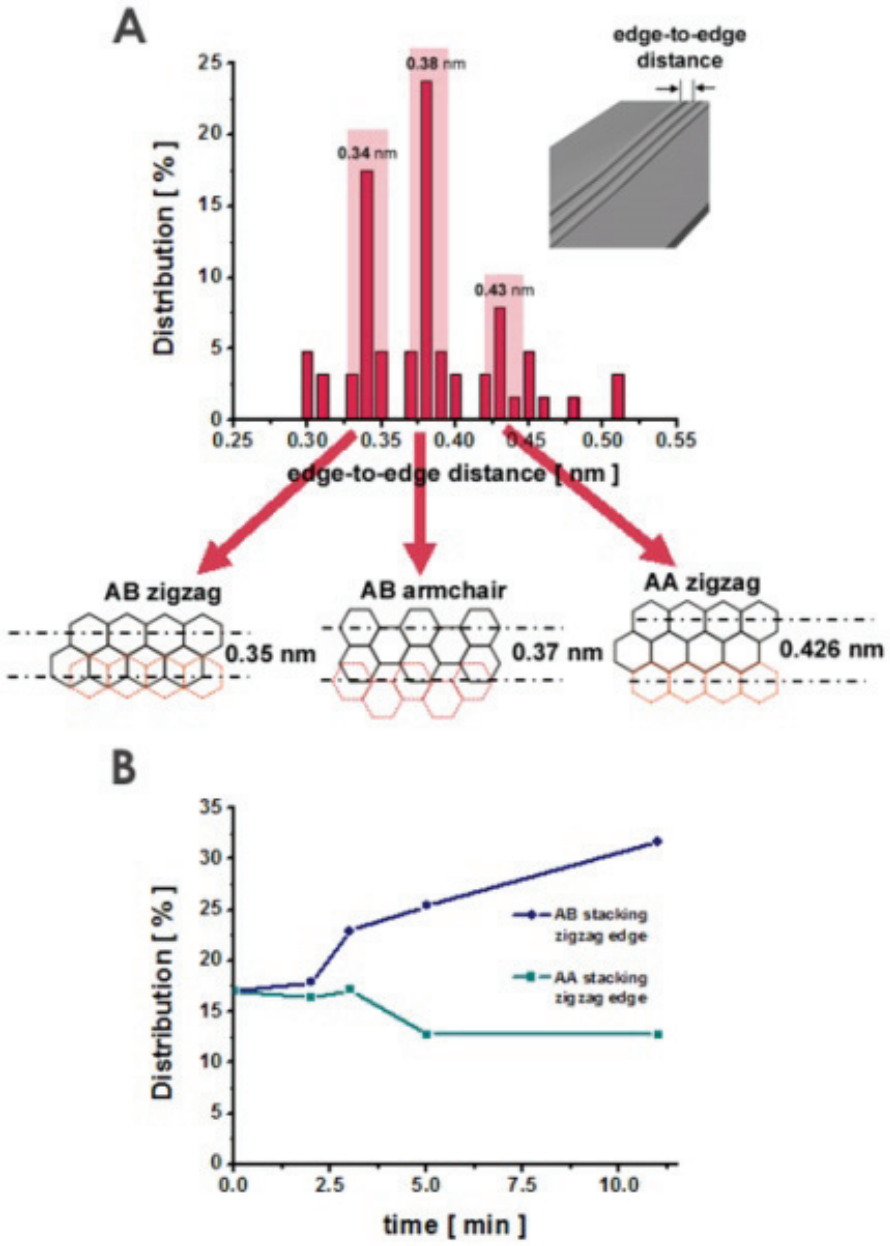

Figure 4.9 Edge arrays and their time evolution. (A) The experimental edge-to-edge distances in the edge arrays show three peaks at 0.34 nm, 0.38 nm, and 0.43 nm. These peaks correspond to the offset of two adjacent AB stacked zigzag edges, AB stacked armchair edges, and AA stacked zigzag edges, respectively, as indicated in the inset of (A). (B) Of all the edges obtained from analysis of Fig. 1D, the percentage of AB stacked zigzag edges increases from 17% to 32%, while the percentage of AA stacked zigzag edges decreases from 17% to 13% after a 10 minute anneal, indicating that the AB stacked layer configuration is more stable than AA stacking. (Error of points is 2%).

edge-to-edge distances. These distances correspond to the offset of adjacent edges of differently stacked graphene layers (see Fig. 4.9A). Of particular interest, the evolution of the edge arrays (see Fig. 4.9B) after 10 minutes of irradiation and Joule annealing shows a clear increase for the AB stacked zigzag edges and a decrease of the AA stacked zigzag edges. This is attributed to the fact that the ABAB stacked configuration is thermodynamically more stable than AA stacking [87], and consistent with the Goma-Oberlin mechanism [83].

4.5 Summary

In summary, we demonstrated the efficient shaping of graphitic nanoribbon edges into zigzag or armchair edges via Joule heating inside a TEM-STM system. This structural transformation is mainly attributed to the vaporization of carbon edges that are reconstructed at high temperatures, in which the resistive Joule heating and the preferred current flow along specific edges play a vital role. The theoretical edge evolution model reveals that the specific edge formation is stimulated as a means to provide an easy path for current flow between intersecting zigzag and conducting armchair edges. This suggests that the efficient formation of all zigzag edge ribbons could be achieved by careful limitation of the flowing current. These results open up a possible way of generating atomically well-defined edges that may make graphene-based electronics possible.

Chapter 5

Folded edge and open edge formation

In this chapter we will introduce the synthesis of the novel graphitic nanoribbon material (section 5.1) followed by a discussion of folded edge (loop) formation in this novel material by furnace annealing (section 5.2) and by Joule heating (section 5.3). Theoretical calculations show that electron beam irradiation plays a significant role in determining either folded or open edge formation, which is presented in section 5.4. Finally we conclude with a summary discussion for loop formation in these nanoribbons (section 5.5).

It has been reported that when graphitic materials are subjected to high temperatures (e.g. >1500 °C), the ends of the graphitic sheets find a more stable configuration by forming a loop with an adjacent sheet [29,88-93], thereby healing the dangling bonds at the edge sites. These loops exhibit a diameter larger than the sheet-to-sheet separation of the graphene layers. Double and multiple layered loops have also been observed in these experiments. The loop formation phenomenon is surface driven and strongly involves the physics and chemistry of reactive edges and sp^2 hybridized surfaces and interfaces. This chapter focuses on the loop formation (folded edge formation) in graphitic nanoribbons based on furnace heating and Joule heating, and reports similarities and differences between the loops formed by the two complementary methods. The mechanism for open or folded edge formation by in-situ Joule heating is also presented in this chapter.

To the best of our knowledge, the first experimental observation of loop formation at the edges of graphitic layers was reported by Murayama et al. [29] in 1990 in furnace heat-treated graphite filaments. Since then, experimental evidence for loop formation has been provided in various furnace heat-treated graphitic materials [88-93], such as graphite polyhedral crystals [90] and cup-

stacked nanofibers [88]. The transitional evolution of such loops from active end planes to stable loop configurations caused by annealing was first reported by Endo et al. [89]. Iijima also reported that loops are formed from graphite edges after furnace heat treatment at 2000 °C for 3 hours [92,94] . Most recently, Campos-Delgado et al. reported defect annealing and loop formation in graphene nanoribbons for heat treatment temperatures up to 2800 °C and they also reported their transformational mechanism and properties [93].

Joule heating has also provided an efficient way to achieve high temperatures in many carbon materials, and it has been demonstrated that carbon nanostructures could be modified substantially by Joule heating, showing phenomena, such as the superplasticity of carbon nanotubes [94], wall-by-wall breakdown of multiwall carbon nanotubes [95], and the formation of tubular structures from amorphous carbon nanowires by Joule heating [78]. In particular, graphitic nanoribbons [28] represent an outstanding materials system to study edges and loop formation because of the high density of accessible end planes that are present in this material. Characteristic changes in the structure of graphitic nanoribbons have already been reported [93] when high temperatures come into play. In this chapter, we describe two routes to create loops on the edges of graphitic nanoribbons: one is through conventional furnace heating, and the other through Joule heating. A detailed description of the synthesis process of this interesting material is included at the beginning of this chapter, as well as a brief discussion of the morphology and structure of this material, obtained by electron microscopy. In this chapter, we also compare the results of loop formation for the two cases of Joule heating and furnace heating, showing both similarities and complementary behaviors.

5.1 Materials synthesis

The materials are synthesized by our collaborator Jessica Campos-Delgado. The experimental set-up used in the synthesis of graphitic nanoribbons [28] is shown

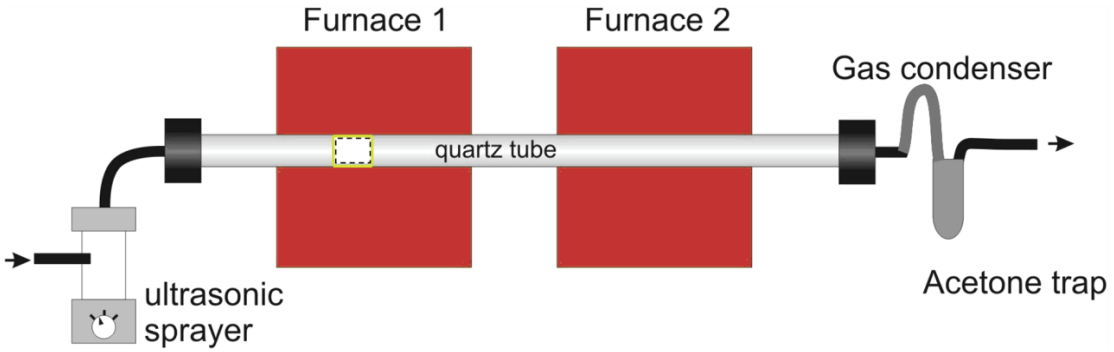

Figure 5.1 A schematic diagram of the experimental set-up used in the synthesis of graphitic nanoribbons. The yellow marked area in the tube within Furnace 1 corresponds to the region where the graphitic nanoribbon material is deposited during synthesis. [96]

schematically in Fig. 5.1, where all the necessary equipment is placed inside a fume hood. A quartz tube (~1.1 m long), connecting an ultrasonic sprayer and a gas condenser/acetone trap for the exiting gases, is placed inside two tubular furnaces (see Fig. 5.1). The length of each furnace is 40 cm and the separation between the two furnaces is ~15 cm. An inert atmosphere is maintained by flowing argon gas through the system. A solution containing 280 ml of ethanol, 2.8235 mg of ferrocene ($FeCp_2$) and 0.266 ml of thiophene (C_4H_4S) is prepared and placed inside the ultrasonic sprayer. During the heating of the furnaces, the ultrasonic sprayer is kept in a turned off setting and the flow of Ar is set to 0.2 l/min. Once both furnaces reach 950 ºC, the ultrasonic sprayer is turned on. The aerosol thus produced is carried to the hot zone of the furnaces by raising the flow rate to 0.8 l/min. These conditions are maintained for 30 min, after which the sprayer is turned off, the flow rate is decreased to 0.2 l/min, and the two furnaces are allowed to cool down to room temperature.

Once the system has cooled down, the quartz tube is taken out and the material of interest containing the nanoribbons is scraped from the walls of the tube. The nanoribbons are deposited as a powder within furnace 1 in a region between 12 and 20 cm relative to the left edge position of the first furnace (see Fig. 5.1).

The black powder containing the nanoribbons has been shown to be efficiently dispersible in various alcohols. We have used ethanol and methanol

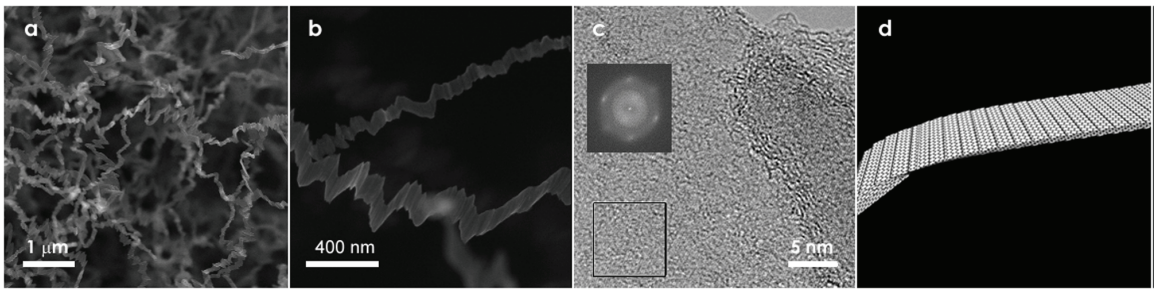

Figure 5.2 SEM and TEM images of as-produced graphitic nanoribbons. a) Low magnification SEM image, where a very clean material with no by-products is seen. b) A higher magnification SEM image of the same sample as in (a). c) TEM image of the surface of the nanoribbon, where the ribbon edge and the structure of a ripple are shown in the right-hand side of the image. The inset represents the FFT (fast Fourier transform) of the square region showing the six fold symmetry of the diffraction pattern. d) A simulated morphology of the ribbon samples showing the ripples as consisting of individual graphitic sheets with open edges. [96]

followed by sonication to create suspensions of graphitic nanoribbons. These suspensions have been used to prepare samples mounted on copper grid sample holders for use in scanning electron microscope (SEM) and transmission electron microscope (TEM) observations.

The morphology of the nanoribbons as observed by SEM and TEM is depicted in Fig. 5.2. A low magnification image of the as-produced nanoribbons is shown in Fig. 5.2(a). The dimensions of the nanoribbons range from 80-500 nm in width, up to 10-15 nm in thickness and many microns in length. The material shows ripples along the main axis, as observed in Fig. 5.2(b). Because of these ripples, the ribbons have a discontinuous appearance. It is also noteworthy that in our TEM observations, we could not find catalytic Fe particles attached to the material or embedded in the entangled nanoribbons.

TEM characterization of the graphitic nanoribbon material [28] reveals a crystalline structure with 001 planes parallel to the ribbon main axis. The FFT in the inset of Fig. 5.2(c) shows that the graphitic nanoribbons are crystalline, consistent with a honeycomb lattice structure. The nanoribbon structure is sketched in Fig. 5.2(d) to help clarify the essence of their structural morphology.

Elemental analysis by XPS showed that the nanoribbons consist of C and some oxygenated groups [28], which we believe are attached to the edges of the

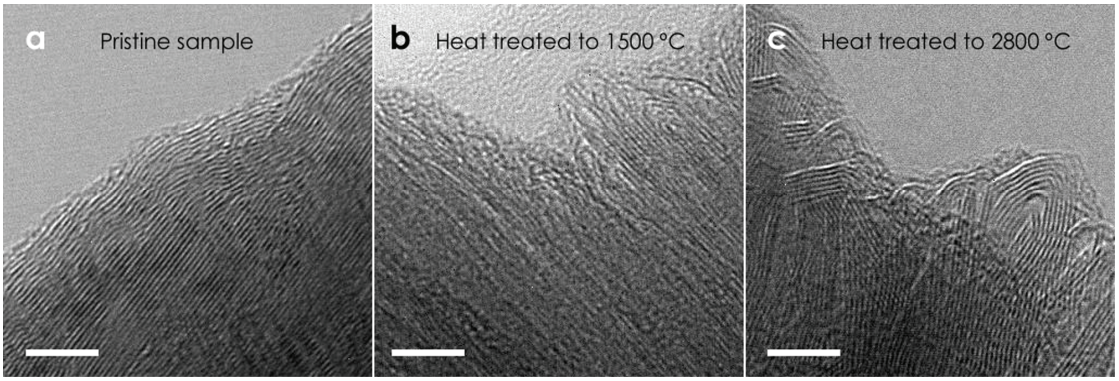

Figure 5.3 TEM micrographs of the edges of graphitic nanoribbons: a) pristine sample, b) sample heat treated at 1500 ºC and c) sample heat treated at 2800 ºC for 30 minutes in a graphite furnace under an inert Ar atmosphere (9). The scale bars for the three images correspond to 5 nm. [96]

ribbons, and these chemical groups thereby passivate these edges. Other atoms present in the synthesis, such as S or Fe, were not detected in our measurements due to their low concentration, which was lower than the detection limits of the different techniques used in our studies (EDX, EELS, XPS). Nevertheless, it is possible that some low concentrations of hetero-atoms are incorporated into the sp^2 hybridized lattice, along with O and H.

5.2 Folded edge formation by furnace heating

The as-produced nanoribbon material was annealed at various temperatures between 1500 ºC and 2800 ºC using a graphite furnace under an inert Ar atmosphere for 30 minutes (9). The structural changes promoted by furnace heating of the samples were monitored by TEM, as shown in Fig. 3 by comparing the images for the pristine material (Fig. 5.3(a)) and for the samples annealed at 1500 ºC (Fig. 5.3(b)) and at 2800 ºC (Fig. 5.3(c)) within the graphite furnace.

For the pristine (as prepared) sample (3), we can observe relatively straight lattice fringes and open end planes at the edges of the un-annealed nanoribbon. With a heat treatment temperature of 1500 ºC, we can notice some changes in the structure, including a straightening of the lattice fringes, reflecting a restructuring process, which also includes single loop formation at

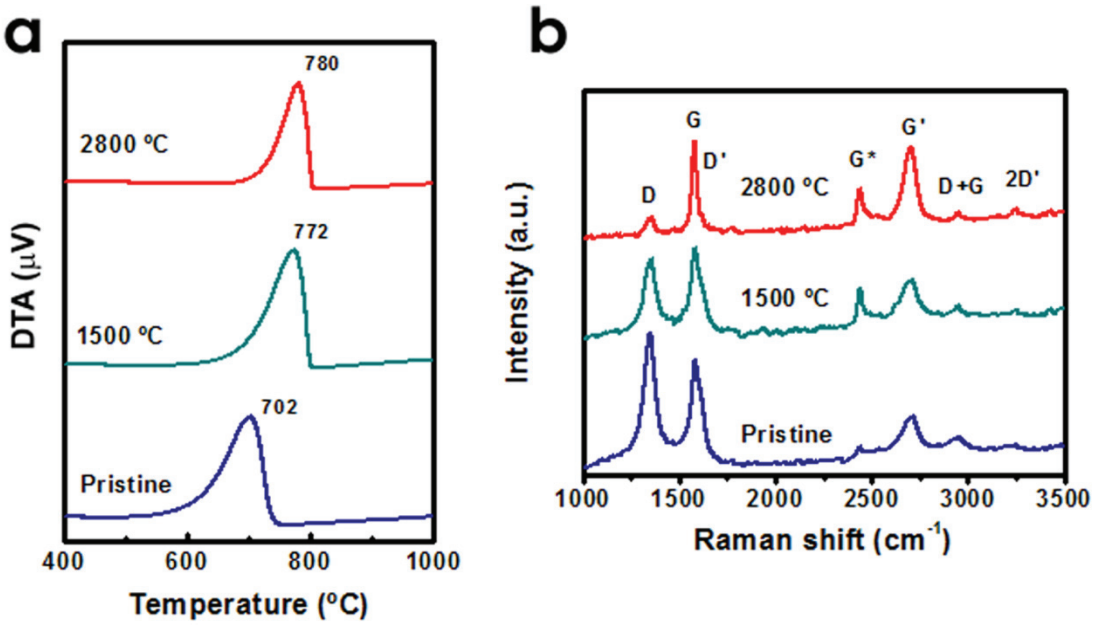

Figure 5.4 a) Data on graphitic ribbons for the first derivative with respect to temperature of the weight loss curves (9) and b) Raman spectra taken at E_{laser} = 2.33 eV for the pristine sample and the samples heat treated at 1500 ºC and 2800 ºC (adapted from Ref. [93]).

the edges. In contrast, for the pristine sample only open-ended planes were observed. At the highest heat treatment temperature (2800 ºC), we observe in Fig. 5.3(c) multiple loops with highly faceted morphologies, along with a highly crystallized material away from the edges of the sample.

Further characterization of the heat treated (HT) graphitic nanoribbons [93] is shown in Fig. 5.4. Thermogravimetric analysis (TGA; Fig. 5.4(a)) revealed the decomposition temperatures T_d in air of the three investigated samples (pristine, HT at 1500 ºC and HT at 2800ºC), with values of T_d being 702 ºC, 772 ºC and 780 ºC, respectively. We can conclude that the annealing treatment induces structural changes that turn the sample into a less reactive material, since the decomposition temperature for the pristine material was increased by ~70 ºC through heat treatment at 1500 ºC. Only an increase of 8 ºC in T_d was found by further increase of the heat treatment (HT) process to 2800 ºC. These changes in the structure were also confirmed by Raman spectroscopy (see Fig. 5.4(b)). For the pristine sample we note a very high intensity of the D-band, even higher than for the G-band, indicating that the hexagonal symmetry of the carbon lattice is

broken due to the presence of structural defects; as the annealing temperature is increased to 1500 ºC, we notice a considerable decrease in the D-band intensity. This is in good agreement with both the TEM and the TGA results, indicating a transformation into a more crystalline material with annealing at 1500 ºC. The similarity of T_d for both the HT-1500 ºC and HT-2800 ºC samples suggests that little change in chemical reactivity occurs with further heat treatment above 1500 ºC. The HT-2800 ºC sample, however, showed a residual Raman D-band with a low intensity because energetically stable loops formed in the end planes of nanoribbons prevent the development of 3D stacking, which we attribute to a high degree of graphitization in the material as a whole. However, the loops formed by heat treatment and the ripples that were preserved within the ribbons after heat treatment, are both types of symmetry-breaking structures that result in a residual D-band intensity in H-2800 ºC sample.

5.3 Folded edge formation by Joule heating

Resistive Joule heating experiments on the graphitic nanoribbons were carried out using an integrated STM-TEM system as previously described in Chapter 4, section 4.1.1. The as-prepared ribbon sample is placed in between the STM tip and the sample holder, and a controlled bias voltage is applied across the ribbon.

Figures 5.5 (a)-(d) depicts TEM images of the nanoribbon edges after Joule heating. As we can see from these images, in the interior region of the ribbon material, the originally wavy fringes (see Fig. 5.2(c) and Fig. 5.3(a)) are developed into close packed straight lines, indicating an increased crystallinity of the graphitic nanoribbon material, which is consistent with our observation of furnace heated samples at 1500 ºC and 2800 ºC (Figs. 5.3(b) and 5.3(c)) [93]. Along the edges of the ribbon material, the open ends (Fig. 5.3(a)) disappear, thus forming loops of different shapes (Figs. 5.5(a)-(d)). The loops formed near the electrodes (Fig. 5.5(a)) reveal a larger degree of curvature with a minimum of 2-3 layers contained within the loops, a result which is consistent with the furnace-heated samples in the temperature range between 2000 ºC - 2500 ºC. The

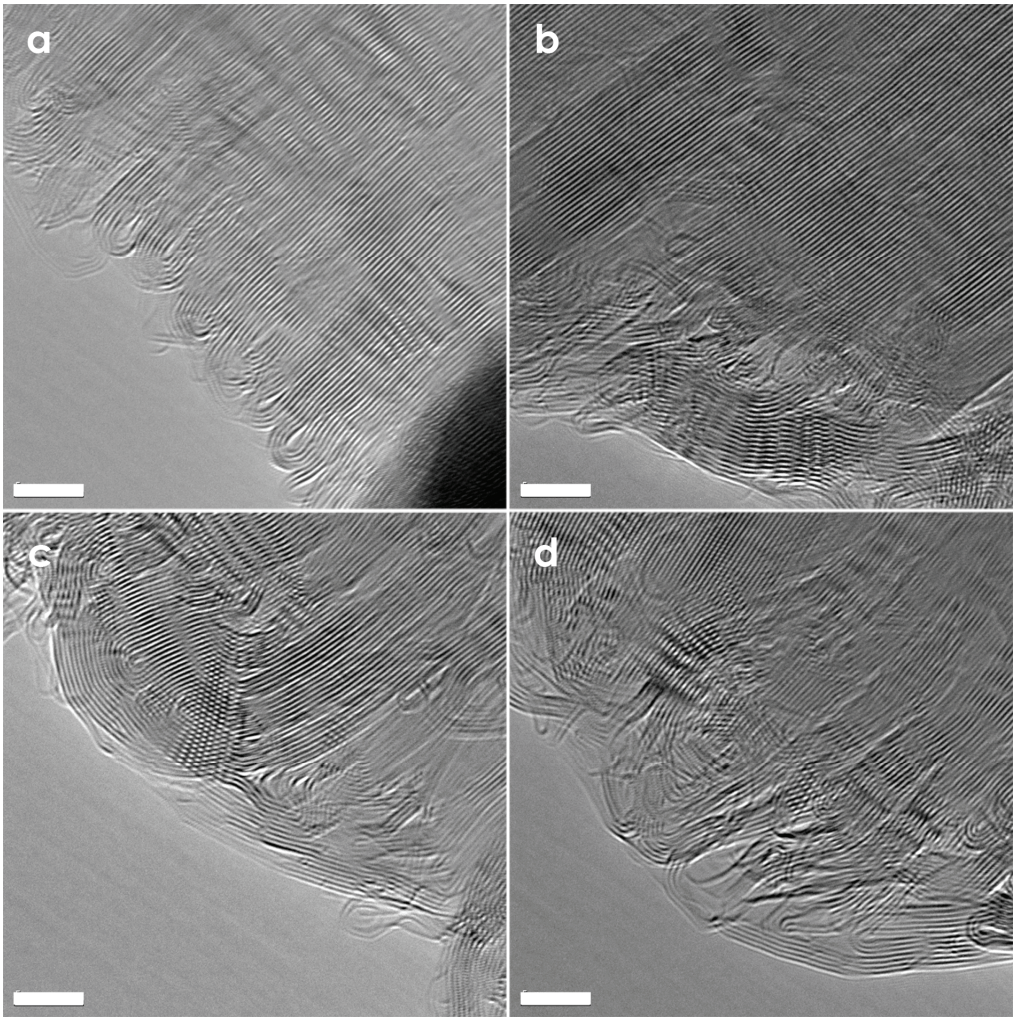

Figure 5.5 TEM images showing loop formation by Joule heating: a) near the electrode, b) and c) further away from the electrodes than in (a), and d) near the central region of the suspended graphitic nanoribbon material. (Scale bar is 5 nm)

loops formed further away from the electrodes (Figs. 5.5(b)-(c)) display a smaller curvature with more than 10 layers contained on average within a single loop. Finally, the loops formed near the central region of the ribbon material (Fig. 5.5(d)) reveal even larger loops and these even contain some facets (graphitization effect). Compared with the furnace heat treatment at 2800 ºC (Fig. 5.3(c)) where multiple loops (~6 layers) are formed, Joule heating (Figs. 5.5(c)-(d)) results in loop formation with more layers (>10 layers), which might indicate that a higher local temperature is reached. Furthermore, the annealing

process for Joule heating takes a shorter time (~15 min) compared to 30 min in the furnace heating experiment.

The effect of loop formation by Joule heating is primarily attributed to the high temperature achieved by resistive Joule heating. We attribute the different shapes of the loops, that is, smaller loops (double or triple) near the electrodes (Fig. 5.5(a)), and larger multiple loops and faceted formations near the central region of the ribbon (Fig. 5.5(d)), to the larger temperature difference across the ribbon. Here the two electrodes serve as the heat sinks, and good thermal conductivity is achieved near the electrodes, so the temperature near the electrodes is much lower than that in the central region of the ribbon. This result is also consistent with the furnace heating experiments, which showed that different shapes of loops are formed at different annealing temperatures (Figs. 5.3(a)-(c)).

5.4. Mechanism for open and folded edge formation

We have demonstrated that loop formation through the coalescence of bare edges on nearby graphene sheets can be successfully achieved by both furnace annealing and Joule heating. We have also noted that high temperatures play the main role in this process. As explained by Campos-Delgado et al. [93], the loop formation is the result of a restructuring process taking place in the nanoribbons when subjected to high temperatures. As the annealing temperature is increased to 1500 ºC, the experiments carried out within the furnace reveal that the structure becomes much more crystalline; the lattice fringes seen in the TEM images corresponding to graphitic planes straighten up as the annealing temperature is increased. Above a temperature of 1500 ºC, the edges of the ribbons reconstruct, and single loops start appearing. It is noteworthy that the diameter of these loops is larger than the sheet-to-sheet separation, sketched in Fig. 9 and observed experimentally in Fig. 5.3(b).

Annealing temperatures around 2000 ºC result in double loop formation (see Fig. 5.6), as reported previously in references [93] and [92]. At higher

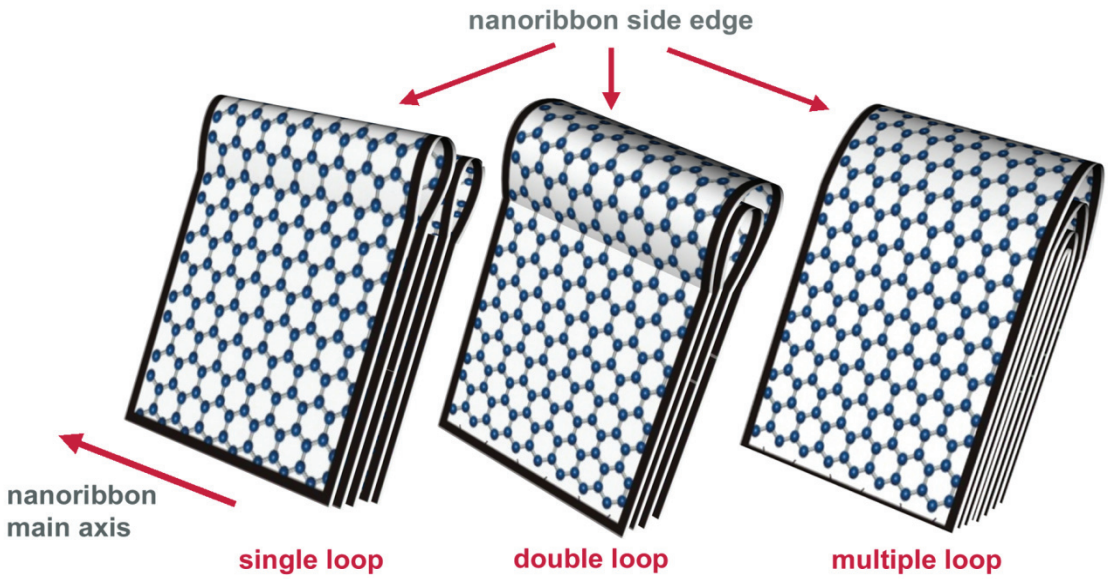

Figure 5.6 Schematic model of single, double and multiple loops formed in the graphitic nanoribbons, where the direction along the length of the nanoribbon is considered as the main axis (see also Figs. 5.2b and 5.2d). [96]

temperatures, above 2500 ºC, multiple loops form (see Fig. 5.6) and we also observed more faceted graphitic features.

For the Joule heated nanoribbons, a similar high temperature effect is achieved due to resistive Joule heating. However, a higher degree of crystallinity is achieved with increased annealing by Joule heating, and loops are created in the graphitic nanoribbon material in order to passivate the carbon atoms at the edges. However, when compared to the furnace heat treatment results, Joule heating could reach higher local temperatures (>2800 ºC) in the material, which induces enhanced crystallinity by the formation of larger multi-layered loop structures. It is also important to emphasize that the loop formation and the lattice restructuring process, could be achieved in a relatively short annealing time by Joule heating.

A similar observation was made by the Iijima group in [92] where an HOPG sample is heat treated in a furnace for several hours at 2000 ºC. In this case, TEM micrographs of the heat treated sample clearly show loop formation at the edges. Another method for loop formation, other than furnace heat treatment, is by direct resistive Joule heating across pristine graphitic nanoribbons inside a

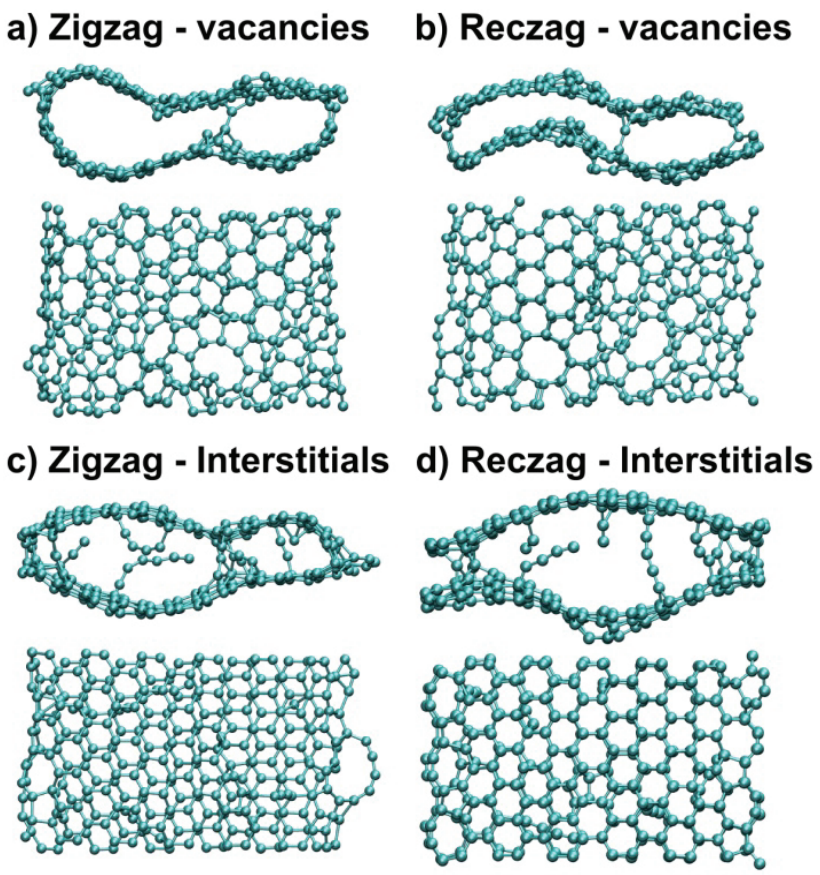

Figure 5.7 Molecular models showing the final configurations for graphene nanoribbons with vacancy (a),(c) and interstitial defects (b),(d). Zigzag ribbons create loops with both vacancies (a) and interstitials (c), while the reconstructed zigzag (*reczag)* edges do not show this behavior and rather show increased structural order. Interstitials lead to the formation of monoatomic carbon chains in both zigzag and *reczag* edges, due to the low reactivity of a graphene surface. (Images are adapted from Ref. [97]).

TEM, as mentioned in section 5.3. It is found that resistive Joule heating without prior electron beam irradiation damage induces effective loop formation in a way that is very similar to that of furnace heat treated samples.

The key difference between open edges and loop formation is the significant role played by electron beam irradiation when applied before and during in-situ Joule heating. Irradiation indeed enables edge modification and sharp open edge formation in CVD-grown graphitic nanoribbons. Recent theoretical work by Cruz-Silva et al. [97] provided an atomistic analysis to highlight the reasons why loops are formed by Joule heating alone, while

adjacent layers do not coalesce when Joule heating is applied after high energy electron irradiation. This theoretical work based on large-scale quantum molecular dynamics calculations indicates that the presence of both vacancies and interstitials (so-called "Frenkel pairs") are essential for keeping graphene layers parallel to one another and for preventing adjacent edges from coalescing (loop formation). Electron beam irradiation, based on previous reports [45,98,99], is likely to provide the driving force for inducing vacancies and interstitials in graphitic nanoribbons. On one hand, the introduction of vacancies increases the surface reactivity and interlayer interaction far away from the edges. On the other hand, the interstitials provide effective feedstock to ensure interlayer cross-link creation which keeps the layers parallel and prevents loop formation (see Fig. 5.7). Quantum transport calculations further confirm that interlayer cross-linking increases the backscattering of electrons and promotes interlayer transport [97]. Therefore the cross-linking sites are key for both Joule heating and defect annealing, and such sites are susceptible to being healed during the joule heating process.

5.5. Summary

In this chapter we discussed the structural transformations occurring in a novel type of high surface area graphitic nanoribbon material grown by a CVD method, which is especially well suited for studying edge reconstruction [28] and for studying loop formation. In this chapter we investigated loop formation in these graphitic nanoribbons, under both furnace heating and Joule heating; these provide complementary ways of heating the samples. In both cases, the pristine open edges of the nanoribbons are shown to develop into stable closed loops, and the shapes and sizes of the loops could be modified and controlled by varying the annealing temperature and other annealing conditions. The shapes of the loops under Joule heating provide evidence for edge evolution into multi loop structures above 2800 ºC. Theoretical calculations show that electron-beam irradiation in the TEM prior to Joule heating may induce vacancies and

interstitial defects which could prevent loop formation, while direct Joule heating would results in loop formation. Comparing furnace heating and Joule heating we can conclude that Joule heating could be an efficient way for restructuring pre-graphitic structures into highly ordered graphitic material, in which stable loops could be formed after an edge reconstruction process of the bare edges of the laminated carbon material has taken place. We envisage that the chemistry and reactivity of these loops will be different when compared on the basis of the precursor materials used in the sample synthesis. Therefore, the interaction of different molecules with these loop structures should now be studied from both an the experimental and theoretical standpoint, so that these looped materials could perhaps be used for sensor applications.

Chapter 6

Temperature measurement using Pt nanoparticles

In Chapters 4 and 5, we demonstrated dramatic structural changes in graphitic nanoribbons using *in-situ* Joule heating. A question which arises naturally is what is the temperature of the nanoribbon during the Joule heating experiment. In order to estimate the temperature inside the TEM, we used Pt nanoparticles to calibrate the temperatures by monitoring Pt nanoparticle melting during Joule heating. We can calculate the melting point of nanoparticles from simple thermodynamics consideration. The nanoparticle melting point is usually much lower than that for their bulk counterparts [100]. However, it is not well understood if the nanoparticles would reach the melting temperature before sublimating or before coalescing into clusters. This chapter aims at understanding this behavior from both experimental and theoretical points of view.

Pt nanoparticles have been widely used in energy applications. For example, they are used as nano-catalysts for lowering the energy barriers for water splitting or CO oxidation. Although there have been theoretical studies on Pt nanoparticle melting, sublimation and sintering, not much experimental work has been reported on Pt nanoparticle melting and sublimation. With the *in-situ* TEM, we are able to probe the structural changes in these Pt nanoparticles at elevated temperatures and in real time. Our work shows that for Pt nanoparticles with small diameters, sublimation and sintering may occur before the nanoparticles reach their melting temperatures. The sublimation or sintering rate strongly depends on the particle size, and the temperature. The substrate and nanoparticle concentration may also play an important role.

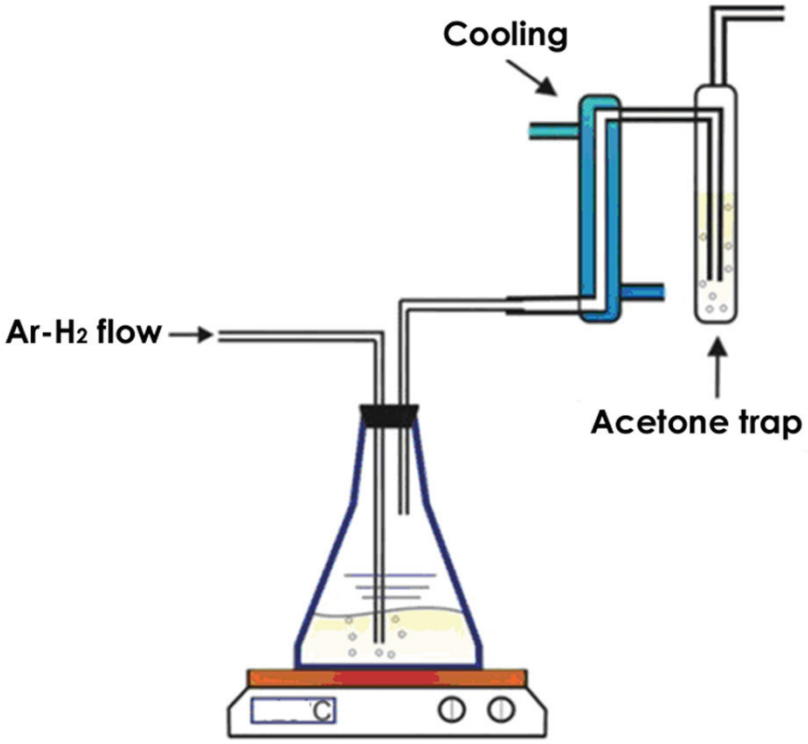

Figure 6.1 Diagram of the set up used in the process of anchoring Pt nanoparticles to the graphitic nanoribbon material. [96]

This chapter will start with an introduction to the synthesis method for depositing Pt nanoparticles on graphitic nanoribbon substrates, followed by experimental investigations of Pt nanoparticle structural behaviors at high temperatures. Theoretical calculations are adopted to understand the observed phenomena.

6.1 Materials synthesis

Pt nanoparticles were deposited chemically on the as-prepared graphitic nanoribbon surface (as described in Chapter 5, section 5.1). The Pt anchoring process consisted of sonicating for 15 minutes a mixture of graphitic nanoribbons (10 mg), plus 10 ml of N,N-dimethylformamide (Sigma-Aldrich®, 99%), and (1,5-Cyclooctadiene) dimethylplatinum (II) (Aldrich®, 97%) as a platinum source and polyvinylpyrrolidone (Sigma-Aldrich®, average mol wt 10,000) as a passivating agent. After sonication, the suspension was maintained

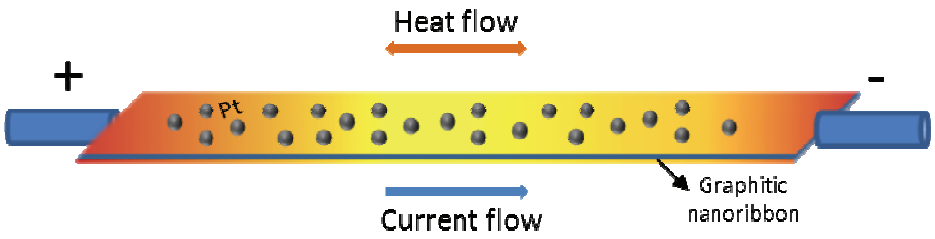

Figure 6.2 A schematic of the Joule heating experimental setup for Pt anchored graphitic nanoribbons.

under an Ar-H_2 (5% H_2) atmosphere to increase the reduction rate (see Figure 6.1), and the suspension was subsequently placed in a glycerin bath at 110 ºC for 40 minutes.

Next, the suspension was allowed to cool down to room temperature and the composite material (graphitic nanoribbons with Pt particles) was recovered by filtration. These graphitic nanoribbons exhibited platinum nanoparticles (with an average size of ~6 nm) anchored to their surface. Finally a thermal treatment was carried out at 350 ºC under an Ar atmosphere for 15 minutes in order to eliminate any residues of organic material that could remain on the surface of the composite material.

6.2 Sublimation and sintering of Pt nanoparticles at high temperatures

The modified nanoribbon material was mounted onto the TEM-STM set-up (as described in Chapter 4, section 4.1). A bias voltage is applied across the ribbon length to induce resistive Joule heating, as sketched in Figure 6.2. The electrodes also serve as heat sinks, and heat is flowing from the center region of the ribbon towards the electrodes. As we increased the applied voltage, the Pt nanoparticles near the central region of the ribbon started to merge with small neighboring Pt nanoparticles (some particles finally reached a diameter of 13 nm). Subsequently, and starting from the central region, the Pt nanoparticles disappeared, resulting in a clean surface (devoid of Pt nanoparticles) near the center of the ribbon sample (Fig. 6.3(b)). When a higher voltage is applied, additional Pt

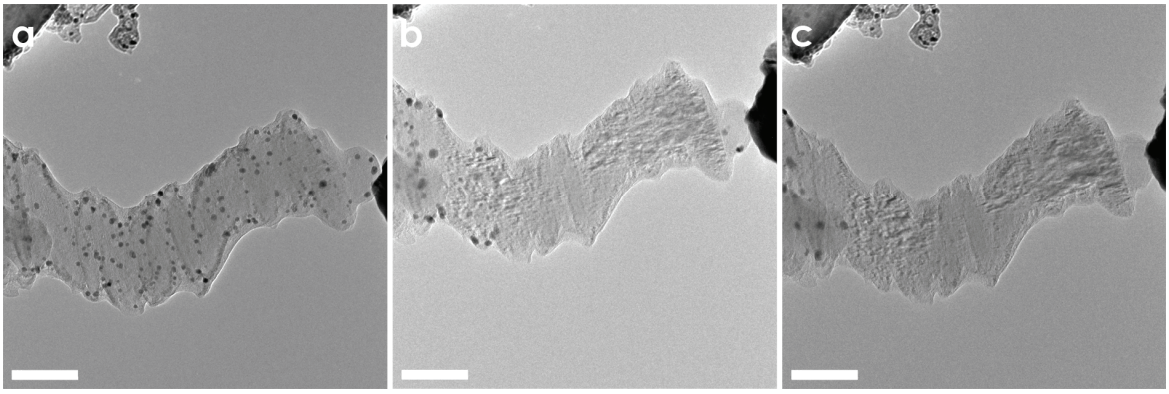

Figure 6.3 A sequence of TEM images showing Pt nanoparticles on the ribbon surface (a) before Joule heating, (b) after Joule heating for 11 minutes under a constant bias of ~2V, and (c) after Joule heating for 15 minutes under a constant bias of ~2V. Here we see that the Pt particles melt and merge into bigger clusters (b), and start to evaporate from the central region of the ribbon (b), and eventually evaporate across almost the entire ribbon sample (c). (The scale bars are all 100 nm.)

nanoparticles disappeared and eventually almost the entire ribbon is free of Pt nanoparticles (Fig. 6.3(c)).

The evolution of the Pt nanoparticle size distribution at increased Joule heating times is plotted in Figure 6.4. From the TEM images and the histograms, we can see the small nanoparticles disappear immediately upon heating, and the big nanoparticles first grow bigger, and eventually they shrink and disappear as well, likely due to a temperature increase. The combined effect of small particles disappearing and big particles growing results in a right-shifting of the histograms, indicating that the average size of the nanoparticles is increased. The transition size at which particles would either disappear or grow is at about 6nm. The total number of particles also decreases dramatically (by ~ 80%) upon Joule heating, as plotted in Figure 6.5.

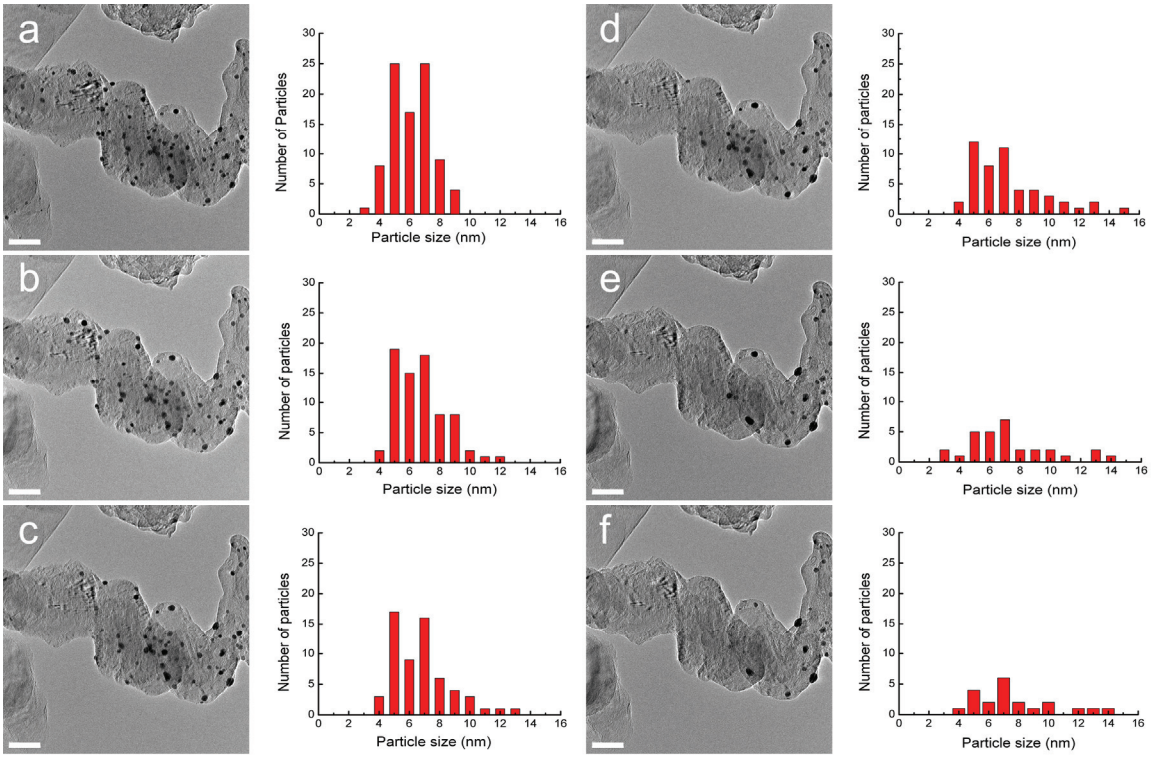

Figure 6.4 The evolution of Pt nanoparticle size distribution at the same region of a graphitic nanoribbon surface during *in-situ* Joule heating. (a) – (f) are series of TEM images at t = 0s, 74s, 132s, 154s, 208s, and 222s heating times, respectively. And the histogram of the particle size distribution is plotted next to each TEM image. The two electrodes are located on the left and right sides of the ribbon, which are not shown here. The scale bar for each image is 50 nm.

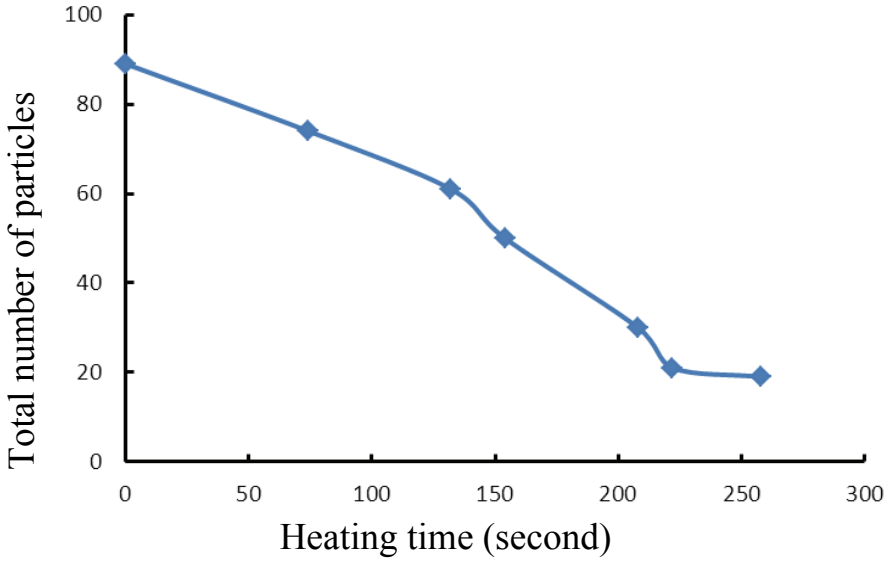

Figure 6.5 The total number of particles as a function of heating time showing a dramatic decrease in the number of particles.

6.3 The competing processes of melting, sublimation, and sintering

Bulk Pt has a melting point of 2041.4K. The melting point of the Pt nanoparticles will be suppressed compared to their bulk counterpart due to size effects [101]. The melting temperature of Pt nanoparticles could be approximated using the following equation:

$$T_m \sim T_m^o \left({}^{E_{b(n)}}/_{E_b^o} \right) \quad (6.1)$$

where T_m^0 and E_b^0 are the bulk melting point and the bulk cohesive energy. $E_{b(n)}$ is the cohesive energy for a nanoparticle containing n atoms, which can be calculated using [102]:

$$E_{b(n)} = E_b^o \left[1 - {}^{1}/_{n} \right] \quad (6.2)$$

The melting point of Pt nanoparticles versus particle size can thus be calculated, as shown in Figure 6.6. The melting point is strongly suppressed at small diameters, and reaches only half of the bulk value at a diameter of about 1 nm.

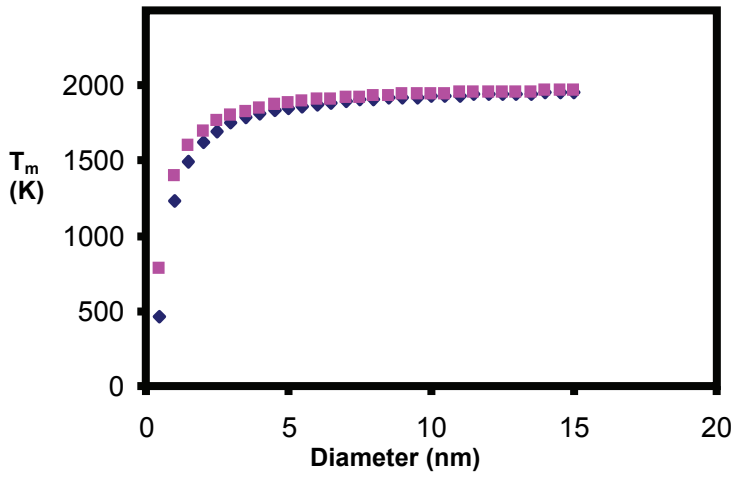

Figure 6.6 Pt nanoparticle melting points at different nanoparticle diameters calculated for hemispherical (blue dots) and spherical nanoparticles (pink dots).

However, melting is not the only process that nanoparticles can be undergoing at high temperatures. It has been calculated that in Au nanoparticles, sintering and sublimation also become significant for small nanoparticles. The vapor pressure P, sintering rates dn/dt, and rate constants for sintering and

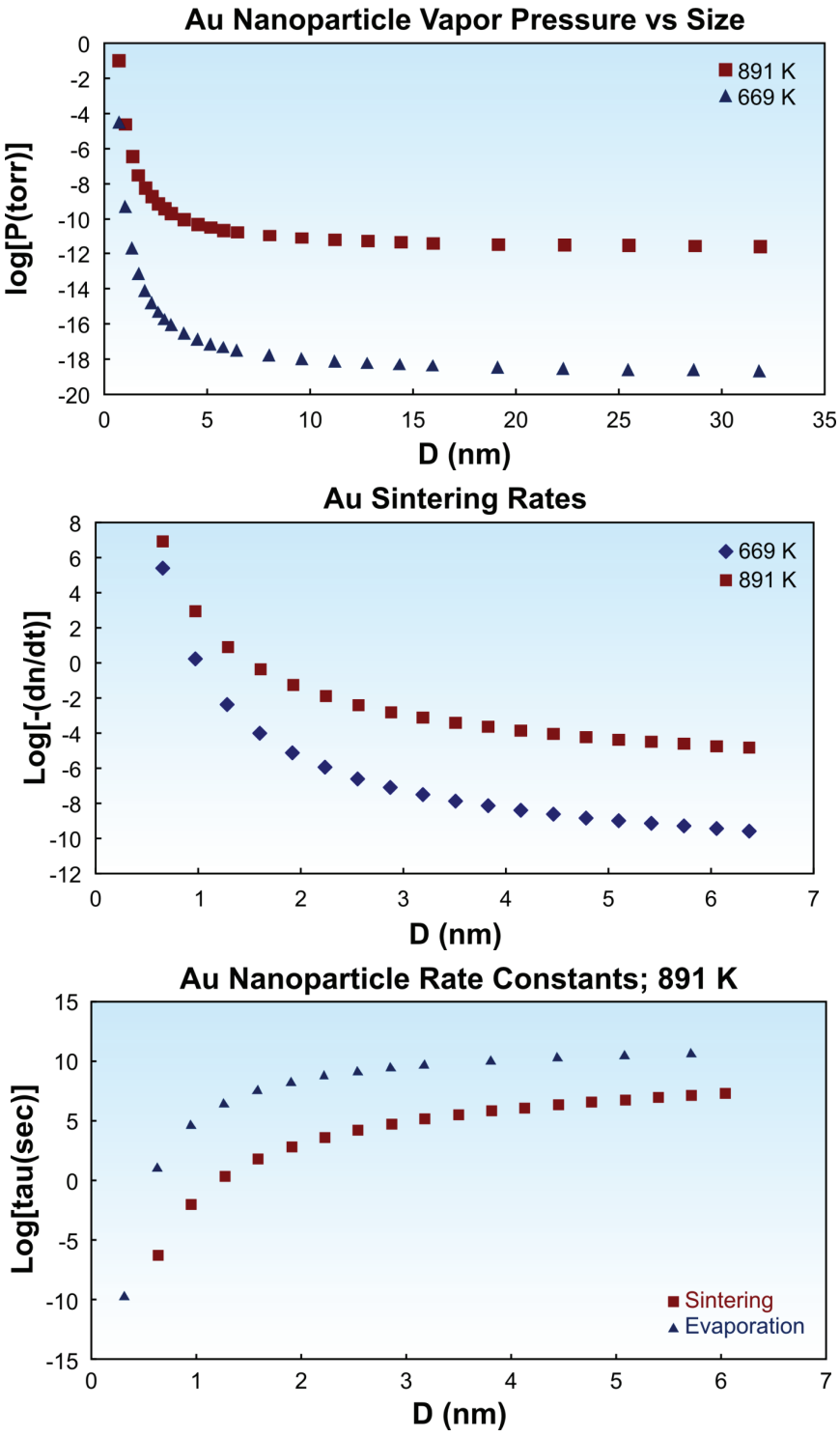

Figure 6.7 Calculated Au nanoparticle vapor pressure P, sintering rates dn/dt and rate constants (for sintering and evaporation) versus particle size at 669K and 891K.

evaporation have been calculated for Au nanoparticles with different sizes and at different temperatures (Figure 6.7). The vapor pressure (which measures the evaporation rate of the nanoparticles) and the sintering rates both increase dramatically as the particle size becomes smaller, and as the temperature is increased. From the comparison of the rate constants we can also see that the sintering process becomes more dominant at high temperatures. Pt nanoparticles have similar physical properties to Au nanoparticles, and should result in similar behaviors. A more detailed calculation for Pt nanoparticle vapor pressure and sintering rate has been undertaken to explain the experiments, and the results are expected to be available for publication soon.

6.4 Summary

In summary, our results indicate that other kinetic phenomena, such as sublimation and particularly sintering, will interfere with the measurement of nanoparticle melting temperatures. Nanoparticles could sublimate or coalesce before they reach their melting temperatures. The sublimation and sintering will depend upon the rate of heating, the experimental set up such as the diffusivity, surface density, etc. In order to get an accurate temperature measurement using Pt nanoparticles as a temperature monitor, other kinetic processes such as sublimation and sintering have to be inhibited by methods such as enclosing the nanoparticles in a porous structure which limits the nanoparticle diffusion [103]. On the other hand, for Pt nanoparticle applications, it is also important to be aware of the sublimation and sintering processes which occur at high temperatures, since the use of such processes may affect the desirable performance of the nanomaterials after processing.

In order to further probe the properties of these nanoparticles, high resolution TEM images need to be taken and compared at different times during heating. HRTEM will provide the information of the nanoparticle crystallinity before and after heating, so the melting process could be accurately monitored. The effect of the substrate, the nanoparticle concentration, and the heating rate

on the sintering and evaporation rate should also be studied by further characterizations.

Chapter 7

STM and STS studies of CVD grown graphene and graphene nanoribbons

7.1 Introduction

In Chapters 4 and 5 we have used *in-situ* TEM to characterize the structures of graphitic nanoribbons and their modified edges. The electronic structures, on the other hand, cannot be studied using TEM. Scanning tunneling microscopy (STM) and scanning tunneling spectroscopy (STS) are advantageous for studying the surface morphology and electronic structures of materials, respectively. In this chapter, I will present the work on the studies of CVD grown graphene and graphene nanoribbons using these complementary techniques.

In the recent couple of years, there has been a growing research interest on the STM and STS studies of graphene, motivated by the unique physical and electronic properties predicted in graphene [10]. Zhang *et al.* first reported giant phonon induced conductance in gate tunable graphene from a HOPG-derived sample placed on a SiO_2 substrate in 2008 [104]. Later on, Li *et al.* observed that twisted graphene layers give rise to van Hove singularities that can be measured in STS [105]. Levy *et al.* recently discovered that the strain in graphene nanobubbles could induce pseudo-magnetic fields greater than 300 Tesla [106].

The electronic properties of graphene nanoribbon edges have also intrigued experimental scientists for a long time [107], since magnetic properties and edge states are predicted at the edges. However, it is very challenging to study the electronic properties at graphene edges with STM and STS for two reasons. First of all, STM and STS measurements are very sensitive to surface contaminations, and an ultra clean surface is usually required to obtain accurate

measurements. However, graphene edges with dangling bonds are chemically reactive, and tend to pick up chemical groups during a graphene wet transfer process. Secondly, graphene nanoribbons with smooth edges are not easily produced. And edge disorder will strongly interfere with the study of edge states.

In this work, we directly synthesized graphene nanoribbons on large sheet graphene using a CVD method, and studied the morphologic and electronic properties on both large sheet graphene and graphene nanoribbons. These materials exhibit a highly crystalline structure, comparable to the HOPG-derived graphene. They also have ultra clean surfaces and edges, allowing us to study the interlayer twisting and the edge states in graphene nanoribbons.

7.2 Synthesis of graphene nanoribbons on a graphene background sample

Graphene materials are synthesized under atmosphere pressure CVD conditions using gas mixtures composed of hydrogen, argon and methane. Copper foils (3" X 1") are placed in a one inch quartz tube furnace and are heated to 1000 °C under a mixture of hydrogen and argon gas flow (H_2:Ar = 50:450 (sccm)). Subsequently, methane gas (2 sccm) is introduced in the furnace after the temperature stabilizes and the syntheses are performed for 20-30 minutes. The samples are finally cooled to room temperature under hydrogen, methane and argon gas flow [108].

The synthesized materials are then transferred onto SiO_2 substrates and TEM grids using a wet etching process, and characterized using optical microscopy and TEM, respectively. Unlike single layer graphene samples grown by conventional low pressure CVD on copper foils (as shown in Figure 7.1a for comparison), these materials exhibit a slightly darker color in the optical microscope with localized regions of even darker colors, indicating multi-layered graphene flakes sitting on a few-layer graphene sheet (Figure 7.1b).

A TEM study is also performed to determine the material quality and to confirm the number of layers using a JEOL 2010F TEM, operating at 200 kV.

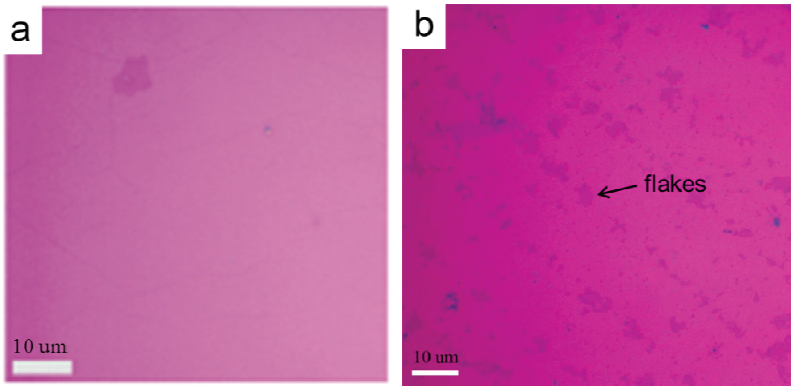

Figure 7.1 Optical images of CVD grown graphene transferred onto SiO_2 substrates. (a) Single layer graphene grown using a low pressure CVD method. (b) Multilayer graphene with flakes grown using an atmosphere pressure CVD method. [108]

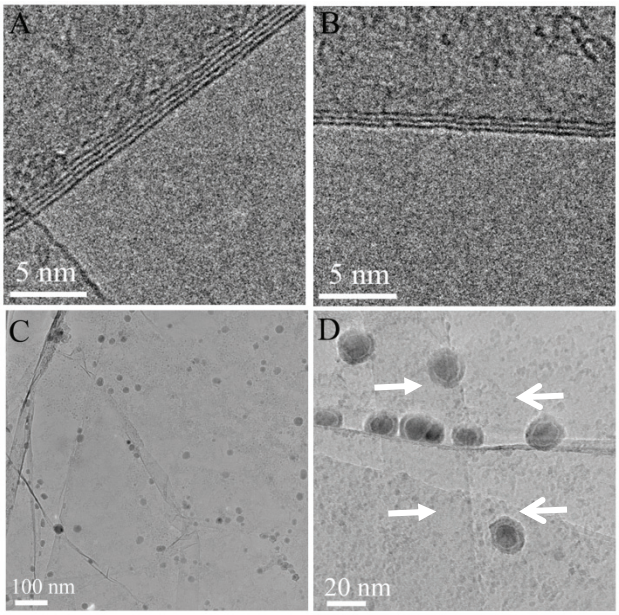

Figure 7.2 TEM characterizations of CVD grown graphene flakes and ribbons on a large sheet few-layer graphene sample. (A, B) High resolution TEM images of graphene synthesized using Cu foils. (C) Contaminant nanoparticles (from the Cu etchant) decorating graphene edges. (D) Graphene nanostrips and nanoribbons (along the arrows). [108]

Representative high-resolution TEM images of the graphene samples are shown in Figure 7.2A-B. These images confirm the presence of multilayer domains in these graphene samples. Additionally, the number of layers in these multilayer domains varies from 2 to 5 layers. When imaging over large areas, we can clearly see nanoparticle residues attached to the edges of graphene domains. These

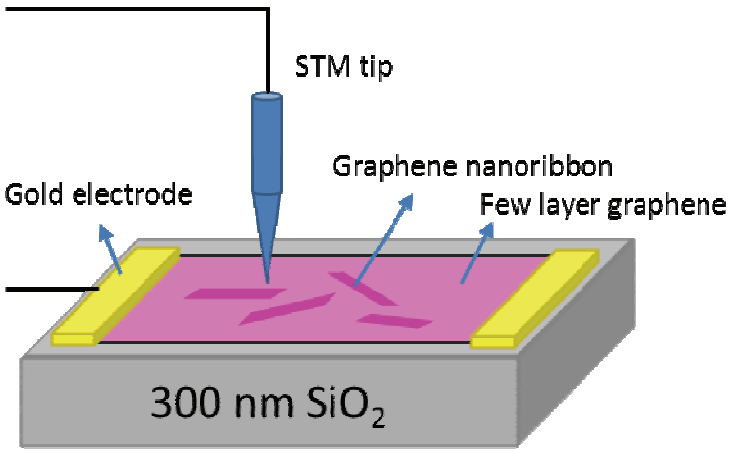

Figure 7.3 A schematic of the STM and STS measurement setup in a ultrahigh vacuum chamber. One gold electrode is grounded.

nanoparticles are iron/iron oxide core shell nanoparticles that come from the copper etchant. The attachment of the particles to the edges indicates strong interactions between the edges and the nanoparticles (Figure 7.2C), and also enable us to identify nano-sized features present in these samples, such as graphene nanoribbons and nanostrips with widths ranging from 20nm to 100nm (Figure 7.2D).

7.3 Twist and strain in few layer graphene

Few layer graphene can have advantages over single layer graphene because it has a larger current carrying capacity, and the electronic properties can be tuned by varying its inter-layer stacking (twist) and intra-layer strains. Here we use STM and STS to probe the morphologic and electronic properties in the CVD grown few layer graphene (the synthesis of which is described in section 7.2). The as-grown samples are transferred onto 300 nm SiO_2 substrates and patterned with gold electrodes, before their transfer into an ultrahigh vacuum STM setup for STM and STS measurements. A schematic of the experimental setup is shown in Figure 7.3. Large area STM scans show a rough surface of the few layer graphene on SiO_2, with a surface corrugation of about 0.6 - 1 nm. This surface corrugation can be attributed to the roughness of the SiO_2 substrate. The few layer graphene on this rough substrate will adopt the surface morphology of the

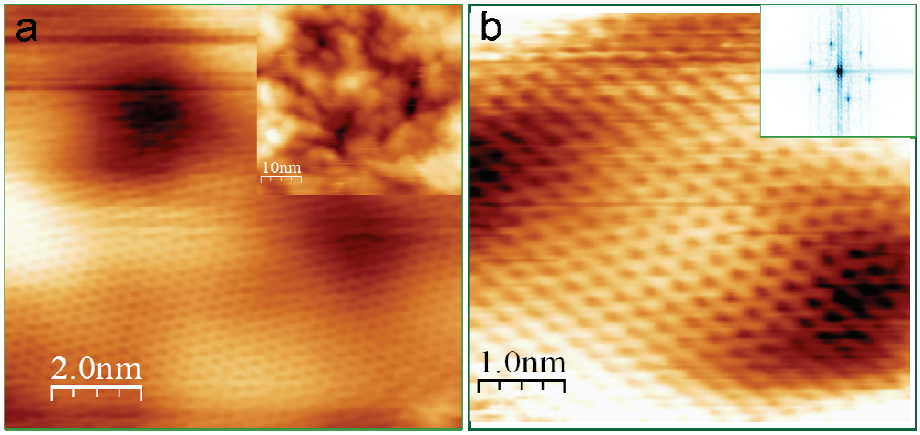

Figure 7.4 STM images of CVD grown few layer graphene on a SiO_2 substrate. (a) Atomic-resolution image shows a well-ordered triangular lattice, which indicates Bernal-stacked layers. The inset is a larger area scan (50nm×50nm) which shows the corrugated surface with the roughness ranging from 0.6 nm to 1 nm. (b) Atomic-resolution image of a 5nm×5nm area shows "hills" and "valleys" features. The inset is a Fourier transform of the image. Tunneling current is 50 pA, and sample bias voltage is 0.6 V.

substrate, exhibiting unique "hills" and "valleys" features all over the surface, as shown in Figure 7.4. This corrugated SiO_2 surface naturally induces strains in these few layer graphene samples.

CVD grown graphene usually forms a rotational stacking order (instead of the AB Bernal stacking order observed in graphite) between adjacent layers [109]. The rotation (or twist) between graphene layers is often observed in a STM image as a Moiré pattern. In a bilayer graphene with a twist angle θ, the condition for commensurate periodic structures leading to a Moiré pattern is easily derived: $\cos(\theta_i) = (3i^2 + 3i + 1/2) / (3i^2 + 3i + 1)$, with i being an integer (i=0, $\theta=60^0$ corresponds to AA stacking; and $i\rightarrow\infty$, $\theta=0^0$ corresponds to AB stacking). Figure 7.5a shows a high resolution STM image of the few layer graphene. Two sets of lattices forming a new periodicity (as marked by the two short red lines) can be found. The line profile measurement shows the separation between the adjacent atoms of two lattices varies from being well-separated to almost overlapped. This suggests the superlattice periodicity i to be about 8, giving us a twist angle $\theta = 3.89^0$. To verify this angle, we did a Fourier transform

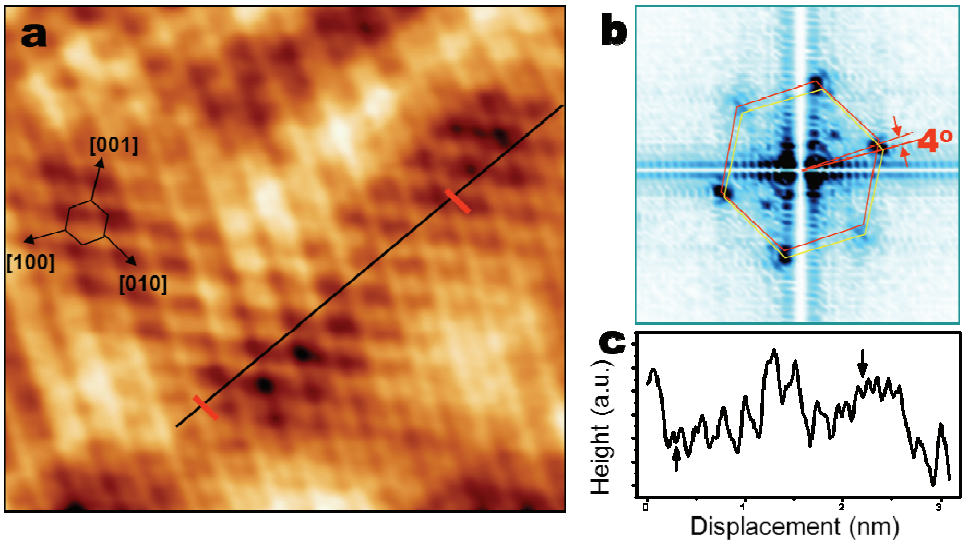

Figure 7.5 High resolution STM image of the few layer graphene. (a) Atomic resolution image shows both triangular lattices for the two twisted layers. Note the two short red lines crossing the long black line. (b) Fourier transform of the atomic-resolution image in (a) shows two sets of hexagonal dotted patterns with a 4^0 rotation. (c) The line profile is measured along the black solid line in (a). The two arrows in (c) corresponds to the positions of the two short red lines in (a), respectively.

of the atomic-resolution image, as shown in Figure 7.5b. The hexagonal reciprocal lattice splits into two sets of adjacent hexagonal dots. The angle between two reciprocal lattice vectors is measured to be 4^0, which confirms the twisting of about 4^0 between the stacked layers.

Compared to a perfect AB stacked bilayer, a graphene bilayer with a relatively small twist angle between the layers has a quite different electronic structure. Both experimental and theoretical studies have shown that the Fermi velocity in a twisted bilayer graphene can be significantly smaller than that in a single layer graphene, and Van Hove singularities (VHS) in the electron density of states can be induced by the twisting [109,110]. The tunneling differential conductance dI/dV is commonly used to probe the local density of states. The rotation-induced VHS will result in two peaks in the density of states with an energy separation of ΔE_{VHS} (as indicated in Figure 7.6b). The energy separation between the VHS points is $\Delta E_{VHS} = \pm \upsilon_F K \times 2\sin(\theta/2)$, where $K = 4\pi/3a_0$, and υ_F is the Fermi velocity which is about 10^6 ms^{-1} for an unrotated graphene layer. By

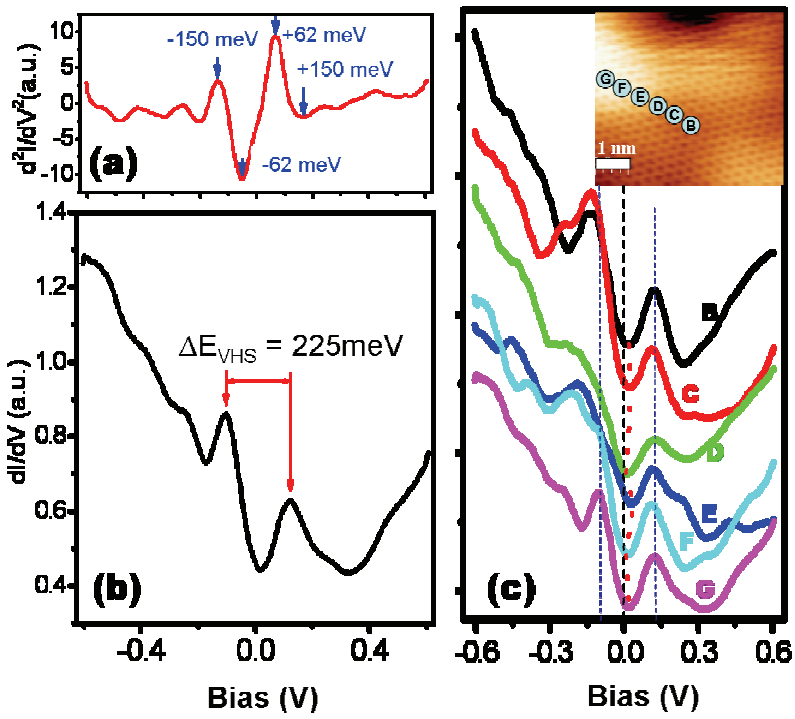

Figure 7.6 Scanning tunneling spectra of CVD grown few layer graphene. (a) Second derivative of the tunneling conductance shows antisymmetric peaks/valleys located at ±62meV and ±150meV. (b) The tunneling spectrum shows two sharp peaks around the Fermi energy with an energy separation ΔE ~ 225 meV. (c) Spatial dependence of the tunneling spectra along a line running from the top of the "hill" to the bottom, shown in the inset figure. Tunneling current is 50 pA, sample bias is 300mV, and a.c. bias modulation is 6 mV_{rms} with a frequency of 746 Hz. Although all spectra show two peaks, the energy separation between the peaks and the position of the central dip (Dirac point) slightly varies according to the position on the sample (BCDEFG).

calculating the bilayer graphene with a twist angle of 4° as measured in our system, we can get the energy separation ΔE_{VHS} to be above 0.5 V.

Figure 7.6b shows a typical dI/dV curve obtained at 25 K for the CVD grown few layer graphene. Two sharp peaks with a dip at the Fermi energy are clearly observed in this spectrum. By comparing this spectrum with the spectra shown by Guohong Li *et al.* [105], we can easily identify these two peaks as the rotation-induced VHS. The energy separation between our two peaks is ΔE_{VHS} = 225 meV, much smaller than the value we calculated from the 4° twisting angle (0.5 eV). One of the possibilities for this discrepancy is that the Fermi velocity in our system is much lower than that in a single layer graphene. That is

consistent with both theoretical prediction and experimental observations. The second derivative of the tunneling current d^2I/dV^2 is shown in Figure 7.6a. The antisymmetric peaks at ±63 meV and ±150meV are located on opposite sides of the Fermi energy, and these peaks are attributed to phonon-mediated inelastic tunneling via K-point phonons, as described in previous work [104].

Figure 7.6c shows a set of dI/dV spectra obtained at different positions (as marked) along a line from the top of the "hill" to the bottom. All the spectra show similar features with two peaks, except that the energy separation of the peaks and the position of the dip slightly change with regard to the spatial locations.

The energy separation between two peaks varies from 225 meV to 245 meV, which indicates the interlayer coupling slightly changes at different locations. Since graphene is only one atom thick, it is highly amenable to strains, which also provides the possibility of tuning the electronic properties in graphene by strain. If a strain varies smoothly on the scale of interatomic distances, it does not break the sublattice symmetry but rather deforms the Brillouin zone in such a way that the Dirac cones which are located at K and K' points shift in opposite directions [111]. There have been several reports on graphene under uniaxial deformation in recently years. The dips in the spectra, reflecting the positions of the Dirac points, all shift slightly towards the positive bias positions, which demonstrates the fact that the graphene film is locally deformed under a strain. The energy shift of the Dirac points reaches a maximum value of about 35 meV in spectrum E.

7.4 Graphene nanoribbons and edge folding

Graphene nanoribbons, which are quasi one dimensional structures of graphene, are predicted to exhibit a wide range of behaviors such as a tunable energy gap and the presence of unique one-dimensional edge states with unusual magnetic properties [18]. The energy gap and the edge states are determined by the edge chirality and the width of the ribbon. Most experimental works on graphene nanoribbons reported so far are about their electrical conductivities, while not

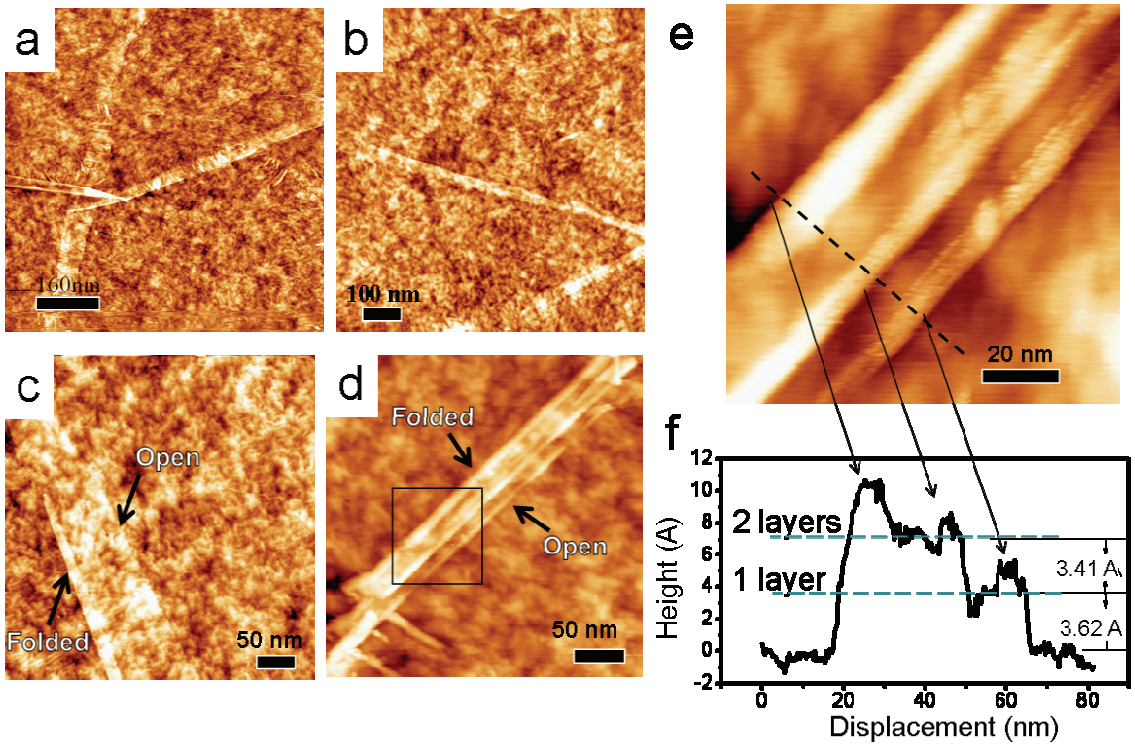

Figure 7.7 STM images and line scan of graphene nanoribbons on few layer graphene. (a-b) Large area scans show many ribbons with widths ranging from 20 nm to about 100 nm. (c-d) Small area scans show the ribbons typically have one edge open and the other edge folded. (e) is a zoom-in image of the ribbon shown in (d) (marked with a balck box). (f) is the line scan across the ribbon width showin in (e), which confirms the open and folded edge structure.

much work has so far been done on studying the electronic structures at the edges, due to the experimental challenges as mentioned above in section 7.1. We have found in using TEM characterization that graphene nanoribbons on few layers of graphene can be directly grown using our atmosphere pressure CVD method (see section 7.2). These nanoribbons did not go through lithographic cutting, so that clean and relatively smooth edges can be expected which are suitable for STM and STS measurements; therefore their local morphologic and electronic edge properties can be investigated.

The graphene nanoribbons on few layer graphene are transferred onto a SiO_2 substrate and measured in an ultrahigh vacuum STM chamber (see Figure 7.7). By taking large area STM scans, many ribbons in different orientations are found, as shown in Figures 7.7a and 7.7b. The roughness observed in the images

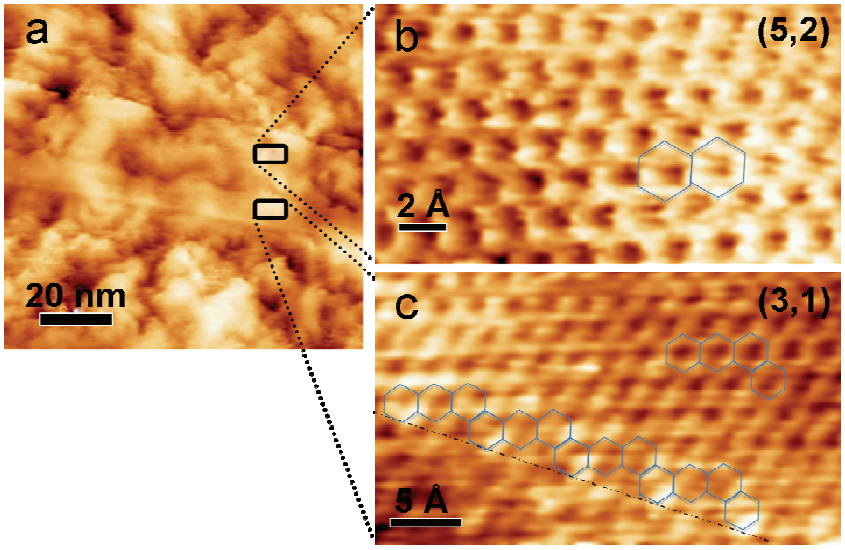

Figure 7.8 Atomic resolution images of a folded graphene nanoribbon. (a) An STM image of a folded graphene nanoribbon with one side open and the other folded. (b) and (c) are atomic resolution images of the bottom layer (b) and the top layer (c) of the same ribbon in (a). The hexagons help to visualize the lattice orientations, and thus to identify the chiralities of the ribbons with regard to the folding line. The bottom layer has a chirality of (5,2), and the bottom layer has a chirality of (3,1), with regard to the folding line near the bottom of the image (c) (marked as a dotted line).

does not come from the ribbons or from the few layer graphene, but rather from the SiO_2 substrate, as we explained in section 7.3. These ribbons have widths ranging from 20 nm to about 100 nm, and have lengths up to several microns. By taking smaller area scans on the ribbon surfaces, we find that most of the ribbons have one side of the edge folded and the other side open. The open edge usually shows a sharp contrast in the STM image, while the folded edge can be blurred, likely due to the curved folding structure. Figures 7.7c and 7.7d are two typical ribbon images exhibiting such a folded and open edge structures. The edge folding can be furthered verified by taking a line scan across the ribbon width. The height profile shows a one-layer thickness on one edge, and about a two-layer thickness on the other edge, as indicated in Figures 7.7e and 7.7f.

Atomic resolution images in Figs. 7.8(b) and (c) can be obtained on these graphene nanoribbons using STM. These results confirm that the rough morphology in large area scans (Fig. 7.8(a)) comes from the SiO_2 substrate, rather than from surface contaminations or corrugations on the ribbon itself.

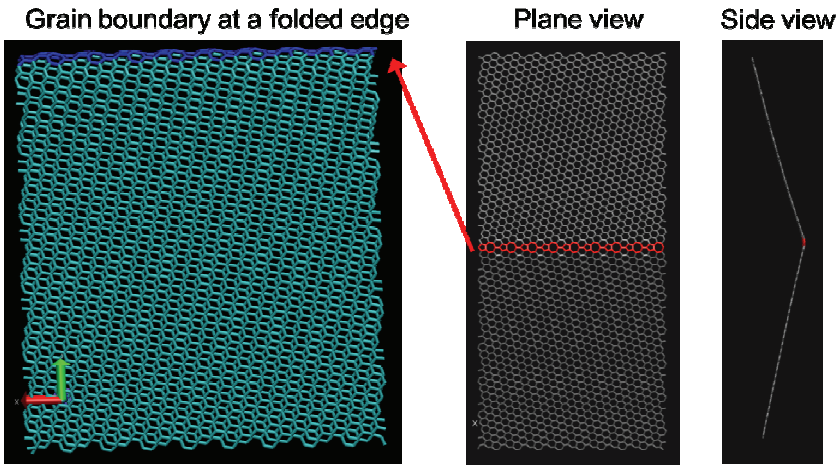

Figure 7.9 A theoretical model of a grain boundary consisting of 5-7 defects located at a folded graphene nanoribbon edge.

These CVD grown graphene nanoribbons indeed have an ultra clean surface even after the wet transfer process, and have a highly crystalline structure, comparable to that in HOPG derived graphene samples. For a folded graphene nanoribbon (Figure 7.8a), by comparing the hexagonal orientations with regard to the folding line, we can determine the chiralities of both the bottom layer and the top layer of the nanoribbon. The chirality for the bottom layer of the nanoribbon in Figure 7.8a is found to be (5,2), and the top layer to be (3,1).

For an unfolded perfect graphene nanoribbon with no defects, the folding line draws a chiral angle which determines the chirality of the edges on both sides of the folding line. So if we know the chirality for the bottom layer of the nanoribbon relative to the folding line, the chirality for the top layer is also determined. For example, a (5,2) bottom layer will form a (5,2) top layer ribbon. However, in our image, the top layer is measured to be (3,1) instead of (5,2). In order to understand this discrepancy, a theoretical model is drawn for a folded ribbon with (5,2) and (3,1) chiralities for the bottom and the top layers respectively (see Figure 7.9). It is shown that a grain boundary consisting of 5-7 defects may exist at the fold, which results in a discrepancy in the chiralities between the top and bottom layer edges. More interestingly, the side view of the stabilized graphene with a grain boundary in the middle shows that it forms an angle at the grain boundary, which we think may assist the ribbon folding we observed in STM images. It is also noteworthy that the difference in the chiral

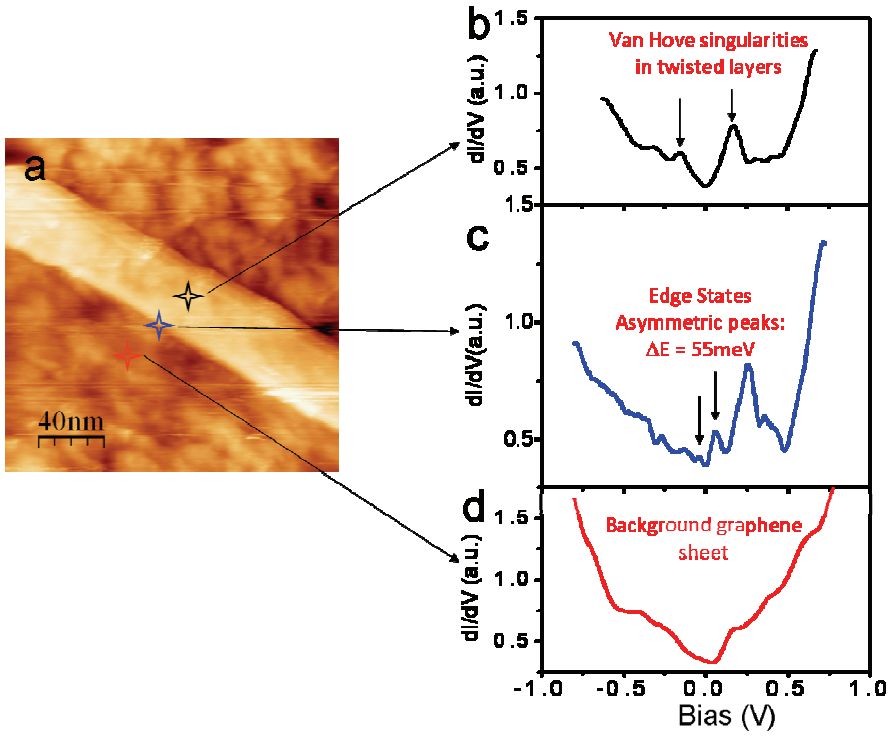

Figure 7.10 STS measurement of a graphene nanoribbon on few layer graphene. (a) is an STM image of a graphene nanoribbon on few layer graphene. (b-d) are STS differential conductance measurements (dI/dV) in the middle region of the ribbon (b), at the ribbon edge (c), and at the background graphene sheet (d).

angles between (3,1) and (5,2) chiral angles is very small. So besides the possibility of a grain boundary existing at the fold, other factors such as sudden surface corrugation near the fold may also result in the measured discrepancy of the chiralities.

7.5 Edge states in GNR

We also conducted STS measurements of a graphene nanoribbon at a low temperature of about 25 K. Figure 7.10 shows the spectra obtained in the middle of the ribbon, at the ribbon edge and at the background few layer graphene. The interior region of the ribbon surface shows two prominent peaks in the spectrum on opposite sides of the Dirac point, which we attribute to the Van Hove singularities in twisted graphene layers (see section 7.3). The energy separation between this two peaks is measured to be 400 meV, which corresponds to a twist

angle of 3.5^0 between the adjacent layers (the graphene nanoribbon and the background layer in this case). The spectrum at the ribbon edge shows two asymmetric peaks with an energy separation of about 55 meV. These peaks are probably due to the edge states in the graphene nanoribbon. A very similar result of the edge states with theoretical calculations is reported recently in carbon nanotube unzipped graphene nanoribbons [112]. Comparing with the calculations done by Tao et al. [112], our edges are likely also magnetic and have an intrinsic local magnetic field. We have also obtained a series of spectra at different locations along the ribbon width direction, and found that the intensity of the two peaks (edge states) decreases as we move away from the edge. This also provides evidence that the two peaks are indeed due to edge states.

7.6 Summary

In this chapter we have studied the morphologic and electronic properties in few layer graphene and graphene nanoribbons using STM and STS.

These unique materials grown by atmosphere pressure CVD have a very clean surface and highly crystalline structures, comparable to the HOPG derived samples, making them well-suited for the STM/STS study.

The electronic properties of few layer graphene can be tuned by an interlayer twist and by intra-layer strains. The twist between adjacent graphene layers gives rise to Van Hove singularities in the electron density of states. And the strains in the layers shift the Dirac point of the graphene.

We have also investigated the graphene nanoribbons structures and their electronic properties. STM provides us with a sensitive tool for studying the edge folding in graphene nanoribbons. And atomic resolution images of a folded graphene ribbon indicate that a grain boundary may exist at the folding line. Finally, edge states have been measured in our graphene nanoribbons with clean surfaces and relatively smooth edges. A direct correlation between the edge geometry and the electronic measurement at the edge is still lacking, and

theoretical calculations are needed to understand the magnetic and electronic properties of different chiral edges in graphene nanoribbons.

Chapter 8

In-situ TEM study of bismuth nanowires and nanoparticles

8.1 Background

The anisotropic electronic structure of Bi provides some directions along the constant energy surfaces for the three electron pockets at the L point of the Brillouin zone which have very low effective mass components giving rise to high mobility carriers. At the same time, the constant energy surfaces of bismuth have other directions with heavy masses giving rise to a high density of states. For both of these reasons, very good thermoelectric properties should be obtained for carrier transport along the low mass direction. However, as the size of a Bi nanowire or a Bi nanoparticle become smaller, the lowest quantized level in the conduction band moves up in energy and the highest quantized level in the valence band moves down, so that eventually these levels cross and a semimetal to semiconductor transition occurs. This transition occurs for larger diameter nanostructures as the temperature is decreased or as Sb is added in the structure (up to about 10%). In the semiconducting state, transport by electrons and not by holes can be achieved by n-type doping, thereby allowing us to capture the benefits of the anisotropic constant energy surfaces of the L point carriers in Bi. The heavy atomic mass of Bi also results in a low thermal conductivity which is also desirable for good thermoelectric performance.

Studies at the single nanowire and single particle level are necessary to probe the anisotropic aspects of these anisotropic constant energy surfaces. Experiments inside a transmission electron microscope allow us to produce clean Bi nanostructures free of oxides, and to study both their structural and electronic properties at the same time. This is highly advantageous for studying the

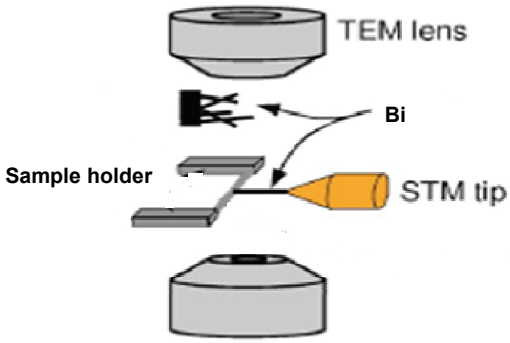

Figure 8.1 Schematic diagram of the in-situ TEM-STM system used to make simultaneous electrical and structural measurements [113].

semimetal-semiconductor transition and how this transition could enhance the thermoelectric properties of this materials system.

Electrical transport measurements of individual nanowires and nanoparticles have always been challenging, especially for very fine Bi nanostructures (diameters < 100nm) due to both their tendency of bismuth to oxidize easily and to their poor mechanical properties [114]. Here we present a direct approach to make single nanowire or nanoparticle measurements within an in-situ TEM-STM system (see Chapter 4, section 4.1.1.). As shown in Figure 8.1, the suspended nanowires or nanoparticles on the sample holder (which also serve as one electrode) can be approached and contacted by the STM probe. The movement of the STM tip is controlled by piezoelectric materials, and the STM tip can be observed under the TEM. With this setup, we are able to make electrical measurements on nanostructures with different sizes and morphologies, while imaging the nanostructures simultaneously.

8.2 Experiment

In this section, the Bi materials growth, *in-situ* TEM measurements on Bi nanowires and Bi nanoparticles will be presented. The structural behavior is monitored simultaneously as we change the applied voltage.

8.2.1 Materials preparation

One-dimensional Bi nanowires are usually prepared using rigid inorganic or polymer templates. Here we prepared Bi nanowires and nanoparticles by a polyol process, which provides good shape control of the synthesized nanostructures. Nanowires with an average width of ~60nm and nanocubes with an average edge length of 60-80nm were synthesized by this basic process [115]. Bi nanoparticles with an edge length as small as 3.8nm can also be grown within the HRTEM chamber as described below.

8.2.2 Bi nanowires

As stated above, the two biggest challenges for Bi nanowire measurements are removing the thick oxide layer surrounding the nanowire without destroying the Bi core, and making good low contact resistance electrical contacts between the nanowire and the electrode. Within the TEM high vacuum chamber, we successfully removed the oxide shell surrounding the Bi nanowire by applying an electrical bias. Successive steps in the reaction process are shown in Figure 8.2 and Figure 8.3. Before applying a bias, a 19.6 nm wide, 50 nm long Bi nanowire inside a 7.2nm oxide layer is placed in contact with a gold STM probe and the other electrode, respectively. The measured lattice spacing and selected area diffraction pattern indicate the crystalline structure of the Bi core region to be along a <012> direction. After applying a ~3V bias for Joule heating for ~3min duration, the oxide shell disappears gradually, while the Bi core starts to expand. No crystalline structure of the nanowire was observed during this process. Shortly after this transformation starts, the shell layer surrounding the entire wire disappears, and the measured current under constant applied bias is increased, indicating the disappearance of oxide layer. Upon fast quenching to room temperature (achieved by cutting off the bias current), a single crystalline Bi structure along the <012> direction was observed for the nanowire (see Figure 8.3). The bias voltage should be controlled carefully, because once the reaction finishes, the current remains high, and the entire Bi nanowire could melt.

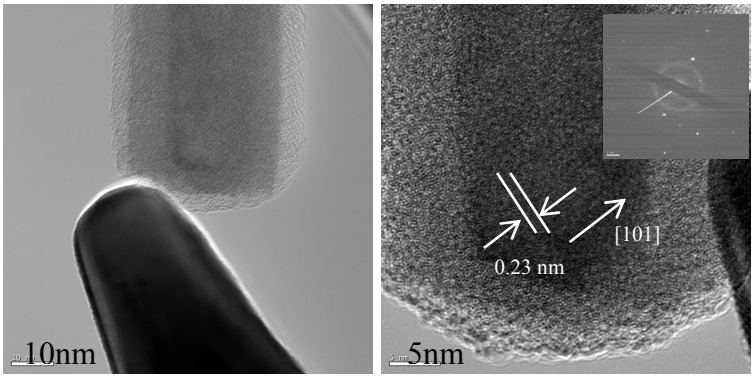

Figure 8.2 TEM images of Bi nanowires before Joule heating annealing: The Bi nanowire (surrounded by the Bi oxide shell) in contact with the gold electrode shown at low resolution (left) and higher resolution (right). Inset is a selected area diffraction pattern of the Bi core.

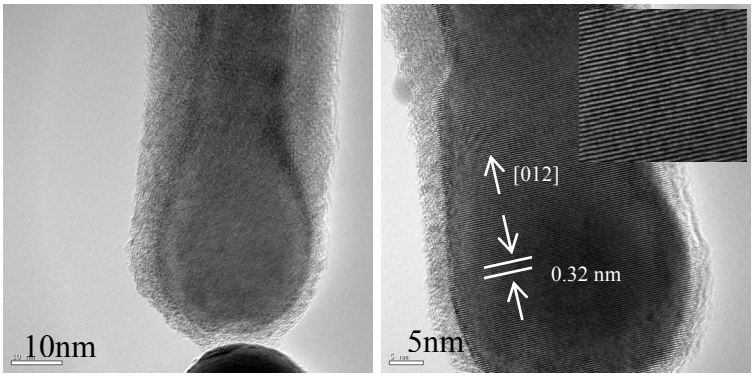

Figure 8.3 TEM images of Bi nanowires after Joule heating annealing: The Bi oxide shell disappears, and finally the nanowire becomes an almost pure crystalline Bi structure oriented along a <012> direction (right).

8.2.3 Bi nanoparticles

Bi nanoparticles are also a good candidate for studying quantum size effects, because they provide more quantum confined structures, and because a wide distribution of particle sizes and some choices in crystalline orientations can be readily achieved. However, conventionally grown Bi nanoparticles are always embedded in a surfactant solution, in order to prevent aggregation and oxidation. Thus Bi quantum dot electrical measurements become very challenging, and no electrical measurements for individual Bi quantum dots have so far been reported to our knowledge.

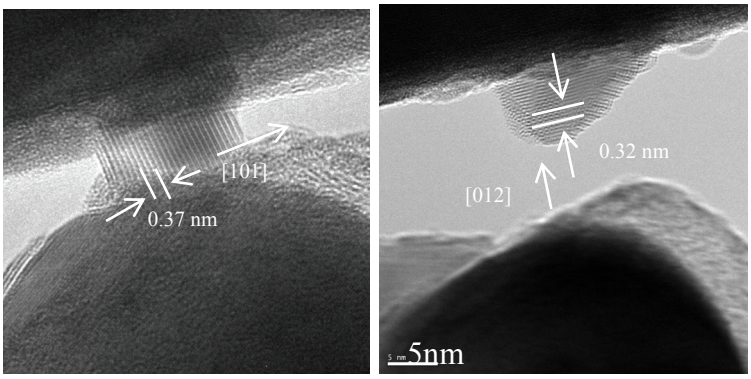

Figure 8.4 A 10nm×3.8nm Bi nanoparticle oriented along the <101> direction (left) and a 10nm×8nm Bi nanoparticle oriented along the <012> direction (right) were grown from bulk Bi upon applying a bias voltage between the STM tip and the big Bi particle.

With our setup, we were able, starting from big Bi particles, to grow clean Bi nanoparticles, with different sizes and crystalline orientations, by applying a dc bias using the setup shown in Figure 4. As we increase the bias voltage, the current density at the tip/Bi contact is increased. Then, by slowly moving the STM tip away from the big particle of Bi, a clean Bi nanoparticle is formed (Figure 8.4), with the nanoparticle in good contact with both the STM tip and the Bi big particle. Figure 8.4 shows a 10 nm by 3.8 nm Bi nanoparticle along the <101> direction (left) and a 10 nm by 8 nm Bi nanoparticle along the <012> direction (right) grown within the TEM chamber in another experiment done in the same set-up.

8.2.4 Electrical characterizations

Figure 8.5 shows the measured I-V curve for a 20.4 nm (wide) by 7.7 nm (long) nanoparticle between two electrodes. From the data in Figure 5, a conductance of 7.8×10^{-5} S is obtained which correspond to a conductivity of 2×10^{3} S/m if we assume that the particle has a circular cross section. For all the nanoparticles measured, the conductivities range from 2×10^{3} to 8×10^{3} S/m, which is about two orders of magnitude lower than that of the bulk Bi conductivity of ~ 8×10^{5} S/m.

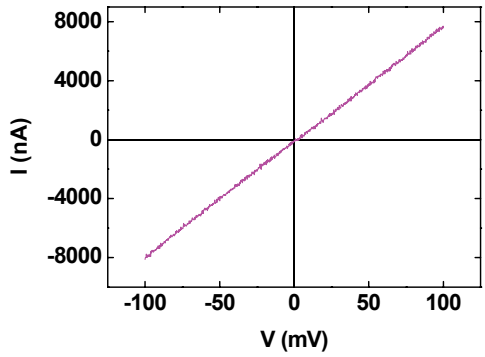

Figure 8.5 Measured I-V characteristics for a 20.4 nm (long) by 7.7 nm (wide) Bi nanoparticle.

The drop in conductivity in nano Bi may be due to a reduced carrier concentration arising from quantum confinement effects.

8.3 Discussion

Thermodynamics for Bi oxide reduction

Figure 8.2 and Figure 8.3 show that when a current is passed through the bismuth nanowire, a phase transition occurs whereby the oxide layer surrounding the Bi core is changed into Bi following Eq.1. The reaction takes place first close to the connection between the wire and tip of the STM. This is to be expected since the contact resistance between the tip and the wire will give rise to a local increase of temperature that will eventually favor the following reaction:

$$Bi_2O_{3(s/l)} \rightleftarrows \frac{3}{2}O_{2(g)} + 2Bi_{(l)} \quad (8.1)$$

in which, *s*, *l* and *g* denote solid, liquid and gas phases. As seen in Figure 8.3, the Bi nanowire initially melts when the temperature reaches 545K. Even if Bi_2O_3 is stable with liquid Bi and oxygen under normal conditions, a temperature increase because of the current and the reduced oxygen pressure in the vacuum chamber of the TEM will eventually favor the decomposition of the oxide. Omitting energy barrier considerations, the reaction to the right of Equation (8.1) will be spontaneous when the Gibbs free energy for Bi_2O_3 formation (ΔG) becomes positive. Following [116], the free energy of formation of Bi_2O_3 is:

$$\Delta G^o(kJ/mol) = -583.4 + 0.2938T(572K \le T \le 988K)$$

$$\Delta G^o(kJ/mol) = -543.8 + 0.2538T(988K \le T \le 1098K). \qquad (8.2)$$

Because of the reduced oxygen pressure in the vacuum chamber of the TEM, a pressure term correction must be added to the free energy, and the free energy of formation then becomes [117]

$$\Delta G = \Delta G^o - RT \ln\left(\frac{P_{O_2}^{3/2} a_{Bi}^2}{a_{Bi_2O_3}}\right) \qquad (8.3)$$

where R is the ideal gas constant, T is the temperature, P_{O_2} is approximated as the pressure in the TEM chamber and the a_i*'s* are defined as the activity coefficients of the Bi and of the Bi_2O_3. We take these a_i values be unity under the assumption that they are a perfect liquid and a perfect solid [118]. Figure 6 shows the result of these calculations and they demonstrate that for temperatures above 1003K, we should expect a decomposition of the Bi_2O_3 external layer into Bi.

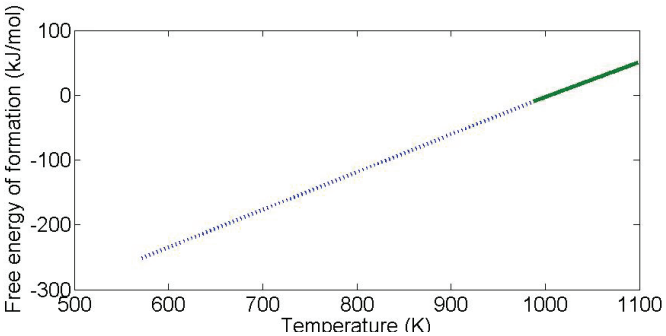

Figure 8.6 Free energy of formation of Bi_2O_3. The free energy of formation of Bi_2O_3 as a function of temperature under an oxygen pressure of 10^{-5}Pa. At ~1003K, when the free energy of formation becomes positive, it means that the decomposition of Bi_2O_3 will be thermodynamically favored and spontaneous, once the energy barriers are removed.

It also becomes evident that the high temperature needed to convert the oxide layer will be more than sufficient to locally melt the Bi core. This melting weakens the nanowire and explains why failure to remove the voltage bias from

the sample after the complete Bi_2O_3 to Bi transition has occurred could lead to a decomposition of the wire itself.

Bi nanoparticle in-situ growth

As we know, Bi is a very low melting point material with a bulk melting point of 271^0C, and the electro-migration of Bi could happen at a current density as low as 300A/cm^2. As we increase the applied bias, the temperature at the electrical contact increases dramatically as the current increases sharply, due to the Joule heating caused by the contact resistance. Thus the Bi atoms become mobile. Meanwhile, the current density reaches a high value of 2.5×10^6A/cm^2 so that the electro-migration of Bi becomes very strong near the electrical contact. For this reason the nanoparticle growth can be attributed to the electro-migration of Bi under high current density.

By controlling the current density and the speed of the STM tip movement, Bi nanoparticles with different sizes and orientations are grown. This gives us the feasibility of growing clean Bi nanoparticles with a wide size distribution, and studying their electrical properties at the single nanoparticle level, while measuring the structure of the same nanoparticle in the TEM.

8.4 Summary

We have here demonstrated a direct approach to reduce the oxide layer surrounding Bi nanowires by high temperature annealing using Joule heating of the nanowire in a TEM-STM system. This non-destructive method is good for measuring very fine Bi nanowires, and may also be applied to single nanowire measurements on a variety of materials in other high vacuum systems. We also demonstrate for the first time TEM in-situ growth of Bi nanoparticles by Joule heating and electro-migration. The clean various-sized particles are ideal for the study of quantum size effects in bismuth. Our first electrical measurements showed that the electrical conductivity of Bi nanoparticles is two orders of magnitude lower than that of bulk Bi, likely due to quantum size effects that

decrease the carrier concentration. Further experiments are needed for investigating the size and crystalline orientation dependences of the electrical conductivity of bismuth nanoparticles. This work forms a baseline for future thermoelectric measurements on Bi nanostructures.

Chapter 9

Conclusions and future work

In conclusion, I have used TEM, *in-situ* TEM, and STM to study carbon nanomaterials (such as graphene, graphitic nanoribbons and graphene nanoribbons) and thermoelectric nanomaterials (Bi nanowires and nanoparticles), with a special focus on the *in-situ* TEM technique. Carbon nanomaterials and thermoelectric nanomaterials provide us with many opportunities in the electronic device applications and renewable energy applications, and they both have unique physical and electronic properties that are interesting for fundamental scientific study. The *in-situ* TEM technique enables simultaneous structural and electrical measurements, and bridges the gap between the direct observation of the structures and the measurement of the properties in the nanoscale materials.

The chemical vapor deposition method for synthesizing graphene and BN thin films is a rapidly growing field in recent years. In this work, TEM and advanced TEM analysis tools have been used to study the crystallinity, the layer uniformity, thickness, and elemental distribution of CVD grown graphene and BN films, and the characterization results may also assist our understanding of the materials growth mechanism.

One of the biggest challenges so far for graphene electronic device applications is opening a well-defined bandgap. Graphene nanoribbons with a narrow width and atomically smooth edges can open a sizable bandgap, but smooth edges are very hard to produce. In this work, a novel method is developed for modifying the rough edges in graphitic nanoribbons to produce atomically smooth edges, using an *in-situ* Joule heating method. The edges thus produced show either zigzag or armchair configurations with very few other configurations. The interlayer stacking between adjacent graphene layers also transforms from AA stacking towards AB stacking during Joule heating, since

AA stacking is not a most stable ground state configuration. The edge modification is mainly attributed to the high temperature evaporation and current-induced local heating at edge hetero-junctions.

Folded edges are commonly found in graphene and graphene nanoribbons after high temperature annealing. And these edges have quite different properties and potential applications from open edges. Folded edge formation by both furnace heating and Joule heating has been investigated in this thesis. Theoretical study of the open and folded edge formation shows that electron beam irradiation may play a critical role in forming an open edge during the Joule heating process.

Pt nanoparticles are useful nanomaterials for catalytic applications, and they are adopted in this work for local temperature measurements during the *in-situ* Joule heating process. To my best knowledge, the direct observation of Pt nanoparticle melting, sintering and evaporation is reported for the first time. The melting, sintering and evaporation are induced by *in-situ* Joule heating rather than by electron beam irradiation. The competition between these processes makes the melting temperature of nanoparticles not trivial to obtain, and these processes are strongly affected by the particle concentration, particle size, temperature, etc.

After comprehensive TEM and *in-situ* TEM studies of carbon nanostructures, complementary STM and STS techniques are utilized to study the morphologic and electronic properties in graphene and graphene nanoribbons. Interlayer twist and in-plane strains are measured in CVD grown few layer graphene, which both modify the electronic properties in few layer graphene. CVD grown graphene nanoribbons with a high quality, comparable to HOPG derived samples, are synthesized, and edge folding, atomic arrangement, and edge states are probed using STM and STS techniques.

This *in-situ* TEM technique can also be applied in studying thermoelectric nanomaterials such as Bi nanowires and nanoparticles. Bi nanowires tend to form a thick oxide shell under atmosphere conditions, and this oxide shell is detrimental for electrical measurements. The oxide shell is found to be readily

removed by *in-situ* Joule heating, resulting in single crystalline Bi nanowires free of oxide shells. Moreover, bismuth nanoparticles with a few nanometers sizes can be drawn from bulk Bi by local heating. Electrical measurements show a reduced conductance for smaller size nanoparticles.

For future work, there are still many open questions and directions to be explored.

First of all, achieving single crystalline uniform graphene and few layer BN films by CVD is still awaits further work, and advanced characterization techniques combined with the materials synthesis will facilitate progress. Direct growth of graphene nanoribbons using CVD is promising for high quality and large scale materials production; however, the growth mechanism is still to be understood.

Secondly, the Joule heating method for producing atomically smooth edges in graphene nanoribbons has been demonstrated in a multilayered graphitic ribbon inside a TEM. For industrial applications, this method has to be adopted to a monolayer or few-layer graphene nanoribbon edge, and applied outside the TEM in a vacuum chamber. There are challenges associated with implementing this type of edge passivation, and for developing thermally insulating substrate (so that heat is not dissipated by the substrate), etc. By making such smooth ribbon edges outside the TEM, it will also be possible to measure various properties of the edges using other techniques such as Raman spectroscopy or to functionalize the edges.

Thirdly, the structure – property relationships in thermoelectric nano-composites can also be investigated using *in-situ* TEM measurements. Thermoelectric nanocomposite materials exhibit a superior performance over their bulk counterparts, and are promising for renewable energy applications. There are still many structural challenges for further enhancing the device performance, for example, how to prevent grain growth in the nanostructured material, and how to engineer the interfaces so that the figure of merit can be further increased.

Bibliography

1. Hicks, L.D. & Dresselhaus, M.S. Thermoelectric Figure of Merit of a One-Dimensional Conductor. *Physical Review B* **47**, 16631-16634 (1993).

2. Hicks, L.D. & Dresselhaus, M.S. Effect of Quantum-Well Structures on the Thermoelectric Figure of Merit. *Physical Review B* **47**, 12727-12731 (1993).

3. DiSalvo, F.J. Thermoelectric cooling and power generation. *Science* **285**, 703-706 (1999).

4. Zhang, Y.B., Tan, Y.W., Stormer, H.L. & Kim, P. Experimental observation of the quantum Hall effect and Berry's phase in graphene. *Nature* **438**, 201-204 (2005).

5. Venkatasubramanian, R., Siivola, E., Colpitts, T. & O'Quinn, B. Thin-film thermoelectric devices with high room-temperature figures of merit. *Nature* **413**, 597-602 (2001).

6. Novoselov, K.S., Geim, A.K., Morozov, S.V., Jiang, D., Zhang, Y., Dubonos, S.V., Grigorieva, I.V. & Firsov, A.A. Electric field effect in atomically thin carbon films. *Science* **306**, 666-669 (2004).

7. Novoselov, K.S., Geim, A.K., Morozov, S.V., Jiang, D., Katsnelson, M.I., Grigorieva, I.V., Dubonos, S.V. & Firsov, A.A. Two-dimensional gas of massless Dirac fermions in graphene. *Nature* **438**, 197-200 (2005).

8. Majumdar, A. Thermoelectricity in semiconductor nanostructures. *Science* **303**, 777-778 (2004).

9. Harman, T.C., Taylor, P.J., Walsh, M.P. & LaForge, B.E. Quantum dot superlattice thermoelectric materials and devices. *Science* **297**, 2229-2232 (2002).

10. Geim, A.K. & Novoselov, K.S. The rise of graphene. *Nature Materials* **6**, 183-191 (2007).

11. de Heer, W.A., Poncharal, P., Berger, C., Gezo, J., Song, Z.M., Bettini, J. & Ugarte, D. Liquid carbon, carbon-glass beads, and the crystallization of carbon nanotubes. *Science* **307**, 907-910 (2005).

12. Chen, Z.H., Lin, Y.M., Rooks, M.J. & Avouris, P. Graphene nano-ribbon electronics. *Physica E-Low-Dimensional Systems & Nanostructures* **40**, 228-232 (2007).

13. Boehm, H.P., Clauss, A., Fischer, G. & Hofmann, U. Surface Properties of Extremely Thin Graphite Lamellae. *Proceedings of the Fifth Conference on Carbon by Pergamon Press* (1962).

14. Novoselov, K.S., Geim, A.K., Morozov, S.V., Jiang, D., Zhang, Y., Dubonos, S.V., Grigorieva, I.V. & Firsov, A.A. Electric field effect in atomically thin carbon films. *Science* **306**, 666-669 (2004).

15. Novoselov, K.S., Jiang, Z., Zhang, Y., Morozov, S.V., Stormer, H.L., Zeitler, U., Maan, J.C., Boebinger, G.S., Kim, P. & Geim, A.K. Room-temperature quantum hall effect in graphene. *Science* **315**, 1379-1379 (2007).

16. Lee, C., Wei, X.D., Kysar, J.W. & Hone, J. Measurement of the elastic properties and intrinsic strength of monolayer graphene. *Science* **321**, 385-388 (2008).

17. Naumis, G.G., Terrones, M., Terrones, H. & Gaggero-Sager, L.M. Design of graphene electronic devices using nanoribbons of different widths. *Applied Physics Letters* **95**(2009).

18. Son, Y.W., Cohen, M.L. & Louie, S.G. Half-metallic graphene nanoribbons. *Nature* **444**, 347-349 (2006).

19. Han, M.Y., Ozyilmaz, B., Zhang, Y.B. & Kim, P. Energy band-gap engineering of graphene nanoribbons. *Physical Review Letters* **98**, 4 (2007).

20. Schwierz, F. Graphene transistors. *Nature Nanotechnology* **5**, 487-496 (2010).

21. Jia, X.T., Hofmann, M., Meunier, V., Sumpter, B.G., Campos-Delgado, J., Romo-Herrera, J.M., Son, H.B., Hsieh, Y.P., Reina, A., Kong, J., Terrones, M. & Dresselhaus, M.S. Controlled Formation of Sharp Zigzag and Armchair Edges in Graphitic Nanoribbons. *Science* **323**, 1701-1705 (2009).

22. Koskinen, P., Malola, S. & Hakkinen, H. Self-Passivating Edge Reconstructions of Graphene. *Physical Review Letters* **101**, 115502 (2008).

23. Kobayashi, Y., Fukui, K., Enoki, T., Kusakabe, K. & Kaburagi, Y. *Physical Review B* **71**, 193406 (2005).

24. Fukunaga, T., Itoh, K., Orimo, S., Aoki, M. & Fujii, H. *Journal of Alloys Compound* **327**, 224 (2001).

25. Terrones, M. Sharpening the Chemical Scissors to Unzip Carbon Nanotubes: Crystalline Graphene Nanoribbons. *ACS Nano* **4**, 1775-1781 (2010).

26. Kosynkin, D.V., Higginbotham, A.L., Sinitskii, A., Lomeda, J.R., Dimiev, A., Price, B.K. & Tour, J.M. Longitudinal unzipping of carbon nanotubes to form graphene nanoribbons. *Nature* **458**, 872-U5 (2009).

27. Li, X.L., Wang, X.R., Zhang, L., Lee, S.W. & Dai, H.J. Chemically derived, ultrasmooth graphene nanoribbon semiconductors. *Science* **319**, 1229-1232 (2008).

28. Campos-Delgado, J., Romo-Herrera, J.M., Jia, X.T., Cullen, D.A., Muramatsu, H., Kim, Y.A., Hayashi, T., Ren, Z.F., Smith, D.J., Okuno, Y., Ohba, T., Kanoh, H., Kaneko, K., Endo, M., Terrones, H., Dresselhaus, M.S. & Terrones, M. Bulk production of a new form of sp(2) carbon: Crystalline graphene nanoribbons. *Nano Letters* **8**, 2773-2778 (2008).

29. Murayama, H. & Maeda, T. A NOVEL FORM OF FILAMENTOUS GRAPHITE. *Nature* **345**, 791-793 (1990).

30. Mahanandia, P., Nanda, K.K., Prasad, V. & Subramanyam, S.V. Synthesis and characterization of carbon nanoribbons and single crystal iron filled carbon nanotubes. *Materials Research Bulletin* **43**, 3252-3262 (2008).

31. Higginbotham, A.L., Kosynkin, D.V., Sinitskii, A., Sun, Z.Z. & Tour, J.M. Lower-Defect Graphene Oxide Nanoribbons from Multiwalled Carbon Nanotubes. *ACS Nano* **4**, 2059-2069 (2010).

32. Jiao, L.Y., Zhang, L., Wang, X.R., Diankov, G. & Dai, H.J. Narrow graphene nanoribbons from carbon nanotubes. *Nature* **458**, 877-880 (2009).

33. Terrones, M. MATERIALS SCIENCE Nanotubes unzipped. *Nature* **458**, 845-846 (2009).

34. Cano-Marquez, A.G., Rodriguez-Macias, F.J., Campos-Delgado, J., Espinosa-Gonzalez, C.G., Tristan-Lopez, F., Ramirez-Gonzalez, D., Cullen, D.A., Smith, D.J., Terrones, M. & Vega-Cantu, Y.I. Ex-MWNTs: Graphene Sheets and Ribbons Produced by Lithium Intercalation and Exfoliation of Carbon Nanotubes. *Nano Letters* **9**, 1527-1533 (2009).

35. Ci, L., Xu, Z.P., Wang, L.L., Gao, W., Ding, F., Kelly, K.F., Yakobson, B.I. & Ajayan, P.M. Controlled Nanocutting of Graphene. *Nano Research* **1**, 116-122 (2008).

36. Campos, L.C., Manfrinato, V.R., Sanchez-Yamagishi, J.D., Kong, J. & Jarillo-Herrero, P. Anisotropic Etching and Nanoribbon Formation in Single-Layer Graphene. *Nano Letters* **9**, 2600-2604 (2009).

37. Jiao, L.Y., Wang, X.R., Diankov, G., Wang, H.L. & Dai, H.J. Facile synthesis of high-quality graphene nanoribbons. *Nature Nanotechnology* **5**, 321-325 (2010).

38. Kim, K., Sussman, A. & Zettl, A. Graphene Nanoribbons Obtained by Electrically Unwrapping Carbon Nanotubes. *ACS Nano* **4**, 1362-1366 (2010).

39. Tapaszto, L., Dobrik, G., Lambin, P. & Biro, L.P. Tailoring the atomic structure of graphene nanoribbons by scanning tunnelling microscope lithography. *Nature Nanotechnology* **3**, 397-401 (2008).

40. Cai, J.M., Ruffieux, P., Jaafar, R., Bieri, M., Braun, T., Blankenburg, S., Muoth, M., Seitsonen, A.P., Saleh, M., Feng, X.L., Mullen, K. & Fasel, R.

Atomically precise bottom-up fabrication of graphene nanoribbons. *Nature* **466**, 470-473 (2010).

41. Enoki, T., Kobayashi, Y. & Fukui, K.I. Electronic structures of graphene edges and nanographene. *International Reviews in Physical Chemistry* **26**, 609-645 (2007).

42. Meyer, J.C., Geim, A.K., Katsnelson, M.I., Novoselov, K.S., Booth, T.J. & Roth, S. The structure of suspended graphene sheets. *Nature* **446**, 60-63 (2007).

43. Novoselov, K.S., Jiang, D., Schedin, F., Booth, T.J., Khotkevich, V.V., Morozov, S.V. & Geim, A.K. Two-dimensional atomic crystals. *Proceedings of the National Academy of Sciences of the United States of America* **102**, 10451-10453 (2005).

44. Meyer, J.C., Girit, C.O., Crommie, M.F. & Zettl, A. Imaging and dynamics of light atoms and molecules on graphene. *Nature* **454**, 319-322 (2008).

45. Warner, J.H., Rummeli, M.H., Ge, L., Gemming, T., Montanari, B., Harrison, N.M., Buchner, B. & Briggs, G.A.D. Structural transformations in graphene studied with high spatial and temporal resolution. *Nature Nanotechnology* **4**, 500-504 (2009).

46. Warner, J.H., Rummeli, M.H., Gemming, T., Buchner, B. & Briggs, G.A.D. Direct Imaging of Rotational Stacking Faults in Few Layer Graphene. *Nano Letters* **9**, 102-106 (2009).

47. Warner, J.H., Schaffel, F., Rummeli, M.H. & Buchner, B. Examining the Edges of Multi-Layer Graphene Sheets. *Chemistry of Materials* **21**, 2418-2421 (2009).

48. Liu, Z., Suenaga, K., Harris, P.J.F. & Iijima, S. Open and Closed Edges of Graphene Layers. *Physical Review Letters* **102**(2009).

49. Huang, J.Y., Ding, F., Yakobson, B.I., Lu, P., Qi, L. & Li, J. In situ observation of graphene sublimation and multi-layer edge reconstructions. *Proceedings of the National Academy of Sciences of the United States of America* **106**, 10103-10108 (2009).

50. Girit, C.O., Meyer, J.C., Erni, R., Rossell, M.D., Kisielowski, C., Yang, L., Park, C.H., Crommie, M.F., Cohen, M.L., Louie, S.G. & Zettl, A. Graphene at the Edge: Stability and Dynamics. *Science* **323**, 1705-1708 (2009).

51. Warner, J.H., Rummeli, M.H., Bachmatiuk, A. & Buchner, B. Examining the stability of folded graphene edges against electron beam induced sputtering with atomic resolution. *Nanotechnology* **21**, 325702 (2010).

52. Stone, A.J. & Wales, D.J. THEORETICAL-STUDIES OF ICOSAHEDRAL C60 AND SOME RELATED SPECIES. *Chemical Physics Letters* **128**, 501-503 (1986).

53. Thrower, P.A. The Study of Defects in Graphite by Transmission Electron Microscopy. *Chemistry and Physics of Carbon* **5**, 261-262 (1969).

54. Cancado, L.G., Pimenta, M.A., Neves, B.R.A., Medeiros-Ribeiro, G., Enoki, T., Kobayashi, Y., Takai, K., Fukui, K., Dresselhaus, M.S., Saito, R. & Jorio, A. Anisotropy of the Raman spectra of nanographite ribbons. *Physical Review Letters* **93**(2004).

55. Cancado, L.G., Pimenta, M.A., Neves, B.R.A., Dantas, M.S.S. & Jorio, A. Influence of the atomic structure on the Raman spectra of graphite edges. *Physical Review Letters* **93**(2004).

56. Saito, R., Furukawa, M., Dresselhaus, G. & Dresselhaus, M.S. Raman spectra of graphene ribbons. *Journal of Physics: Condensed Matter* **22**, 334203 (2010).

57. Lahiri, J., Lin, Y., Bozkurt, P., Oleynik, II & Batzill, M. An extended defect in graphene as a metallic wire. *Nature Nanotechnology* **5**, 326-329 (2010).

58. Botello-Mendez, A.R., Cruz-Silva, E., Lopez-Urias, F., Sumpter, B.G., Meunier, V., Terrones, M. & Terrones, H. Spin Polarized Conductance in Hybrid Graphene Nanoribbons Using 5-7 Defects. *ACS Nano* **3**, 3606-3612 (2009).

59. Ci, L., Song, L., Jin, C.H., Jariwala, D., Wu, D.X., Li, Y.J., Srivastava, A., Wang, Z.F., Storr, K., Balicas, L., Liu, F. & Ajayan, P.M. Atomic layers of hybridized boron nitride and graphene domains. *Nature Materials* **9**, 430-435 (2010).

60. Tada, T. & Yoshizawa, K. Quantum transport effects in nanosized graphite sheets. II. Enhanced transport effects by heteroatoms. *Journal of Physical Chemistry B* **107**, 8789-8793 (2003).

61. Denis, P.A. Band gap opening of monolayer and bilayer graphene doped with aluminium, silicon, phosphorus, and sulfur. *Chemical Physics Letters* **492**, 251-257 (2010).

62. Radovic, L.R. & Bockrath, B. On the chemical nature of graphene edges: Origin of stability and potential for magnetism in carbon materials. *Journal of the American Chemical Society* **127**, 5917-5927 (2005).

63. Cervantes-Sodi, F., Csanyi, G., Piscanec, S. & Ferrari, A.C. Edge-functionalized and substitutionally doped graphene nanoribbons: Electronic and spin properties. *Physical Review B* **77**(2008).

64. Wang, X.R., Li, X.L., Zhang, L., Yoon, Y., Weber, P.K., Wang, H.L., Guo, J. & Dai, H.J. N-Doping of Graphene Through Electrothermal Reactions with Ammonia. *Science* **324**, 768-771 (2009).

65. Joly, V.L.J., Kiguchi, M., Hao, S.J., Takai, K., Enoki, T., Sumii, R., Amemiya, K., Muramatsu, H., Hayashi, T., Kim, Y.A., Endo, M., Campos-Delgado, J., Lopez-Urias, F., Botello-Mendez, A., Terrones, H.,

Terrones, M. & Dresselhaus, M.S. Observation of magnetic edge state in graphene nanoribbons. *Physical Review B* **81**, 245428 (2010).

66. Bai, J., Cheng, R., Xiu, F., Liao, L., Wang, M., Shailos, A., Wang, K.L., Huang, Y. & Duan, X. Very large magnetoresistance in graphene nanoribbons. *Nature Nanotechnology* (2010).

67. Reina, A., Jia, X.T., Ho, J., Nezich, D., Son, H.B., Bulovic, V., Dresselhaus, M.S. & Kong, J. Large Area, Few-Layer Graphene Films on Arbitrary Substrates by Chemical Vapor Deposition. *Nano Letters* **9**, 30-35 (2009).

68. Reina, A., Thiele, S., Jia, X.T., Bhaviripudi, S., Dresselhaus, M.S., Schaefer, J.A. & Kong, J. Growth of Large-Area Single- and Bi-Layer Graphene by Controlled Carbon Precipitation on Polycrystalline Ni Surfaces. *Nano Research* **2**, 509-516 (2009).

69. Dean, C.R., Young, A.F., Meric, I., Lee, C., Wang, L., Sorgenfrei, S., Watanabe, K., Taniguchi, T., Kim, P., Shepard, K.L. & Hone, J. Boron nitride substrates for high-quality graphene electronics. *Nature Nanotechnology* **5**, 722-726 (2010).

70. Shi, Y.M., Hamsen, C., Jia, X.T., Kim, K.K., Reina, A., Hofmann, M., Hsu, A.L., Zhang, K., Li, H.N., Juang, Z.Y., Dresselhaus, M.S., Li, L.J. & Kong, J. Synthesis of Few-Layer Hexagonal Boron Nitride Thin Film by Chemical Vapor Deposition. *Nano Letters* **10**, 4134-4139 (2010).

71. Nakada, K., Fujita, M., Dresselhaus, G. & Dresselhaus, M.S. Edge state in graphene ribbons: Nanometer size effect and edge shape dependence. *Physical Review B* **54**, 17954-17961 (1996).

72. Yang, L., Park, C.H., Son, Y.W., Cohen, M.L. & Louie, S.G. Quasiparticle energies and band gaps in graphene nanoribbons. *Physical Review Letters* **99**(2007).

73. Wang, X., Ischebeck, R., Muggli, P., Katsouleas, T., Joshi, C., Mori, W.B. & Hogan, M.J. Positron injection and acceleration on the wake driven by an electron beam in a foil-and-gas plasma. *Physical Review Letters* **101**, 124801 (2008).

74. Wakabayashi, K. Electronic transport properties of nanographite ribbon junctions. *Physical Review B* **6412** (2001).

75. Shemella, P., Zhang, Y., Mailman, M., Ajayan, P.M. & Nayak, S.K. Energy gaps in zero-dimensional graphene nanoribbons. *Applied Physics Letters* **91**, 042101 (2007).

76. Cervantes-Sodi, F., Csanyi, G., Piscanec, S. & Ferrari, A.C. Edge-functionalized and substitutionally doped graphene nanoribbons: Electronic and spin properties. *Physical Review B* **77**, 165427 (2008).

77. Li, T.C. & Lu, S.P. Quantum conductance of graphene nanoribbons with edge defects. *Physical Review B* **77**, 085408 (2008).

78. Huang, J.Y., Chen, S., Ren, Z.F., Chen, G. & Dresselhaus, M.S. Real-time observation of tubule formation from amorphous carbon nanowires under high-bias Joule heating. *Nano Letters* **6**, 1699-1705 (2006).

79. Banhart, F. Irradiation effects in carbon nanostructures. *Reports on Progress in Physics* **62**, 1181-1221 (1999).

80. Kelly, B.T. *Physics of Graphite*.(Applied Science Publishers, 1981)

81. Jin, C., Suenaga, K. & Lijima, S. Vacancy migrations in carbon nanotubes. *Nano Letters* **8**, 1127-1130 (2008).

82. Rouzaud, J.N., Oberlin, A. & Benybassez, C. Carbon-Films - Structure and Microtexture (Optical and Electron-Microscopy, Raman-Spectroscopy). *Thin Solid Films* **105**, 75-96 (1983).

83. Goma, J. & Oberlin, M. Graphitization of Thin Carbon-Films. *Thin Solid Films* **65**, 221-232 (1980).

84. Son, Y.W., Cohen, M.L. & Louie, S.G. Energy gaps in graphene nanoribbons. *Physical Review Letters* **97**, 216803 (2006).

85. Areshkin, D.A., Gunlycke, D. & White, C.T. Ballistic transport in graphene nanostrips in the presence of disorder: Importance of edge effects. *Nano Letters* **7**, 204-210 (2007).

86. Vandescuren, M., Hermet, P., Meunier, V., Henrard, L. & Lambin, P. Theoretical study of the vibrational edge modes in graphene nanoribbons. *Physical Review B* **78**, 195401 (2008).

87. Amara, H., Latil, S., Meunier, V., Lambin, P. & Charlier, J.C. Scanning tunneling microscopy fingerprints of point defects in graphene: A theoretical prediction. *Physical Review B* **76**, 115423 (2007).

88. Endo, M., Kim, Y.A., Hayashi, T., Fukai, Y., Oshida, K., Terrones, M., Yanagisawa, T., Higaki, S. & Dresselhaus, M.S. Structural characterization of cup-stacked-type nanofibers with an entirely hollow core. *Applied Physics Letters* **80**, 1267-1269 (2002).

89. Endo, M., Lee, B.J., Kim, Y.A., Kim, Y.J., Muramatsu, H., Yanagisawa, T., Hayashi, T., Terrones, M. & Dresselhaus, M.S. Transitional behaviour in the transformation from active end planes to stable loops caused by annealing. *New Journal of Physics* **5**, 66296-8 (2003).

90. Gogotsi, Y., Libera, J.A., Kalashnikov, N. & Yoshimura, M. Graphite polyhedral crystals. *Science* **290**, 317-320 (2000).

91. Joseyacaman, M., Terrones, H., Rendon, L. & Dominguez, J.M. Carbon Structures Grown from Decomposition of a Phenylacetylene and Thiophene Mixture on Ni Nanoparticles. *Carbon* **33**, 669-678 (1995).

92. Liu, Z., Suenaga, K., Harris, P.J.F. & Iijima, S. Open and Closed Edges of Graphene Layers. *Physical Review Letters* **102**, 015501 (2009).

93. Campos-Delgado, J., Kim, Y.A., Hayashi, T., Morelos-Gomez, A., Hofmann, M., Muramatsu, H., Endo, M., Terrones, H., Shull, R.D., Dresselhaus, M.S. & Terrones, M. Thermal stability studies of CVD-grown graphene nanoribbons: Defect annealing and loop formation. *Chemical Physics Letters* **469**, 177-182 (2009).

94. Huang, J.Y., Chen, S., Wang, Z.Q., Kempa, K., Wang, Y.M., Jo, S.H., Chen, G., Dresselhaus, M.S. & Ren, Z.F. Superplastic carbon nanotubes - Conditions have been discovered that allow extensive deformation of rigid single-walled nanotubes. *Nature* **439**, 281-281 (2006).

95. Huang, J.Y., Chen, S., Jo, S.H., Wang, Z., Han, D.X., Chen, G., Dresselhaus, M.S. & Ren, Z.F. Atomic-scale imaging of wall-by-wall breakdown and concurrent transport measurements in multiwall carbon nanotubes. *Physical Review Letters* **94**, 236802 (2005).

96. Jia, X.T., Campos-Delgado, J., Gracia-Espino, E.E., Hofmann, M., Muramatsu, H., Kim, Y.A., Hayashi, T., Endo, M., Kong, J., Terrones, M. & Dresselhaus, M.S. Loop formation in graphitic nanoribbon edges using furnace heating or Joule heating. *Journal of Vacuum Science & Technology B* **27**, 1996-2002 (2009).

97. Cruz-Silva, E., Botello-Mendez, A.R., Barnett, Z., Jia, X., Dresselhaus, M.S., Terrones, H., Terrones, M., Sumpter, B.G. & Meunier, V. Controlling Edge Morphology in Graphene Layers Using Electron Irradiation: From Sharp Atomic Edges to Coalesced Layers Forming Loops. *Physical Review Letters* **105**, 045501 (2010).

98. Krasheninnikov, A.V. & Banhart, F. Engineering of nanostructured carbon materials with electron or ion beams. *Nature Materials* **6**, 723-733 (2007).

99. Rodriguez-Manzo, J.A. & Banhart, F. Creation of Individual Vacancies in Carbon Nanotubes by Using an Electron Beam of 1 angstrom Diameter. *Nano Letters* **9**, 2285-2289 (2009).

100. Buffat, P.A. Lowering of Melting Temperature of Small Gold Crystals between 150a and 25a Diameter. *Thin Solid Films* **32**, 283-286 (1976).

101. Buffat, P.A. Electron diffraction and HRTEM studies of multiply-twinned structures and dynamical events in metal nanoparticles: facts and artefacts. *Materials Chemistry and Physics* **81**, 368-375 (2003).

102. Farrell, H.H. & Van Siclen, C.D. Binding energy, vapor pressure, and melting point of semiconductor nanoparticles. *Journal of Vacuum Science & Technology B* **25**, 1441-1447 (2007).

103. Unruh, K.M., Huber, T.E. & Huber, C.A. Melting and Freezing Behavior of Indium Metal in Porous Glasses. *Physical Review B* **48**, 9021-9027 (1993).

104. Zhang, Y.B., Brar, V.W., Wang, F., Girit, C., Yayon, Y., Panlasigui, M., Zettl, A. & Crommie, M.F. Giant phonon-induced conductance in

scanning tunnelling spectroscopy of gate-tunable graphene. *Nature Physics* **4**, 627-630 (2008).

105. Li, G.H., Luican, A., dos Santos, J., Neto, A.H.C., Reina, A., Kong, J. & Andrei, E.Y. Observation of Van Hove singularities in twisted graphene layers. *Nature Physics* **6**, 109-113 (2009).

106. Levy, N., Burke, S.A., Meaker, K.L., Panlasigui, M., Zettl, A., Guinea, F., Neto, A.H.C. & Crommie, M.F. Strain-Induced Pseudo-Magnetic Fields Greater Than 300 Tesla in Graphene Nanobubbles. *Science* **329**, 544-547 (2010).

107. Ritter, K.A. & Lyding, J.W. The influence of edge structure on the electronic properties of graphene quantum dots and nanoribbons. *Nature Materials* **8**, 235-242 (2009).

108. Bhaviripudi, S., Jia, X.T., Dresselhaus, M.S. & Kong, J. Role of Kinetic Factors in Chemical Vapor Deposition Synthesis of Uniform Large Area Graphene Using Copper Catalyst. *Nano Letters* **10**, 4128-4133 (2010).

109. Li, G.H., Luican, A., dos Santos, J.M.B.L., Neto, A.H.C., Reina, A., Kong, J. & Andrei, E.Y. Observation of Van Hove singularities in twisted graphene layers. *Nature Physics* **6**, 109-113 (2010).

110. dos Santos, J., Peres, N.M.R. & Castro, A.H. Graphene bilayer with a twist: Electronic structure. *Physical Review Letters* **99**(2007).

111. Castro Neto, A.H., Guinea, F., Peres, N.M.R., Novoselov, K.S. & Geim, A.K. The electronic properties of graphene. *Reviews of Modern Physics* **81**, 109-162 (2009).

112. Tao, C., Jiao, L.Y., Yazyev, O.V., Chen, Y.C., Feng, J., Zhang, X., Capaz, R.B., Tour, J.M., Zettl, A., Louie, S.G., Dai, H.J. & Crommie, M.F. Spatially resolving spin-split edge states of chiral graphene nanoribbons. *(Submitted to arXiv)* (2011).

113. Dames, C., Chen, S., Harris, C.T., Huang, J.Y., Ren, Z.F., Dresselhaus, M.S. & Chen, G. A hot-wire probe for thermal measurements of nanowires and nanotubes inside a transmission electron microscope. *Review of Scientific Instruments* **78**, 104903 (2007).

114. Cronin, S.B., Lin, Y.M., Rabin, O., Black, M.R., Ying, J.Y., Dresselhaus, M.S., Gai, P.L., Minet, J.P. & Issi, J.P. Making electrical contacts to nanowires with a thick oxide coating. *Nanotechnology* **13**, 653-658 (2002).

115. Wang, W.Z., Poudel, B., Ma, Y. & Ren, Z.F. Shape control of single crystalline bismuth nanostructures. *Journal of Physical Chemistry B* **110**, 25702-25706 (2006).

116. Ganesan, R., Gnanasekaran, T. & Srinivasa, R.S. Determination of standard molar Gibbs free energy of formation of Bi2O3 over a wide temperature range by EMF method. *Journal of Chemical Thermodynamics* **35**, 1703-1716 (2003).

117. Berube, V., Radtke, G., Dresselhaus, M. & Chen, G. Size effects on the hydrogen storage properties of nanostructured metal hydrides: A review. *International Journal of Energy Research* **31**, 637-663 (2007).

118. Glasstone, S. *Textbook of physical chemistry, Van Nostrand Co: New York* (1946).